BIOANALYTICAL APPROACHES TO CHEMICAL BIOLOGY

By

Stephen Reese Harry

Dissertation

Submitted to the Faculty of the

Graduate School of Vanderbilt University

in partial fulfillment of the requirements

for the degree of

DOCTOR OF PHILOSOPHY

in

Chemistry

August, 2010

Nashville, Tennessee

Approved:

Professor David W. Wright

Professor Brian O. Bachmann

Professor John A. McLean

Professor Eric P. Skaar

This dissertation is dedicated:

to my loving and constantly supportive parents, Mike and Violet, whose high expectations unlocked the door to limitless opportunities in life.

to my wife Brandi, whose relentless love, support and devotion has allowed me to follow my dreams.

ACKNOWLEDGEMENTS

On several occasions, I was approached by young potential graduate students that constantly ask the question, "what is the hardest part of graduate school?" The answer to this question evolves in several stages beginning with excitement of the new challenges that lay ahead. This excitement quickly morphs into a growing responsibility that is the heart of personal development. As this chapter of my life concludes, I have to say that persistence was the core component associated with my achievements. Persistence is not a quality that can be learned but one that must be acquired by practical means. For this, I am eternally grateful to my advisor David Wright for teaching me the merits and rewards of persistence.

To all my fellow labmates, it has been a pleasure. There are way too many to name. Specifically, I would like to recognize my friend Ryan Rutledge for introducing me to the wonderful world of fantasy sports....among other things. Next, my eternal friend Melissa Carter who travelled the untamed road of hemozoin with me and is a constant source of motivation. I cannot forget my friend, Jonas Perez, for constantly keeping me entertained by every means possible and to the chemistry department softball team for providing an outlet to relieve everyday stress.

Finally, to my beautiful wife Brandi. Even from the beginning, she was always supportive and managed to give me that kick in the rear that every person needs from time to time. I love you very much and am so excited about our future endeavors, wherever that may take us.

TABLE OF CONTENTS

Page

DEDICATION ii

ACKNOWLEDGEMENTS iii

LIST OF TABLES vi

LIST OF FIGURES vii

Chapter

I. THE OMICS ERA: A PARALLEL EVOLUTION OF SYSTEMS BIOLOGY WITH BIOANALYTICAL METHODOLOGY 1

References 8

II. IDENTIFICATION OF HYDROXYEICOSATETRAENOIC ACID COMPONENTS OF SCHISTOSOMAL HEMOZOIN 10

Introduction 10
Experimental 16
Results and Discussion 23
Conclusion 33
References 34

III. METABOLIC IMPACT OF 4-HYDROXYNONENAL ON MACROPHAGE FUNCTION AND ACTIVATION 37

Introduction 37
Experimental 42
Results and Discussion 48
Conclusion 66
References 68

IV. NOVEL HAIRPIN DNA-COATED GOLD NANOPARTICLES FOR THE DETECTION OF METASTATIC MELANOMA 70

Introduction 70
Experimental 74
Results and Discussion 82
Conclusion 100

Future Directions 102
References.....104

LIST OF TABLES

Table Page

1. HNE-induced metabolic rate changes in steady state macrophage metabolism....52

2. HNE effect on metabolic rate changes in PMA-induced oxidative burst.....58

3. Melanoma hAuNP oligonucleotide sequence information.....94

4. hAuNP expression values for multiple melanoma cell lines 97

5. RT-PCR relative transcription ratios for multiple melanoma cell lines 99

LIST OF FIGURES

Figure		Page
1.	Schematic of the fundamental principles of biological processes	2
2.	Worldwide distribution of schistosomiasis	10
3.	Chemical structure of hemozoin	12
4.	Phagocytic function in response to extracellular microbial challenge	13
5.	Schistosomal hemozoin and parasitic egg deposition in *S. mansoni*	14
6.	Hemozoin from *S. mansoni*	23
7.	IR and XRD of hemozoin from *S. mansoni*	24
8.	HETE-containing lipid coat of native hemozoin from *S. mansoni*	25
9.	Extracted ion profile of *Sm*Hz lipid coat	26
10.	Chiral RP-LC-MS/MS of *Sm*Hz lipid coat	28
11.	Hemozoin-mediated lipid peroxidation of arachidonic acid	29
12.	Extracted ion profile of HETEs from β-hematin-AA reaction	30
13.	Extracted ion profile of HETEs from SmHz-AA reaction	31
14.	Impact of native *Sm*Hz and components on iNOS activity	32
15.	Schematic of a Cytosensor microphysiometer	38
16.	Schematic of a fully assembled MMP sensor head	40
17.	Cellular energy metabolism	48
18.	Modified MMP sensor head	49
19.	Conversion of raw MMP measurements to metabolic rate values	51
20	3D composite of HNE-treated steady state macrophage metabolism	53

21. HNE effects on macrophage metabolism as a function of concentration 54

22. PMA-stimulated macrophage metabolic response.....56

23. 3D composite of HNE effects on macrophage oxidative burst metabolism 60

24. HNE effects on macrophage oxidative burst metabolism as a function of concentration 61

25. HNE inhibition of PMA-induced oxidative burst in RAW 264.7 cells 62

26. Western blot analysis of HNE-modified PKC from cell lysates.....64

27. Tyrosinase-mediated melanin synthesis 71

28. Schematic of hAuNP design 82

29. hAuNP mRNA detection scheme 83

30. TYR hAuNP target selectivity assay 85

31. DNase I susceptibility assay 86

32. hAuNP labeling of SK-MEL-28 melanoma cells 87

33. RT-PCR analysis of TYR expression in SK-MEL-28 and HEp2 cells 88

34. Coculture composite scanning confocal imaging of hAuNP 89

35. Z-stack confocal image of cocultured SK-MEL-28 and HEp2 cells 90

36. Coculture flow cytometric analysis of SK-MEL-28 and HEp2 cells 91

37. Confocal fluorescence imaging of primary melanoma cells.....92

38. hAuNP specificity of melanoma profile probes.....94

39. Confocal imaging of SK-MEL-28 cells with melanoma profile hAuNPs.....95

40. hAuNP expression values for multiple melanoma cell lines 97

41. RT-PCR relative transcription ratios for multiple melanoma cell lines 98

CHAPTER I

THE OMICS ERA: A PARALLEL EVOLUTION OF SYSTEMS BIOLOGY WITH BIOANALYTICAL METHODOLOGY

In literal meaning, systems biology is defined as the comprehensive, quantitative analysis of the manner in which all of the components of a biological system interact over time.[1] Systems biology is hypothesis-driven, global, quantitative, iterative, integrative and dynamic.[2] The systems approach begins with acquisition of large global sets of biological data from as much information and as many biological processes possible.[2] From a cell biology perspective, systems biology is a major contributor to the development and integration of traditional and emerging bioanalytical techniques for measuring small perturbations of the inner workings of a cell.

Cells are living systems full of various functional molecules which eventually determine the phenotype of the cells. Such molecules include mRNA transcribed from DNA, proteins translated from mRNA, and various metabolites of small molecular mass generated by various enzymatic activities. (**figure 1**) While one might think that every biological process is dictated by DNA sequence, the vast majority of genetic information leads to minimal insight into the functionality of biomolecules and the regulatory mechanisms involved in generating such molecules.[3] To explore all aspects of cellular processes, the last decade has witnessed significant growth in bioanalytical technologies

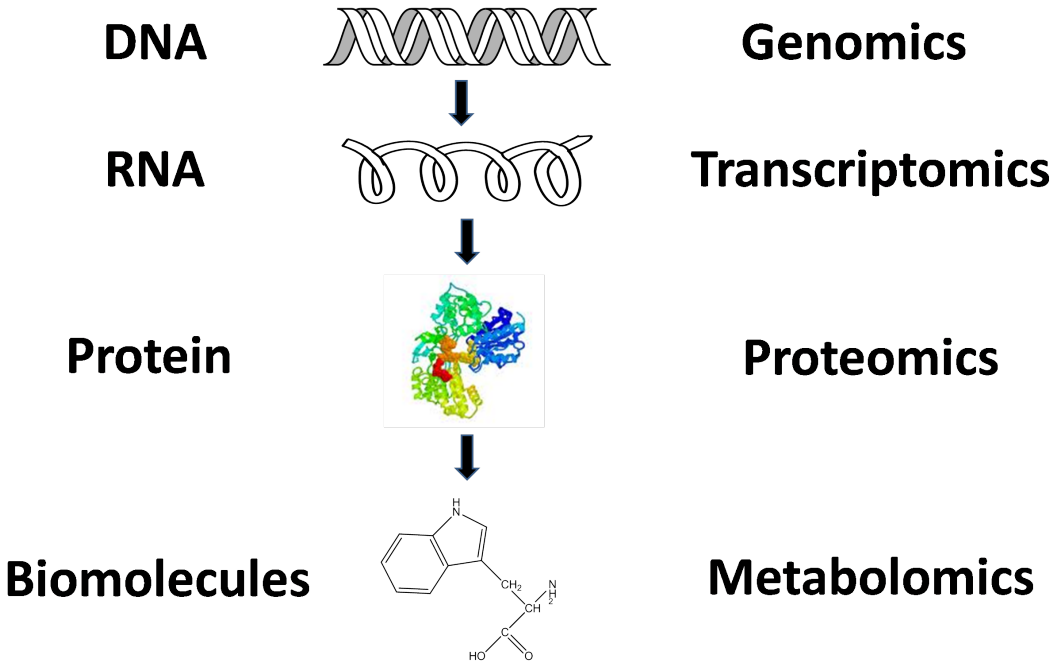

Figure 1. Schematic of the Fundamental Principles of Biological Processes.

pertaining to molecular biology assays in order to measure various cellular molecules including mRNA, proteins and metabolites. This evolution has led to the generation of several new 'omic' research fields including transcriptomics, proteomics, metabolomics, and so on.[4] These 'omic' experimental approaches exhibit three key characteristics beginning with a non-traditional shotgun, top-down experimental methodology.[4] Secondly, 'omic' research attempts to understand the 'whole-picture' or the grand 'integrated system' by incorporating cross-correlated interactions between a vast array of molecular species.[5] Finally, all emerging 'omic' research features a high-throughput approach that generates large waves of data that require significant statistical and computational processing. Collectively, the 'omic' field of research is driving the development of many sensitive and high-throughput bioanalytical techniques that rely on

the emerging field of 'bioinformatics' to classify, evaluate and transfer interrelations into systems biological models for conceptual analysis.[6]

While many believe the term 'omic' to be of Greek origin, there are no such correlations. Genomics was the foundation of "omic" research notation and was derived from a combination of the words 'gene' and 'chromosome' which indicated the complete set of chromosomes, and the genes contained in them. The 'omics' field has emerged as meaning an approach capable of generating a comprehensive data set.

In 1980, the Department of Energy (DOE) and the National Institute of Health (NIH) initiated the Human Genome Project (HGP) with an ultimate goal of accurately sequencing the human genome.[7] By 2003, the complete human genome was elucidated and accessible by all.[7] Without the rapid advances in capillary electrophoresis (CE) and capillary array electrophoresis (CAE), the HGP would not have been achieved two years ahead of schedule. Although CE research began in the early 1960s, investment in the technique did not become popular until advanced methods of DNA sequencing, namely CAE, began to emerge in the mid 1990s.[8,9] Still today, CAE continues to be the gold standard for genomic research and one will find benchtop CAE DNA sequencers in most molecular biology research departments. Currently, bioanalytical techniques in genomics are developing more from an engineering standpoint that aims to increase throughput and reduce overall time and cost of analysis. Eventually, genetic screening will be an integral part of an individual's medical assessment.

With the discovery of the human genome, also came an influx in proteomic research and development. The first reported proteomic analysis utilized nanometal particle assisted laser desorption mass spectrometry to obtain large biomolecular spectra

that could be correlated to protein molecular weight.[10] Shortly after, emergence of matrix-assisted laser desorption/ionization (MALDI) time-of-flight (TOF) mass spectrometry (MS)[11] and electrospray ionization (ESI) mass spectrometry[12] began to be the cornerstones for proteomic analysis. Implementation of proteolytic enzymes such as tyrpsin and chymotrypsin allowed for discrete peptide identification and the introduction of collision-induced dissociation (CID) provided the necessary means of secondary fragmentation (MS^2) for amino acid assignment.[13] Current proteomic techniques have evolved at a similar if not faster rate than genomic instrumentation but the cost of proteomic instrumentation (primarily MS technology) as a whole has not followed such a trend. New approaches to multi-dimensional online chromatography and nanoscale capillary chromatography have drastically reduced sample preparation as well as increased sample throughput. A current need is the development and validation of methods to decipher post-translational modifications with high accuracy. Additionally, the emergence of bioinformatics as a data interpretation tool shows promise for future bioanalytical approaches in proteomic research.[13]

The next emerging research area is that of transcriptomics. Transcriptomics builds on the knowledge of genomes. Although the genome is basically the same in every cell of an organism, different cells show different patterns of gene expression to serve various physiological functions but also to respond to external stimuli, such as chemical stressors.[14] The term 'gene expression' refers to the synthesis, or transcription, of RNA from a gene; thus, the transcriptome constitutes a snapshot of all actively expressed genes at any given time. An overwhelming amount of transcriptomic research revolves around new advances in DNA microarray technology that utilizes

complementary DNA (cDNA) detection strategies.[15] Microarray analysis continues to evolve at a rapid rate due to the popularity of commercial platforms and the wealth of data that is acquired. Next generation RNA sequencers are currently being developed and will eventually overcome most of the current limitations. RNA sequencers will eventually overcome most of the current limitations and allow for whole transcriptome shotgun sequencing that will enable the assembly of full cellular transcripts for a single sample.[16] Furthermore, digital acquisition of sequence reads will ultimately provide a reliable quantitative assessment over a wide range of expression levels with detection limits down to a few transcripts per cell without the need for any previous knowledge of the transcript of interest.[17]

Until recently, 'omic' areas of research were narrowly defined by large biomolecules of > 1500 Daltons that are associated directly or indirectly involved in gene expression but in 1999, the term, metabolomics was coined.[18] Metabolomics is defined as the quantitative measure of the dynamic multiparametric metabolic response of living systems to pathophysiologic stimuli or genetic modification and is concerned with the high throughput identification and quantitation of the small molecule metabolites of the metabolome.[19] The metabolome constitutes the interaction between small molecules, such as metabolic substrates and products, lipids, small peptides, vitamins and other protein cofactors.[20] The profiling of metabolites was first reported in the early 1950s with little progress for the next half century.[21]

Many recent developments in metabolomics have occurred due to major advances in analytical techniques (LC-MS, LC-NMR) and bioinformatics tools (Chemometrics).[20] Nuclear magnetic resonance spectroscopy (NMR)-based metabolomics offer key

advantages over MS techniques due to nondestructive, cost-effective and quick sample preparation and analysis. For the majority of cellular metabolites, LC-MS or GC-MS are the primary means of quantitative analysis with each offering high selectivity and sensitivity.[22] Metabolomic research and technology is grossly immature in comparison to genomics or proteomics but this is to be expected due to the drastic chemical diversity of cellular metabolites. Each 'omic' technology evolves to identify and quantitate a specific analyte such as individual nucleotides, tryptic digest peptides or RNA/cDNA fragments. Metabolomics on the other hand requires a vast array of analytical techniques that range from enzyme-immobilized electrochemical detection to simple UV/vis spectroscopy.[23] The likelihood of condensing such a large number of analytical methods into a single high-throughput technique is very unlikely with the only possible exception attributed to exponential development of microfluidic devices. This highlights the major hurdle for metabolomics which is the absence of a singular technique for high-throughput global analysis of the total cellular metabolic state.

The emergence of 'omic' focused research has dramatically changed the field of chemical biology to exist as a vastly networked collaboration of disciplines including biochemistry, cellular biology, biophysics, bioengineering, biostatistics and bioinformatics. Each of these disciplines exists under the confines of systems biology as we know it today. The direction of future innovation lies somewhere between platform miniaturization for single cell measurements and a convergence of interdisciplinary analytical methods and materials. Genomics and transcriptomics will likely become microchip-based sequencing techniques that become incorporated in limitless aspects of our lives. Analytical methods in proteomic research will be greatly enhanced by new

innovative separation techniques both online and offline coupled with high resolution mass spectrometry (HR-MS). The current field of metabolomics has already begun to dismantle into their respective focus of research, such as lipidomics or interactomics.[24] Of all the 'omic' fields of study, metabolomics leaves much to be desired in all aspects including metabolic flux, metabolite kinetics and phenotypic metabolic signatures, to name a few. The analytical tools needed to elucidate the metabolome can only be developed with continued collaboration across all areas of life science.

As analytical approaches to chemical biology continue to evolve, systems biology continues to amass key pieces to the overall puzzle of cellular complexity. The following chapters represent pieces to that puzzle. In **chapter two**, multi-dimensional LC-MS was performed to identify non-enzymatic fatty acid oxidation products associated with schistosomal hemozoin. In **chapter three**, multianalyte microphysiometry was employed to electrochemically measure macrophage energy metabolism changes in response to HNE exposure and PMA activation in real-time. To conclude, **chapter four** details the design, characterization and validation of a novel DNA-coated gold nanoparticle probe for identification and phenotypic classification of metastatic melanoma. While different in their own right, each study builds on the use and development of bioanalytical techniques and reporting biomaterials.

References

1. Zak, D. E.; Aderem, A. *Immunol Rev* **2009**, *227*, 264-82.

2. Ramsey, S. A.; Gold, E. S.; Aderem, A. *EMBO Mol Med* **2010**, *2*, 79-89.

3. Deckwer, W. D.; Jahn, D.; Hempel, D.; Zeng, A. P. *Eng. Life Sci.* **2006**, *6*, 455-469.

4. Zhang, W.; Li, F.; Nie, L. *Microbiology* **2010**, *156*, 287-301.

5. Ishii, N.; Tomita, M. *Science* **2007**, *316*, 593-597.

6. Wagner, P. *Current Opinions in Chemical Biology* **2003**, *7*, 592-594.

7. Venter, J. C. *Science* **2001**, *291*, 1145-1434.

8. Song, E. J.; Babar, S. M. E.; Oh, E.; Hasan, M. N.; Hong, H. M.; Yoo, Y. S. *Electrophoresis* **2008**, *29*, 129-142.

9. Babu, S.; Song, E. J.; Babar, S. M. E.; Wi, M. H.; Yoo, Y. S. *Electrophoresis* **2006**, *27*, 97-110.

10. Tanaka, K.; Yaki, H.; Ido, Y.; Akida, S.; Yoshida, Y.; Yoshida, T. *Rapid Commun. Mass Spectrom.* **1988**, *2*, 151.

11. Karas, M.; Hillenkamp, F. *Anal Chem* **1988**, *60*, 2299-301.

12. Wong, S. F.; Men, C. K.; Fenn, J. B. *J. Phys. Chem.* **1988**, *92*, 516.

13. Chen, C. H. *Analytica Chimica Actat* **2008**, *624*, 16-36.

14. Schirmer, K.; Fisher, B. B.; Madureira, D. J.; Pillai, S. *Anal. Bioanal. Chem.* **2010**, 214-228.

15. Tan, D. S.; Lambros, M. B. K.; Natrajan, R.; Reis-Filho, J. S. *laboratory Investigation* **2007**, *87*, 737-754.

16. Cui, Y.; Paules, R. S. *Phamacogenomics* **2010**, *11*, 573-585.

17. Meng, Z.; Limbach, P. A. *Functional Genomics and Proteomics* **2006**, *5*, 87-95.

18. Nicholson, J. K.; Lindon, J. C.; Holmes, E. *Xenobiotica* **1999**, *29*, 1181.

19. Goodacre, R.; Vaidyanathan, S.; Dunn, W. B. *Trends Biotechnol.* **2004**, *22*, 245.

20. Goldsmith, P.; Fenton, H.; Morris-Stiff, G.; Ahmad, N.; Fisher, J.; Prasad, K. R. *Journal of Surgical Research* **2010**, *160*, 122-132.

21. Rochfort, S. *J. Nat. Prod.* **2005**, *68*, 1813-1820.

22. Dettmer, K.; Aronov, A. P.; Hammock, B. D. *Mass Spectrom Rev* **2007**, *26*, 51.

23. Eklund, S. E.; Snider, R. M.; Wikswo, J.; Baudenbacher, F.; Prokop, A.; Cliffel, D. E. *J. of Electroanalytical Chemistry* **2006**, *587*, 333-339.

24. Astarita, G.; Ahmed, F.; Piomelli, D. *Methoeds in Molecular biology* **2009**, *579*, 201-219.

CHAPTER II

IDENTIFICATION OF HYDROXYEICOSATETRAENOIC ACID COMPONENTS OF SCHISTOSOMAL HEMOZOIN[1]

Introduction

Schistosomiasis is a parasitic disease that chronically infects over 200 million people in 74 countries and is responsible for more than 200,000 deaths each year.[3-5] Based on recent reports, schistosomiasis ranks second only to malaria as a cause for chronic morbidity among tropical diseases.[6] Parasitic infection by *Schistosoma mansoni* occurs via a complex digenetic life cycle consisting of skin penetration by free-swimming

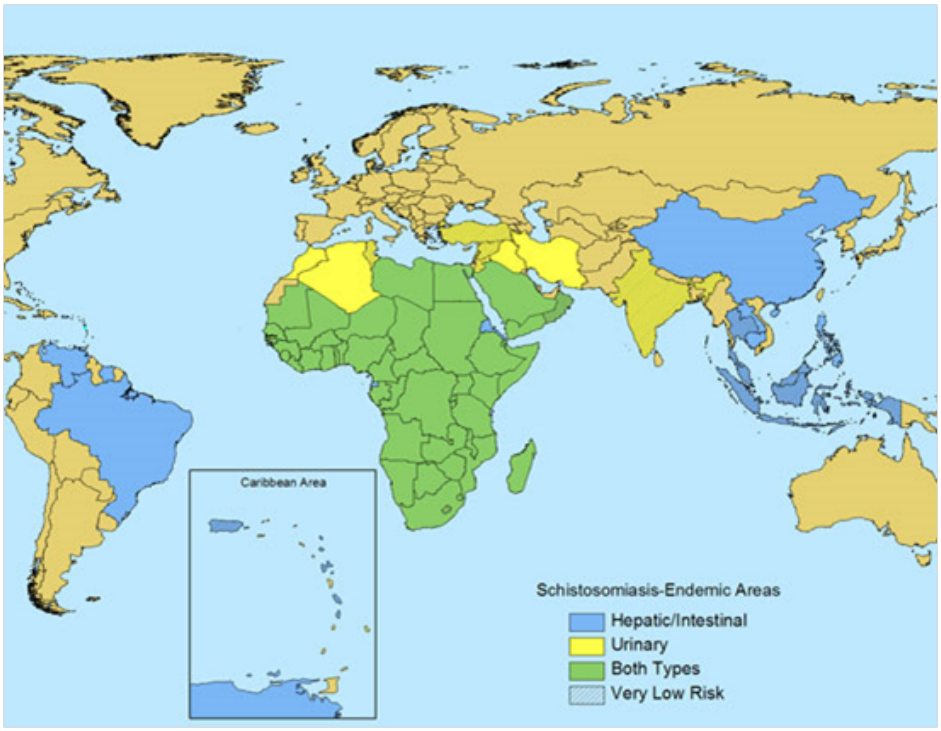

Figure 2. Worldwide Distribution of Schistosomiasis

cercariae that are released from infected aquatic snails of the genus *Biomphalaria*, followed by migration, maturation, and sexual reproduction in the host's vascular system. Schistosome eggs typically deposit in the intestinal tissue and are excreted in the feces. The life cycle is completed once excreted eggs reach freshwater and hatch into free-swimming miracidia, which, in turn, reinfect the intermediate snail hosts.

S. mansoni is the primary species responsible for vertebrate schistosomiasis and like other blood feeding organisms such as *Plasmodium falciparum* (malaria)[7] and *Haemoproteus columbae* (avian malaria)[8], the blood fluke catabolizes host hemoglobin (Hb) in order to obtain requisite amino acids for growth and development. While residing in the hepatic portal system, adult schistosomal worms ingest large quantities of host red blood cells (RBCs). In fact, it is estimated that mature female schistosomes consume up to 330,000 RBCs per hour.[9] Erythrocytic Hb is broken down by proteolytic enzymes in the gut and the current paradigm suggests that heme is an end-product of Hb digestion.[8] Although heme is an essential molecule for most living organisms, high concentrations of free heme are thought to elicit deleterious pro-oxidant effects such as free radical formation, hemolysis,[10] and lipid peroxidation.[11] In order to evade the cytotoxic effects of free heme, blood feeding organisms have developed novel mechanisms of heme detoxification. In the protozoan *P. falciparum*, toxic free heme accumulates in the digestive food vacuole and is sequestered by aggregation into an inert crystalline pigment called hemozoin (Hz).[7] *S. mansoni* employs a similar heme detoxification pathway. During hemoglobin breakdown in the digestive cavity of the trematode, free heme aggregates and the subsequent pigment is regurgitated by the parasite into the surrounding host vasculature. The dark-brown pigment produced during

S. mansoni infection has long been speculated to consist of a dimeric heme core and in a recent study by Oliveira and coworkers, X-ray powder diffraction studies unequivocally revealed that schistosomal pigment is structurally identical to *P. falciparum* hemozoin and its synthetic analogue, β-hematin (BH).[12,13]

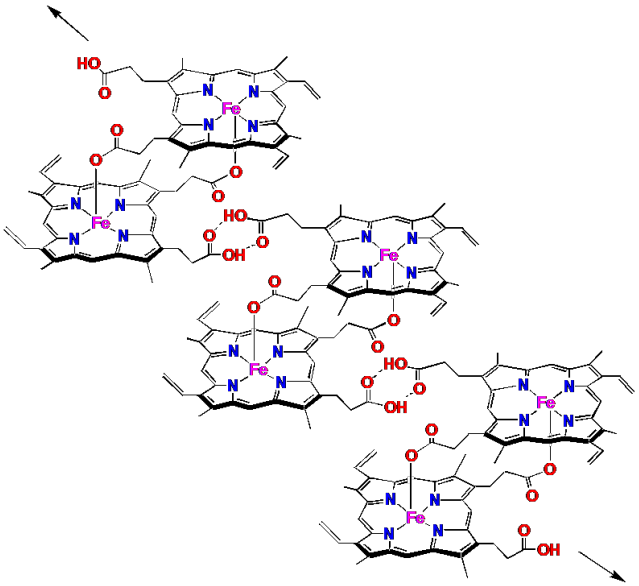

Figure 3. Chemical Structure of Hemozoin

The chemical structure of hemozoin (**figure 3**) consists of heme (protoporphyrin IX) dimers linked by the binding of the central iron of the first porphyrin ring to one of the propionic side chains of the reciprocating porphyrin. An extended crystalline network is formed via hydrogen bonding between free propionic acid side chains followed by precipitation in solution. The structure of hemozoin was first demonstrated

by Pagola *et al*. from high-resolution synchrotron X-ray powder diffraction studies and was confirmed using isotope enriched Raman and IR spectroscopy.[14,15]

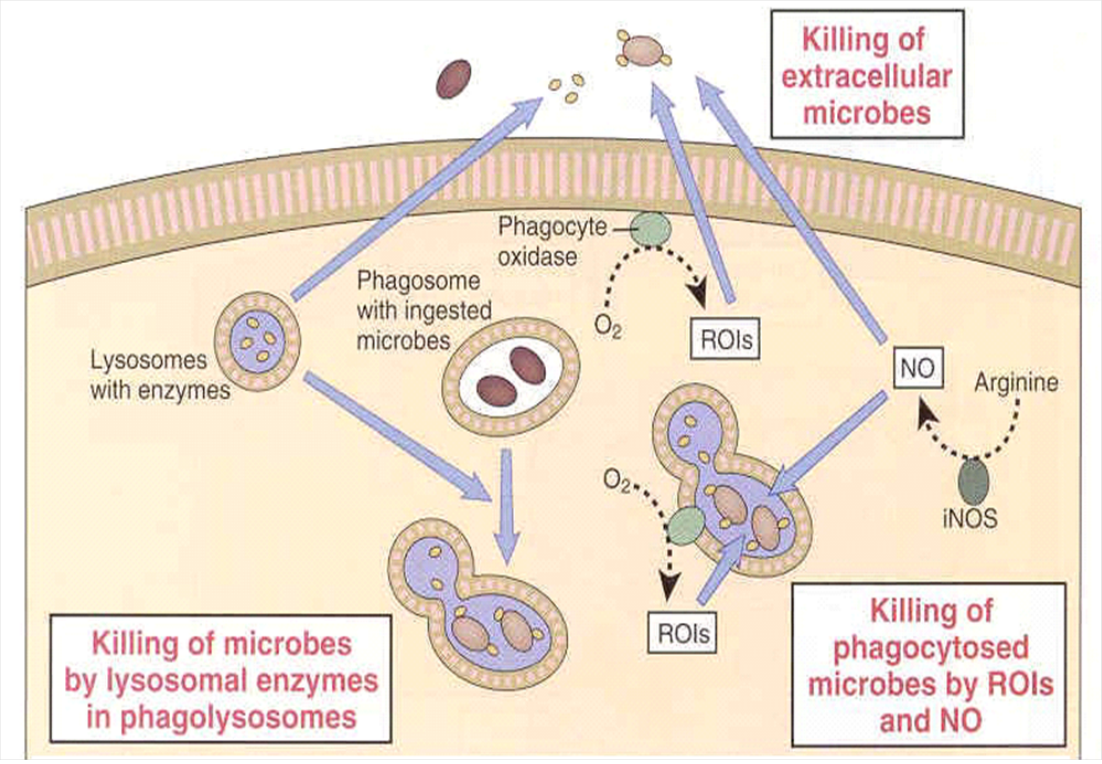

Figure 4. Phagocytic funtion in response to extracellular microbial challenge.
(Copywrite, Elsevier 2000)[2]

Upon regurgitation from the gut of the worm, hemozoin is released into the vasculature triggering an immune response by professional phagocytes. Macrophages and neutrophils engulf the particulate, known as phagocytosis, in order to eradicate the foreign substance from the body. Hz has long been considered an inert, detoxification end-product, but previous studies suggest that native hemozoin is capable of modulating host immunity. Schwarzer and coworkers showed that phagocytosis of native hemozoin from *P. falciparum* disrupts the normal cellular function of human monocytes *in vitro*.[16,17] The accumulation of native hemozoin in circulating monocytes (macrophages

and neutrophils) inhibits normal phagocytic function by inducing oxidative stress and down regulating intercellular mechanisms that generate potent oxidative molecules used to defend against foreign invaders, namely reactive oxygen species (ROS) and reactive nitrogen species (RNS).[18] (**figure 4**) Furthermore, Hz has also been shown to induce lipid peroxidation via the non-enzymatic iron-catalyzed oxidation of polyunsaturated fatty acids (PUFAs) resulting in the formation of several potent, cytotoxic and immunosuppressive molecules including hydroxyeicosatetraenoic acids (HETEs)[11,16,19] and 4-hydroxy-2-nonenal (HNE).[20,21]

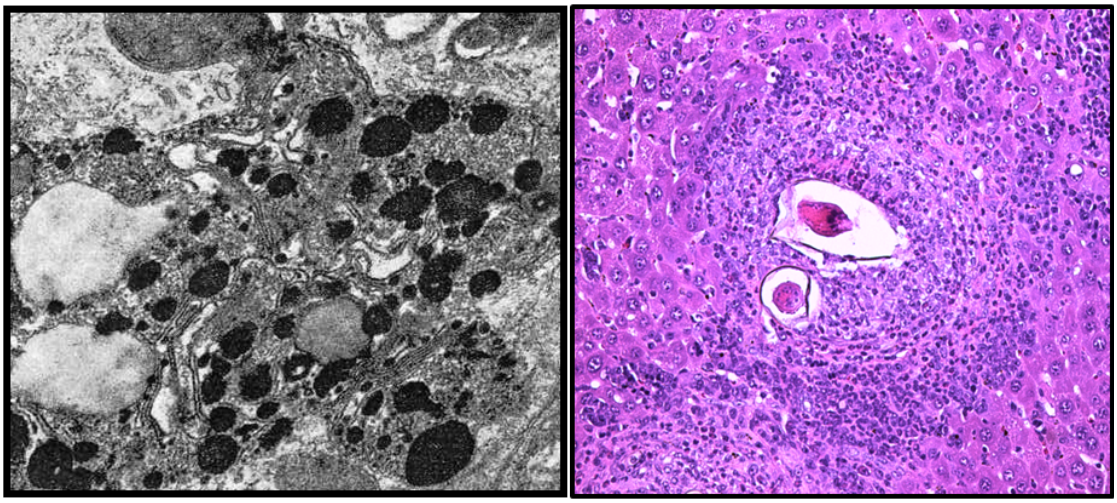

Figure 5. Schistosomal hemozoin and parasitic egg deposition in Schistosomiasis pathology. (Left) Transmission electron micrograph of a *S. mansoni* hemozoin-laden kupffer cell. (Right) Haematoxylin and eosin stained liver section of an embedded schistosome egg surrounded by granuloma-associated tissue.

In human schistosomiasis, disease related pathology is primarily a result of the host's cell-mediated response to antigens released by entrapped parasite eggs in the liver.[22] (**figure 5**) The schistosome egg-induced granulomatous response leads to severe inflammation, tissue eosinophilia, collagen deposition, and, ultimately, extensive hepatic

fibrosis.[22] Schistosomal pigment has long been observed in granulomatous liver tissue. In a recent study, the majority of hepatic granulomas observed in naturally infected *Nectomys squamipes* consisted of large macrophages filled with schistosomal Hz.[23] Consequently, Hz-mediated production of arachidonic acid (AA) metabolites, such as HETEs and HNE, are of significant interest in schistosomiasis since the role of Hz in the disease's pathogenesis remains largely unexplored.

Experimental

Materials

S. mansoni infected Swiss-Webster mice were provided courtesy of Dr. Fred Lewis and the NIAID Schistosomiasis Resource Center (NIH-NIAID contract AI-30026) (Rockville, MD, USA). Hydroxyeicosatetraenoic acid (HETE) standards were purchased from Cayman Chemical Company (Ann Arbor, MI, USA). RPMI 1640, penicillin, and streptomycin were obtained from Cellgro Mediatech, Inc (Herdon, VA, USA). Arachidonic acid was obtained from Nu-Chek Prep Inc. (Elysian, MN, USA). 4-hydroxy-2-nonenal (HNE) was purchased from Calbiochem (San Diego, CA, USA). Lipopolysaccharide (LPS) (*E. coli* 055:B5), chelex, sulfanilamide, N-(1-naphthyl)ethylenediamine (NED), 2,6-lutidine, ethyl acetate, 2,6-di-tert-butyl-4-methylphenol (BHT) and hemin chloride (Fluka-brand, >98%) were all purchased from Sigma-Aldrich (St. Louis, MO, USA). All chemicals were used as received unless otherwise noted.

β-hematin synthesis

β-hematin (BHz), the synthetic version of Hz, was synthesized via the method of dehydrohalogenation of hemin, as described by Bohle and Helms. Briefly, in an inert atmosphere, hemin chloride (0.75 mmol) was dissolved in a minimal volume of 2,6-lutidine and stirred vigorously for 10 min. Upon complete dispersion, a 20 ml volume of 50:50 anhydrous methanol:dimethylsulfoxide (v/v) was added to the hemin chloride solution. The reaction vessel was then sealed, protected from ambient light, and allowed

to stand undisturbed for 3 months. Upon completion, the reaction mixture was filtered and the resulting precipitate was washed exhaustively with excess methanol, 0.1 M sodium bicarbonate (pH 9.1) and deionized water. After drying overnight at 150^{o}C, the dark brown precipitate was alternately washed with deionized water and 0.1 M sodium bicarbonate (pH 9.1) until the supernatant was free of residual heme. The identity of the final product was confirmed by x-ray diffraction (XRD), fourier-transform infrared spectroscopy (FT-IR), and scanning electron microscopy (SEM).

SmHz Isolation

Adult schistosomes were obtained by mesenteric perfusion of mice 42 days after infection as previously described. Freshly cultivated adult female worms were homogenized under sterile conditions in phosphate buffered saline (PBS, pH 7.4) using a standard 15 mL glass homogenizer. The resulting homogenate was centrifuged twice at 1000 x g for 60 s to remove worm tissue from the suspension. The tissue pellet was removed and the resulting supernatant was centrifuged at 5500 x g for 2 h. The resulting dark-brown pellet was resuspended in 5 mL of sterile PBS (pH 7.4) after vortexing and gentle sonication for 5 min. SmHz content was quantitated as described by Sullivan *et al.* [24]. Briefly, SmHz was incubated with 20 mM NaOH + 2% SDS at room temperature for 2 h to degrade the reciprocating iron-propionate linkages. Heme content was determined from the absorbance at 400 nm ($\varepsilon = 1 \times 10^5$ $M^{-1}cm^{-1}$) using an Agilent 8453 UV-Visible Spectrophotometer.

Native SmHz lipid extraction

The native *Sm*HZ lipid component was extracted twice from 2.5 mg/mL native *Sm*HZ in 25 mM chelexed-phosphate buffer (pH 7.4) using 1:1 (v/v) ethyl acetate. The emulsion was vortexed 60 s and centrifuged 30 min at 5445 x g. The organic layer was removed and evaporated under nitrogen. The lipids were reconstituted in 1 mL of ethanol and stored at -80°C.

In vitro Hz-mediated HETE production

Purified native *Sm*HZ, complete removal of lipids confirmed by NP-HPLC, was used in all experiments. The reaction was performed by adding 5.32 mM AA to a 2 mL suspension of either *Sm*HZ or BH (0.3 mg/mL) in 25 mM chelexed-phosphate buffer (pH 7.4) for 4 h at 25°C. Reaction products were extracted with ethyl acetate and stored in ethanol at -80°C.

LC-MS/MS HETE identification.

HETE standards and lipid samples were dried under nitrogen and resuspended in acetonitrile/water (30:70), 10 mM ammonium carbonate and 0.1 M BHT prior to injection. The LC-MS/MS analysis was performed on a Waters Acquity UPLC system (Waters, Milford, MA) connected to a Thermo Fisher Scientific, Waltham, MA) using a Thermo Hypersil Gold C18 column (1.9 μm, 2.1 x 150 mm). LC conditions were as follows: solvent A contained 10 mM ammonium carbonate in acetonitrile/water (10:90) and solvent B contained 10 mM ammonium carbonate in acetonitrile/water (10:90). The following gradient program was used with a flow rate of 600 μL/min: 0-0.25 min, 30%

B; 0.25-9 min, linear gradient 30-45%; 9-10 min, 45% B; 10-10.50 min, linear gradient 45-30% B; 10.50-17 min, 30% B. Sample injection volume was 10 µL. The following optimized parameters were used for the detection of analyte and internal standard: N_2 sheath gas 36 psi; N_2 auxiliary gas 20 psi; capillary temperature 300°C; source voltage 3.8 kV; source current 100 µA; skimmer offset 0.00 V; capillary offset -44.00 V; tube lens offset -103.30 V; activation time 30 ms (MS), 50 ms (MS^2); isolation width 1 *m/z* (MS), 2 *m/z* (MS^2). Data acquisition and quantitative spectral analysis was conducted using the Thermo-Finnigan Xcaliber software, version 2.0 Sur 1.

LC-MS/MS chiral separation.

Normal phase LC (NP-LC) analysis was performed prior to chiral RP-LC-MS/MS in order to isolate HETE isomers for individual analysis. The NP-LC was performed on a Waters 600 HPLC connected to a Waters 996 photodiode array (Waters, Milford, MA) using a Beckman Ultrasphere silica column (5 µm, 4.6 mm x 25 cm; Beckman Coulter, Fullerton, CA). An isocratic gradient of 98.8% hexane, 1.2% isopropanol and 0.1% acetic acid was used at a flow rate of 1.00 mL/min. HETE absorbance was detected at 237 nm.

Chiral-RP-LC-MS/MS.

The LC-MS/MS analysis was performed as before using a CHIRALPAK AD-RH column (5 µm, 2.1 mm x 150 mm; Chiral Technologies, Inc., West Chester, PA). LC conditions were as follows: solvent A contained 0.25% formic acid in acetonitrile/water (5:95) and solvent B contained 0.25% formic acid in acetonitrile/water (95:5). The

following gradient program was used with a flow rate of 200 μL/min: 0-5 min, 50% B; 5-20 min, linear gradient 50-100% B; 30-32 min, 50% B. The following optimized parameters were used for the detection of analyte and internal standard: N_2 sheath gas 36 psi; N_2 auxiliary gas 20 psi; capillary temperature 300°C; source voltage 3.8 kV; source current 100 μA; skimmer offset 0.00 V; capillary offset -44.00 V; tube lens offset -103.30 V; activation time 30 ms (MS), 50 ms (MS^2); isolation width 1 *m/z* (MS), 2 *m/z* (MS^2). Data acquisition and quantitative spectral analysis were conducted using Thermo-Finnigan Xcaliber version 2.0 Sur 1.

Cell Cultures

The RAW 264.7 murine macrophage cell line was cultured in RPMI 1640 supplemented with 4 mM L-glutamine, 100 units/ml penicillin/streptomycin, and 10% (v/v) fetal bovine serum. Before each experiment, the cells were incubated overnight at 37°C in a 95% air / 5% CO_2 atmosphere and washed once with sterile PBS (pH 7.4) before performing the appropriate experiment. Cell viability was confimed by Trypan Blue exclusion.

iNOS Inhibition Experiments

The inhibitory effects of (5-, 12-, 15-) HETE, HNE, and schistosomal Hz on LPS-stimulated iNOS activity in RAW 264.7 cells was examined. RAW 264.7 cells were plated at a density of 1×10^5 cells/well in 96-well culture plates and incubated at 37°C in a 5% CO_2 atmosphere for ≥8 h. To determine the inhibition by 5-, 12-, and 15-HETE, stock solutions of each isomer were prepared by evaporating each 100 μg vial to near

dryness under nitrogen and reconstituting in RPMI complete medium, paying close attention to keep ethanol concentrations below 0.5 % (v/v). Concentrations were determined for each HETE stock solution by measuring the absorbance at 236 nm (ε = 2.7 ± 10^4 $M^{-1}cm^{-1}$). Cell cultures were treated with increasing concentrations of HETE (0-20 μM) and stimulated with LPS at a final concentration of 1 μg/mL. To determine the inhibition by schistosomal Hz, stock solutions of 0.1 mg/mL schistosomal Hz, 0.1 mg/mL βHz and 17.5 μM HNE were prepared in RPMI complete medium. Cell cultures were treated with each stock solution and stimulated with LPS at a final concentration of 1 μg/mL. Cell cultures were incubated at 37°C in a 5% CO_2 atmosphere and NO concentrations were determined after 24 h. All iNOS inhibition experiments were performed in quadruplet and are reported as the average value with standard deviations.

Nitric Oxide Measurements

Nitric oxide (NO) generation was determined by measuring the concentration of nitrite (NO_2^-), a stable NO oxidation product, in cell culture supernatants using the Greiss reaction. After an incubation period of 24 h, the cell culture supernatant was removed and clarified by centrifugation at 13,200 x g for 5 min. The reaction was performed by transferring 100 μl of the supernatant to a 96 well plate and adding 50 μl of 1% sulfanilamide in 5% phosphoric acid followed by 50 μl of 0.1% N-(1-naphthyl)ethylenediamine (NED). After incubation for 5 min at room temperature, the absorbance of the resulting azo complex was measured at 540 nm using a Bio-Tek Synergy HT Multidetection Microplate Reader. NO_2^- concentrations were calculated using a $NaNO_2$ standard curve.

Scanning electron microscopy

Dry purified *Sm*HZ was suspended in ethanol, sonicated for 10 min, applied to a polished aluminum specimen mount, and dried at 25°C overnight. Each sample was sputter-coated with gold for 20 s and imaged using a Hitachi S4200 scanning electron microscope at 5.0 kV accelerating voltage.

Fourier Transform Infrared Spectroscopy (FT-IR) / X-ray Powder Diffraction (XRD)

Fourier transform IR spectroscopy was performed in a KBr pellet using an ATI Mattson Genesis Series FTIR spectrophotometer. Powder X-ray diffraction scans were obtained on a Scintag X_1 θ/θ automated powder diffractometer with a Cu target and a Peltier-cooled solid sate detector. Samples were ground into a fine powder and placed evenly on a zero background Si (510) sample support. All measurements were performed at a wavelength of 1.54056 Å with a step size of 0.02^o in 2θ from 4^o to 50^o.

Results and Discussion

Schistosomal pigment (*Sm*HZ) is typically found accumulated in resident tissue macrophages of the liver. Adult worm pairs reside in the hepatic portal system of the host and regurgitate hemozoin and cellular debris into the surrounding vasculature. Adult female worms exhibit a much heavier degree of pigmentation relative to males due to the nutritional demands of oogenesis (**figure 6A**). Following perfusion of the hepatic portal vein in *S. mansoni*-infected Swiss Webster mice, adult female and male worms were separated, counted and homogenized to determine *Sm*HZ burden per worm as previously described.[25] On average, adult females were found to accumulate 1.729 ± 0.29 μg of hemozoin while the adult males were found to amass only 0.114 ± 0.07 μg per worm. Isolated *Sm*HZ was purified and characterized using X-ray powder diffraction

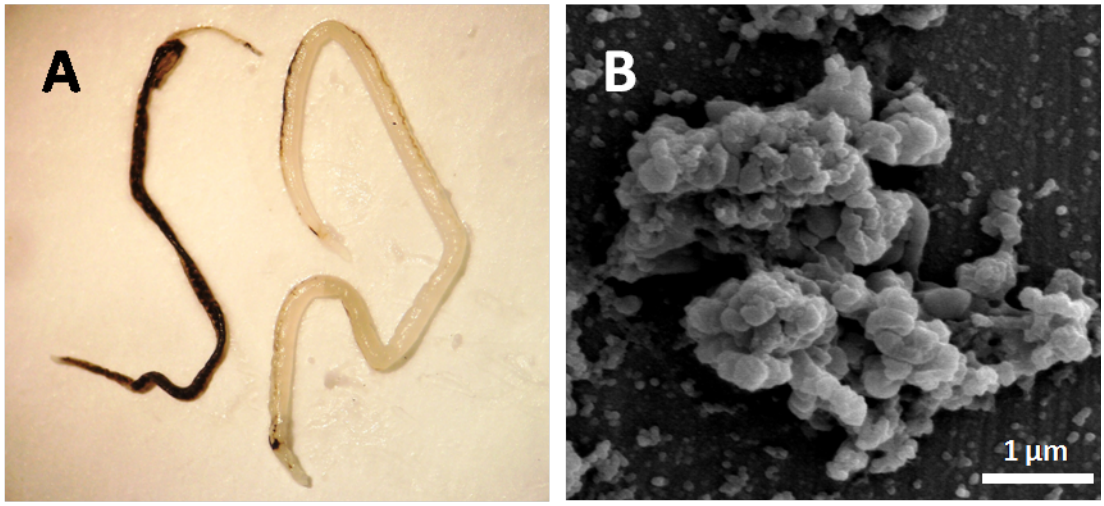

Figure 6 . Hemozoin from *S. Mansoni*. (A) Adult female (left) and male (right) *S. mansoni* laden with hemozoin. (B) SEM image of schistosomal hemozoin isolated from homogenized *S. mansoni.* (Copyright, Elsevier 2007)

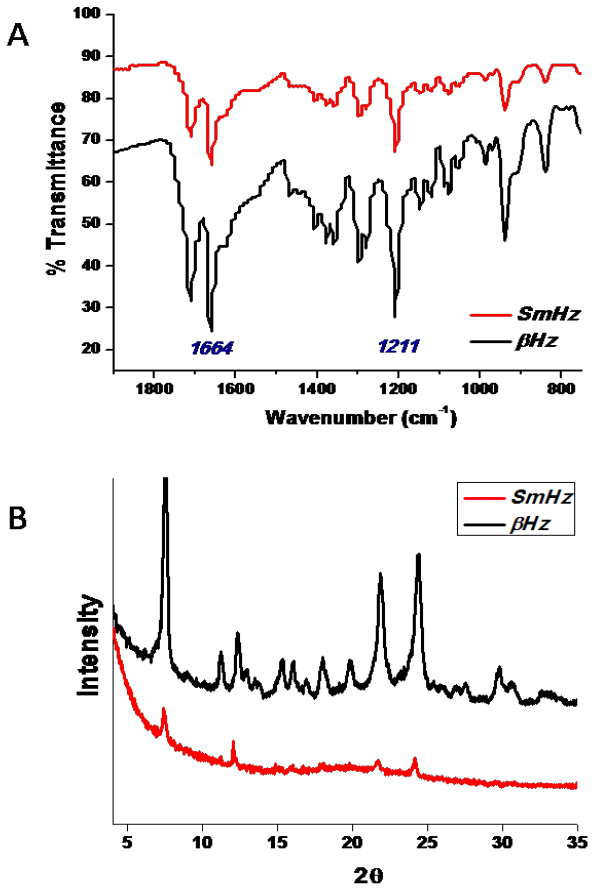

Figure 7. IR and XRD of HZ. (A) The presence of axial propionate linkages in HZ's dimeric ferriprotoporphyrin IX structure was confirmed using infrared spectroscopy showing the C-O stretching at 1211 cm^{-1} and C=O stretching at 1664 cm^{-1}. (B) Characterization by powder x-ray diffraction (Cu Kα radiation) reveals the 2:1 intensity of 2θ peaks at 7˚: 21˚ and 24˚. Reduced peak distinction compared to BH in *Sm*HZ pattern is attributed to limited sample size. (Copyright, Elsevier 2007)

(characteristic 2:1 intensity of the signature 2θ peaks at 7°: 21° and 24°) and Fourier transform infrared spectroscopy (1664 and 1211 cm^{-1} of C=O and C-O stretching) confirming a dimeric ferriprotoporphyrin IX aggregate identical to *Pf*HZ and BH (**Figure 7**). While *Pf*HZ and BH SEM images portray a biomineral of elongated rectangular crystals with well-defined crystal facets, *Sm*HZ images depict the characteristic

heterogeneous morphology and large size distribution often attributed to the extracellular environment of HZ formation in *S. mansoni* (**figure 6B**).[13]

The nature and function of the lipid environment surrounding the heme aggregate of native HZ is complex. In a recent study, transmission electron microscopy (TEM) showed the localization of *Sm*HZ at the hydrophilic-hydrophobic interface of lipid droplets in the *S. mansoni* gut lumen.[26] Similarly, Pisciotta and coworkers extracted a suite of neutral lipids coating native HZ from the digestive food vacuole of *P. falciparum*.[27] In both cases, the lipid extracts provided a competent scaffold for

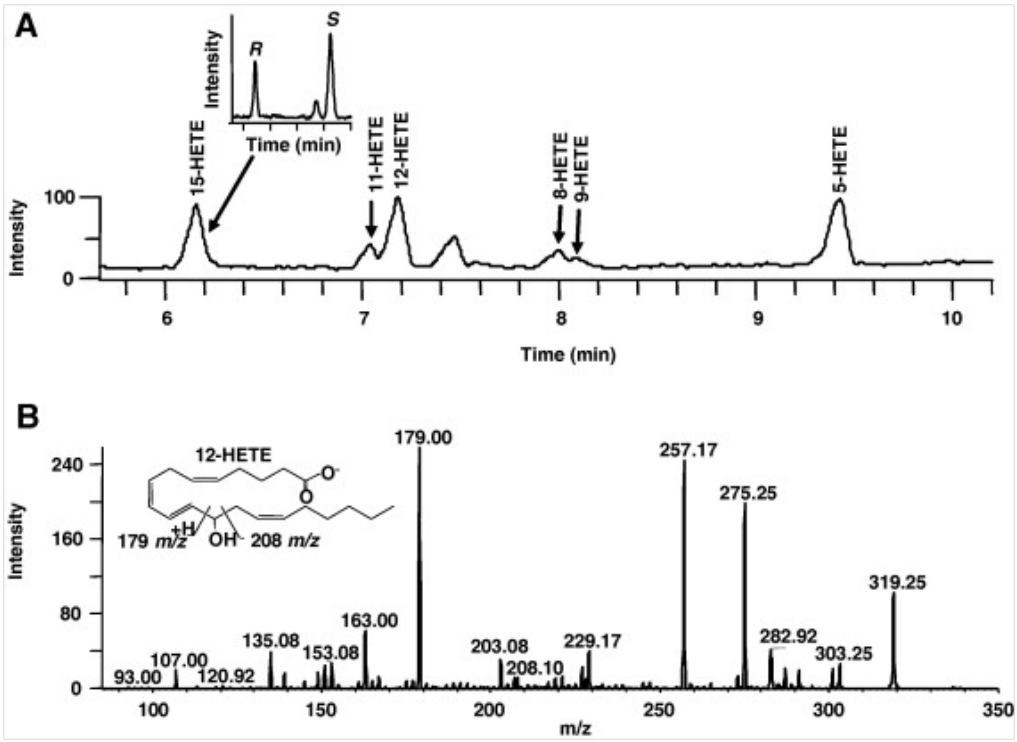

Figure 8. HETE-containing lipid coat of native *Sm*HZ. (A) Lipids were extracted from native *Sm*HZ using ethyl acetate, blown dry under $N_{2(g)}$ and redissolved in RP-LC-MS/MS mobile phase. All six hydroxylated fatty acid derivatives of arachidonic acid were identified (15-, 11-, 12-, 8-, 9- and 5-HETE). Insert shows the representative chiral resolution for 15-HETE (11.5 min. *R* and 14.5 min. *S*). (B) Representative MS/MS fragmentation for 12-HETE. All isomers were confirmed using authentic standards and extracted ion profiles from MS/MS. (Copyright, Elsevier 2007)

hemozoin formation *in vitro*. Polar hydroxylated fatty acids derived from arachidonic and linoleic acids have also been extracted from native *Pf*HZ, as has the secondary oxidation product HNE.[11,16,20] These compounds have been shown to be capable of significantly altering the function of macrophage cells during the course of malarial infection.

To investigate the presence of biologically active AA metabolites in native *Sm*HZ,

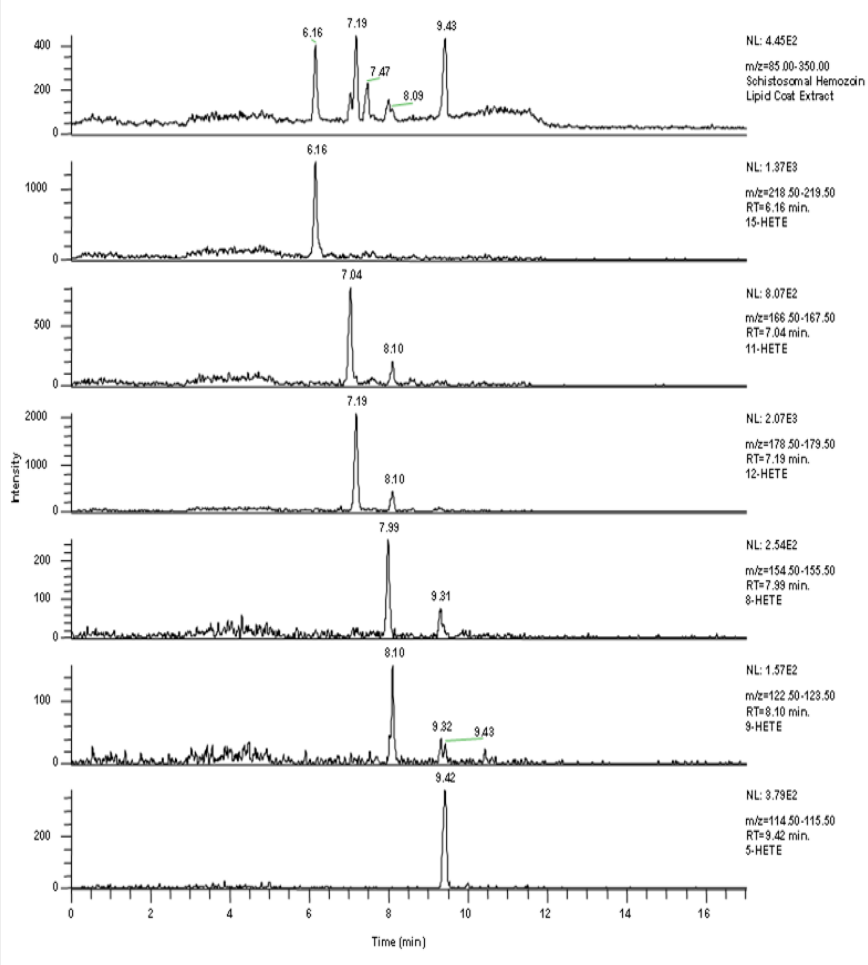

Figure 9. Extracted ion profile of *Sm*Hz lipid coat. The identification of all six positional isomers of HETE in the *Sm*Hz lipid coat was achieved by extracting the characteristic MS/MS fragment masses of each isomer from the collected 319 *m/z* reverse-phase-LC-MS ions. Individual isomers from the total ion chromatogram (A) of the *Sm*Hz lipid coat are shown: (B) 15-HETE at 6.16 min., (C) 11-HETE at 7.04 min., (D) 12-HETE at 7.19 min., (E) 8-HETE at 7.99 min., (F) 9-HETE at 8.10 min. and (G) 5-HETE at 9.42 min. Characteristic MS/MS fragments were confirmed using authentic HETE standards. (Copyright, Elsevier 2007)

the hydroxylated fatty acid component of native *Sm*HZ was isolated and analyzed by liquid chromatography-tandem mass spectrometry (LC-MS/MS). The identification of each HETE positional isomer peak was achieved using time dependent MS/MS in which the isobaric carboxylate $[M-H]^-$, 319 *m/z*, precursor ion was trapped and subsequently fragmented to give product ions of each HETE isomer (**figure 9**). All six HETE positional isomers derived from AA were observed in the *Sm*HZ lipid extract, with the most abundant species being 15-, 12- and 5-HETE ($[M-ROH]^-$: 219, 179 and 115 *m/z*, respectively) (**figure 8**). In contrast to previous HETE identifications in hemozoin producing parasites[16], the LC-MS/MS method presented herein is a marked advancement including MS/MS confirmation of all identified HETEs during separation and an increased instrument sensitivity reaching the femtomole range. Such a limit of detection is especially important when working with the extracted lipids of limited native Hz samples, as is the case of *S. mansoni* yields from Swiss Webster mice (1 mg *Sm*HZ/ 60 mice).

Chiral purity of biologically derived hydroxylated fatty acids is typically attributed to the lipoxygenase (Lox) family with preference usually shown for *S*-stereo-isomer products.[28-35] In the absence of Lox, however, free radical-mediated peroxidation of AA can yield a racemic mixture of each hydroxylated isomer. Given the presence of all six HETE isomers in the *Sm*HZ lipid coat, additional chiral analysis was performed to examine the enantiomeric chiral analysis was performed to examine the enantiomeric distribution of the monohydroxy derivatives. Chiral LC-MS/MS of the *Sm*HZ lipid extract revealed an equivalent stereoselective distribution of all HETEs with the exception of 12-*S*-HETE (**figure 10**). Based on integrated peak area, a 70:1 abundance of

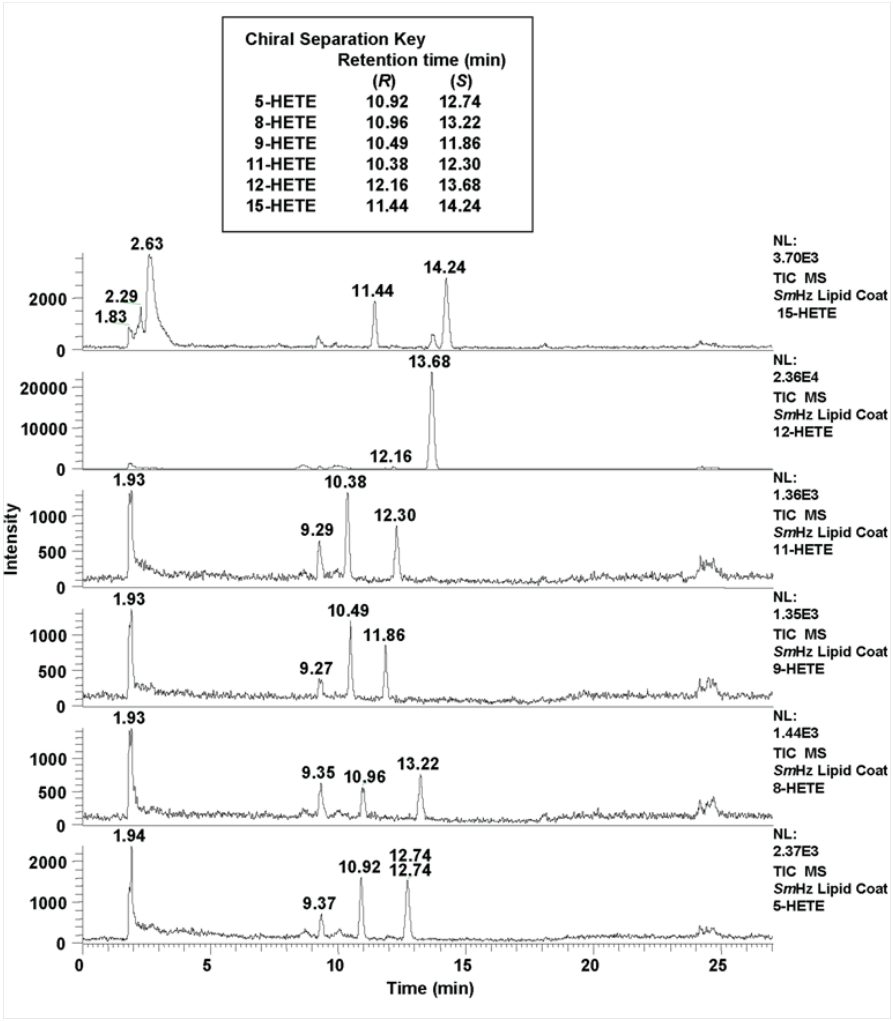

Figure 10. Chiral-RP-LC-MS/MS of *Sm*Hz lipid coat. *R* and *S* HETE enantiomers were separated using chiral-reverse-phase-LC-MS/MS (*R*- and *S*-HETE retention times shown in figure key). Each HETE isomer was identified by its characteristic MS/MS fragment masses as determined from authentic HETE standards. A 1:1 ratio was observed for all HETE enantiomers with the exception of 12-HETE which exhibited a 70:1 distribution of 12-*S*-HETE to 12-*R*-HETE. (Copyright, Elsevier 2007)

12-*S*-HETE to 12-*R*-HETE was observed suggesting accumulation of enzymatically produced HETE. This is in marked contrast to the equivalent stereoisomeric ratios observed for the 12-HETEs in the lipid coat of *Pf*HZ.[16] Previously, murine host 12-Lox activity has been described in the immunomodulation of schistosomiasis.[26,36] Three types of murine 12-Lox (epidermal-, leukocyte- and platelet-type 12-Lox) have been reported,

but none of these were observed in a recent proteomic analysis of gut contents from *S. mansoni*.[26,36] In *S. mansoni*, only the activity of a 15-*S*-Lox has been reported, although sequence analysis of the partially sequenced *S. mansoni* genome suggests the possible presence of a 12-*S*-Lox gene.[37] Regardless of the origin of the observed 12-*S*-HETE, the racemic mixture of all other HETE isomers is indicative of HZ-mediated lipid peroxidation of fatty acids.

In order to confirm the expected HZ-driven lipid peroxidation of fatty acids, *in vitro*, reactions of AA incubated with either purified *Sm*HZ or BH were performed under aerobic conditions. The resultant oxidized lipids were extracted and characterized by RP- and chiral-LC-MS/MS. Relative to AA controls, both purified *Sm*HZ and BH produced

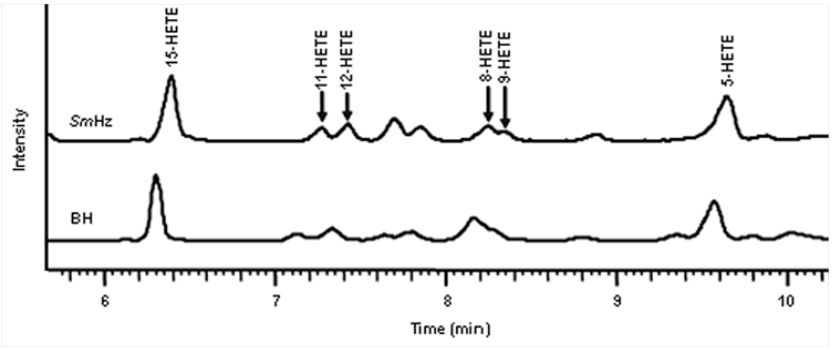

Figure 11. Hemozoin-mediated lipid peroxidation of arachidonic acid. Oxidation studies by incubation of 0.3 mg/mL BH or *Sm*HZ with 5.32 mM AA were conducted. The hydroxylated fatty acid isomers 15-, 11-, 12-, 8-, 9- and 5-HETE were identified in the reactions' lipid extracts using RP-LC-MS/MS. (Copyright, Elsevier 2007)

significant quantities of the six HETE positional hydroxylation isomers, with 15- and 5-HETE as the most prominent (**figures 11-13**). These findings are in good agreement with earlier literature concerning the reactivity of both purified *Pf*HZ and BH.[11,38]

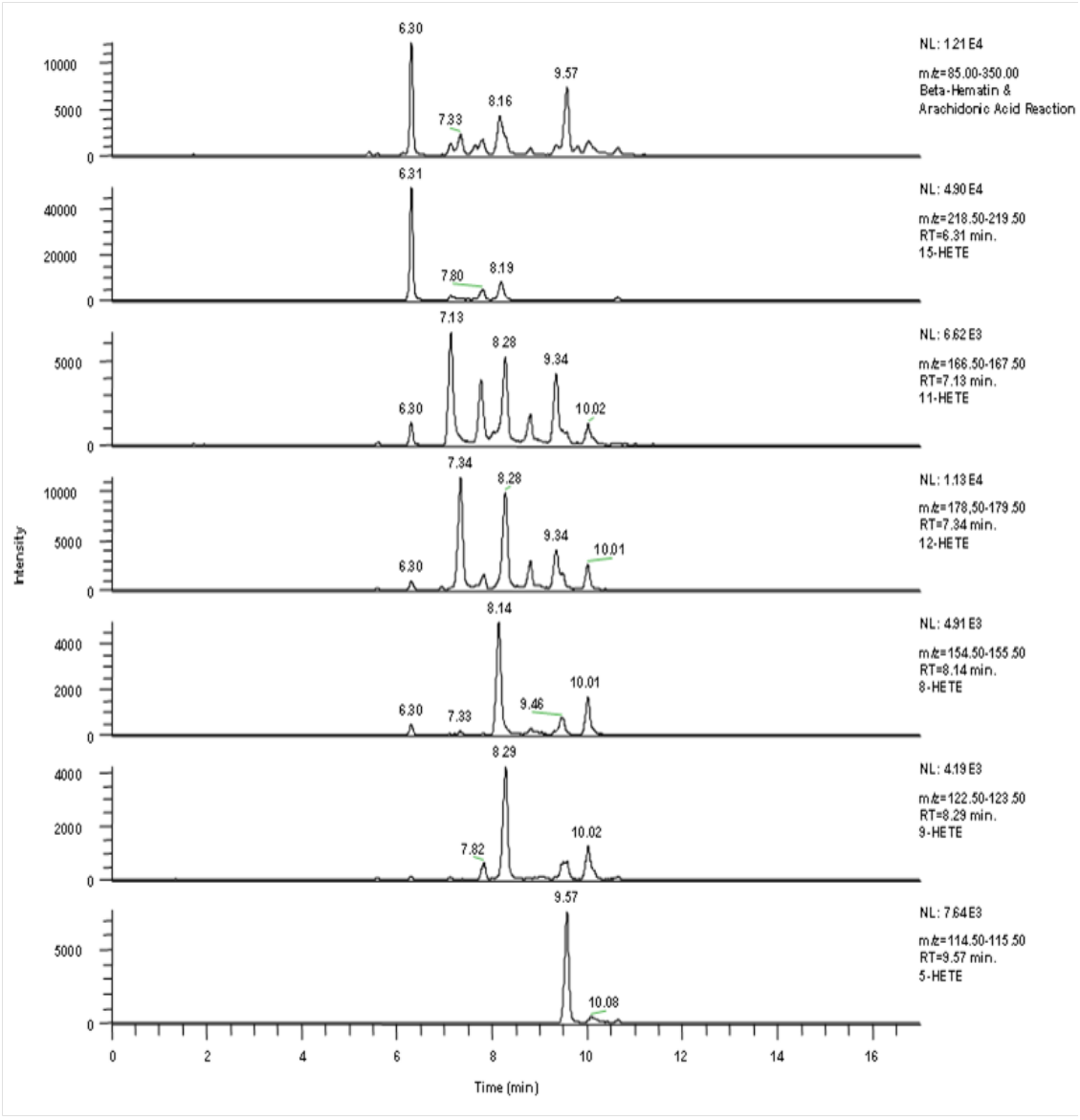

Figure 12. Extracted ion profile of HETEs from the BH-AA reaction. All six positional isomers of HETEs were extracted and confirmed by MS/MS from the BH-AA reaction. (Copyright, Elsevier 2007)

Upon subsequent chiral analysis, the positional HETE isomers were separated with a stereoselective ratio of nearly 1, suggesting no preferential stereochemical orientation of the substrate during oxidation. As expected, the stereoselective bias for 12-*S*-HETE seen in the native *Sm*HZ lipid coat was absent in the reaction of either purified *Sm*HZ or BH

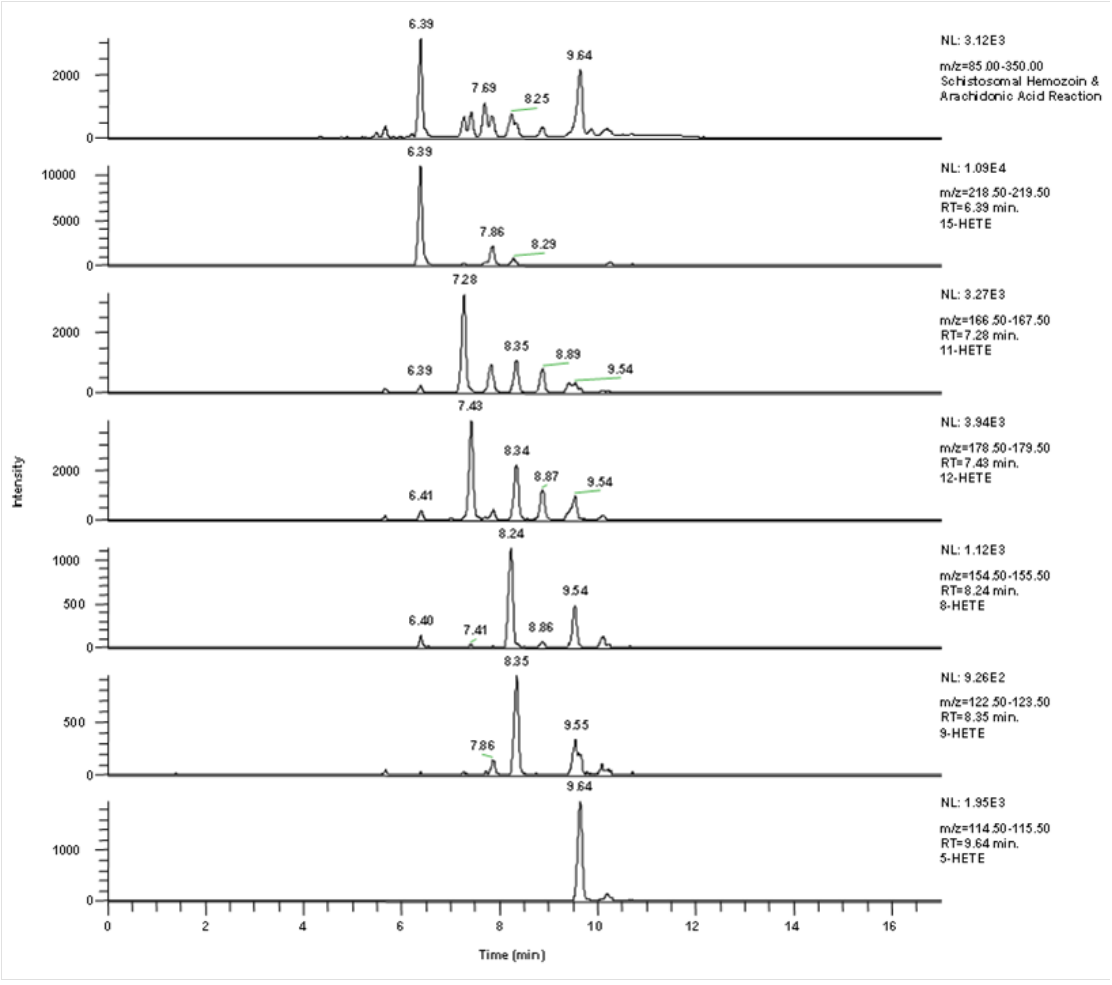

Figure 13. Extracted ion profile of HETEs from the *Sm*HZ-AA reaction. All six positional isomers of HETEs were extracted and confirmed by MS/MS from the *Sm*HZ-AA reaction. (Copyright, Elsevier 2007)

with AA. Taken together, these results demonstrate that *Sm*HZ mediated peroxidation of PUFAs is the likely source for the enantiomeric population of observed HETE isomers in the lipid coat.

Lipid metabolites have been shown to elicit immunomodulatory effects ranging from impairment of both PMA-stimulated oxidative burst and nitric oxide (NO) production in macrophages to altering endothelial cell permeability and initiating

chemotaxis.[16,39,40] Investigation of the HETE isomers' individual effects on macrophage-like cell function following LPS challenge revealed that the predominate 5-, 12- and 15-*S*-HETEs impaired NO production in a dose-dependent manner (**figure 14A**). 12-*S*-HETE was the most potent inhibitor of iNOS, attenuating NO production by 50%. The immunosuppressive activity of native *Sm*HZ's hydroxylated fatty acids suggest that phagocytosis of native *Sm*HZ by resident macrophages may partially disrupt the innate immune response. In fact, further study revealed a 25% reduction in NO production in lipid-coated *Sm*HZ-laden macrophages relative to control experiments, implicating native *Sm*HZ as a biologically active agent (**figure 14B**).

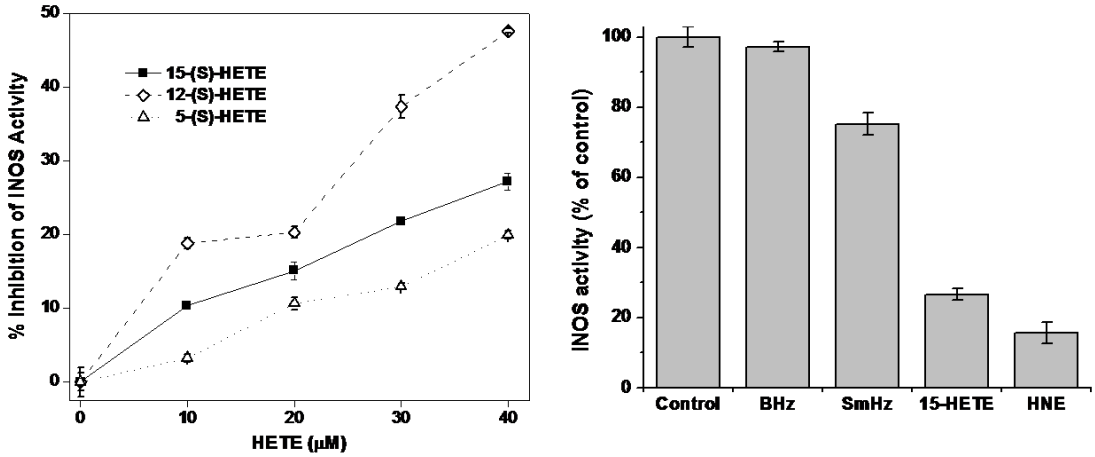

Figure 14. Impact of native *Sm*HZ and components on iNOS activity. (A) RNS production in macrophage cells monitored following treatment with increasing concentrations of (●) 15-, (■) 12- and (▲) 5-*S*-HETE by the Griess assay. (B) Cells were treated with 0.1 mg/mL BH or *Sm*HZ, as well as 40 μM 15-*S*-HETE or HNE. The activity of cells stimulated with LPS was used as a control. (Copyright, Elsevier 2007)

Conclusion

The lipid coat of native *Sm*HZ is a complex mixture of both neutral lipids and PUFA peroxidation products. Herein, the composition of the arachidonate metabolites has been determined to consist of an enantiomeric mixture of all positional hydroxylated isomers with 15-, 12- and 5-HETE as the dominant species. These findings are consistent with HZ-mediated non-enzymatic lipid peroxidation of host arachidonate. Additional chiral analysis revealed an accumulation of a biologically derived 12-*S*-HETE of an unknown origin. When the immunosuppressive activity of native *Sm*HZ and its major HETE components was examined in macrophage-like cells, iNOS activity was impaired. Further exploration of this unique biomineral's composition and its ability to modulate host immunity is crucial in developing a better understanding of the possible role of hemozoin in the host-pathogen interactions involving *S. mansoni*.

References

1. Carter, M. D.; Reese Harry, S.; Wright, D. W. *Biochem Biophys Res Commun* **2007**, *363*, 867-72.

2. Abbas, A. K.; Janeway, C. A., Jr. *Cell* **2000**, *100*, 129-38.

3. *(2002) in WHO Technical Report Series 912, Geneva*.

4. McManus, D. P. *Immunol. Rev.* **1999**, *171*, 149-161.

5. Pearce, E. J.; MacDonald, A. S. *Nat. Rev.* **2002**, *2*, 499-511.

6. van der Werf, M. J.; de Vlas, S. J.; Brooker, S.; Looman, C. W. N.; Nagelkerke, N. J. D.; Habbema, J. D. F.; Engels, D. *Acta Trop* **2003**, *86*, 125-139.

7. Francis, S. E.; Sullivan, D. J., Jr.; Goldberg, D. E. *Annu Rev Microbiol* **1997**, *51*, 97-123.

8. Brindley, P. J.; Kalinna, B. H.; Dalton, J. P.; Day, S. R.; Wong, J. Y.; Smythe, M. L.; McManus, D. P. *Mol Biochem Parasitol* **1997**, *89*, 1-9.

9. Lawrence, J. D. *J. Parasitol.* **1973**, *59*, 60-63.

10. Chou, A. C.; Fitch, C. D. *J Clin Invest* **1981**, *68*, 672-7.

11. Green, M. D.; Xiao, L.; Lal, A. A. *Mol Biochem Parasitol* **1996**, *83*, 183-8.

12. Oliveira, M. F.; d'Avila, J. C.; Torres, C. R.; Oliveira, P. L.; Tempone, A. J.; Rumjanek, F. D.; Braga, C. M.; Silva, J. R.; Dansa-Petretski, M.; Oliveira, M. A.; de Souza, W.; Ferreira, S. T. *Mol Biochem Parasitol* **2000**, *111*, 217-21.

13. Oliveira, M. F.; Kycia, S. W.; Gomez, A.; Kosar, A. J.; Bohle, D. S.; Hempelmann, E.; Menezes, D.; Vannier-Santos, M. A.; Oliveira, P. L.; Ferreira, S. T. *FEBS Lett* **2005**, *579*, 6010-6.

14. Pagola, S.; Stephens, P. W.; Bohle, D. S.; Kosar, A. D.; Madsen, S. K. *Nature* **2000**, *404*, 307-10.

15. Bohle, D. S.; Helms, J. B. *Biochem Biophys Res Commun* **1993**, *193*, 504-8.

16. Schwarzer, E.; Kuhn, H.; Valente, E.; Arese, P. *Blood* **2003**, *101*, 722-8.

17. Schwarzer, E.; Turrini, F.; Ulliers, D.; Giribaldi, G.; Ginsburg, H.; Arese, P. *J Exp Med* **1992**, *176*, 1033-41.

18. Urban, B. C.; Roberts, D. J. *Curr Opin Immunol* **2002**, *14*, 458-65.

19. Giribaldi, G.; Ulliers, D.; Schwarzer, E.; Roberts, I.; Piacibello, W.; Arese, P. *Haematologica* **2004**, *89*, 492-3.

20. Miller, C. M.; Carney, C. K.; Schrimpe, A. C.; Wright, D. W. *Inorg Chem* **2005**, *44*, 2134-6.

21. Schwarzer, E.; Muller, O.; Arese, P.; Siems, W. G.; Grune, T. *FEBS Lett* **1996**, *388*, 119-22.

22. Wynn, T. A.; Thompson, R. W.; Cheever, A. W.; Mentink-Kane, M. M. *Immunol Rev* **2004**, *201*, 156-67.

23. Costa-Silva, M.; Rodrigues-Silva, R.; Hulstijn, M.; Neves, R. H.; de Souza Panasco, M.; Lenzi, H. L.; Machado-Silva, J. R. *Mem Inst Oswaldo Cruz* **2002**, *97 Suppl 1*, 129-42.

24. Sullivan Jr., D. J.; Gluzman, I. Y.; Russell, D. G.; Goldberg, D. E. *Proc. Natl. Acad. Sci. USA* **1996**, *93*, 11865-11870.

25. Sullivan, D. J., Jr.; Gluzman, I. Y.; Russell, D. G.; Goldberg, D. E. *Proc. Natl. Acad. Sci.* **1996**, *93*, 1865-11870.

26. Soares, J. B. R. C.; Maya-Monteiro, C. M.; Bittencourt-Cunha, P. R. B.; Oliveira, P. L.; Egan, T. J.; Oliveira, M. F. *FEBS Lett.* **2007**, *581*, 1742-1750.

27. Pisciotta, J. M.; Coppens, I.; Tripathi, A. K.; Scholl, P. F.; Shuman, J.; Bajad, S.; Shulaev, V.; Sullivan, D. J., Jr. *Biochem J* **2007**, *402*, 197-204.

28. Boeglin, W. E.; Kim, R. B.; Brash, A. R. *Proc Natl Acad Sci U S A* **1998**, *95*, 6744-9.

29. Coffa, G.; Hill, E. M. *Lipids* **2000**, *35*, 1195-204.

30. Hada, T.; Swift, L. L.; Brash, A. R. *Biochim Biophys Acta* **1997**, *1346*, 109-19.

31. Hawkins, D. J.; Brash, A. R. *J Biol Chem* **1987**, *262*, 7629-34.

32. Jiang, Z. D.; Gerwick, W. H. *Lipids* **1997**, *32*, 231-5.

33. Jiang, Z. D.; Ketchum, S. O.; Gerwick, W. H. *Phytochemistry* **2000**, *53*, 129-33.

34. Samuelsson, B.; Dahlen, S. E.; Lindgren, J. A.; Rouzer, C. A.; Serhan, C. N. *Science* **1987**, *237*, 1171-6.

35. Yamamoto, S.; Suzuki, H.; Ueda, N. *Prog Lipid Res* **1997**, *36*, 23-41.

36. Burger, F.; Krieg, P.; Marks, F.; Furstenberger, G. *Biochem J* **2000**, *348 Pt 2*, 329-35.

37. *S. mansoni GeneDB v. 4.0, The Wellcome Trust Sanger Institute*.

38. Porter, N. A.; Wolf, R. A.; Yarbro, E. M.; Weenen, H. *Biochem Biophys Res Commun* **1979**, *89*, 1058-64.

39. Carney, C. K.; Schrimpe, A. C.; Halfpenny, K.; Harry, R. S.; Miller, C. M.; Broncel, M.; Sewell, S. L.; Schaff, J. E.; Deol, R.; Carter, M. D.; Wright, D. W. *J Biol Inorg Chem* **2006**, *11*, 917-29.

40. Schwarzer, E.; Ludwig, P.; Valente, E.; Arese, P. *Parassitologia* **1999**, *41*, 199-202.

CHAPTER III

METABOLIC IMPACT OF 4-HYDROXYNONENAL ON MACROPHAGE FUNCTION AND ACTIVATION

Introduction

4-hydroxynonenal (HNE) is an α,β-unsaturated aldehyde that is emerging as a biochemical marker of oxidative stress in many diseases such as Parkinson's disease, Alzheimer's disease, atherosclerosis, malaria and even obesity.[1-6] During cellular oxidative stress, HNE is formed by means of membrane lipid peroxidation which is initiated by the surrounding reactive oxygen species.[8] HNE is a highly reactive electrophile that covalently modifies DNA and protein resulting in genetic mutations, altered cellular function and ultimately cell death.[9]

HNE is formed as a secondary oxidation product of the peroxidation of cellular membrane-rich fatty acids including arachidonic and linoleic acids. The primary reactants for HNE include the amino acid residues of cysteine, histidine and lysine and typically occurs by the formation of Michael adducts and/or Schiff bases at available basic amino acid residues. HNE modification of cellular proteins and enzymes results in wide range of cellular dysfunction including protein and nucleic acid synthesis, mitochondrial and cellular respiration as well as specialized cell functions such as oxidative burst in neutrophils and macrophages.[10-12]

In the case of specialized cell function, professional phagocytes such as macrophages engulf microbial intruders and effectively kill and eradicate the foreign bodies. During this process, NADPH oxidase translocates to the phagolysosome to

provides the antimicrobial superoxide (O_2^-) substrate for a plethora of reactive oxygen and nitrogen species (ROS, RNS).[13] Macrophages are equipped with endogenous antioxidant mechanisms that prevent excessive lipid peroxidation buildup within the cell while exogenous HNE exposure has been shown to dramatically impair macrophage function including: inducible nitric oxide synthase (iNOS), phorbol ester stimulated oxidative burst, and phagocytosis.[11,14]

To investigate the metabolic impact of HNE exposure on macrophage function

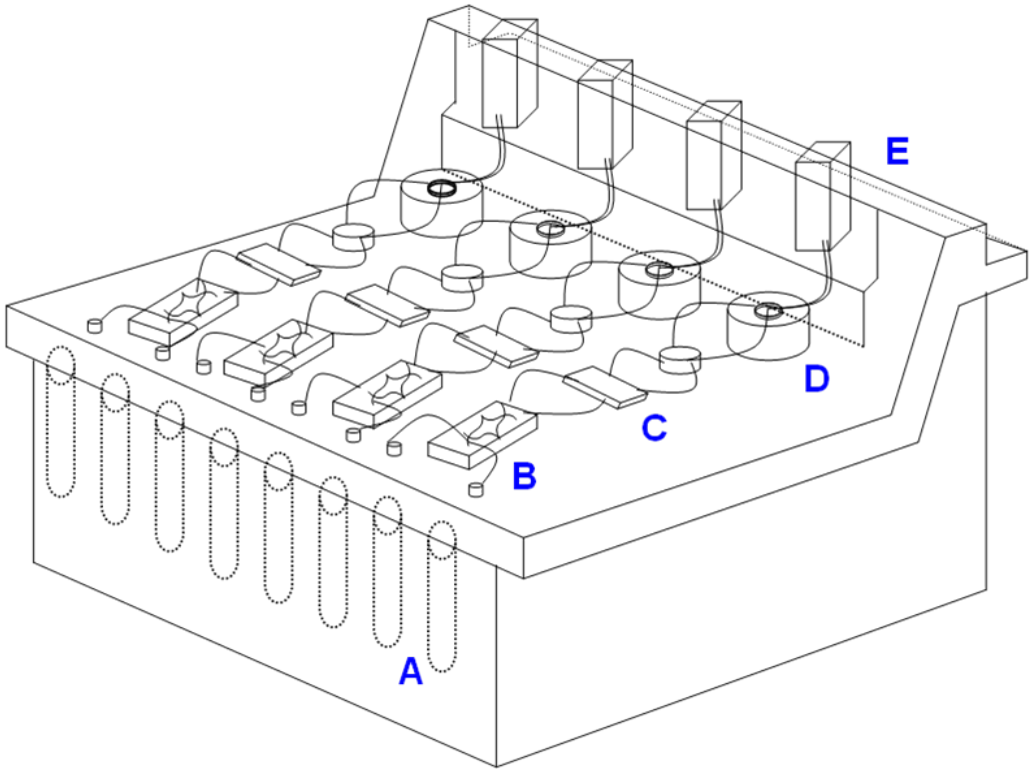

Figure 15 . Schematic of a Cytosensor Microphysiometer (A) Low-buffered running medium, (B) peristaltic pumps, (C) Teflon debubbler membrane, (D) LAPS sensor cup, cell culture immobilization membrane and custom MMP sensorhead/plunger, (E) online Ag/AgCl reference electrode.

and activation, we employed a multianalyte microphysiometer (MMP) that simultaneously measures multiple cellular metabolites in real-time.[15] The MMP is based on a core cell-based assay platform known as the Cytosensor microphysiometer.[7,15-17] The Cytosensor microphysiometer was designed to use a light-addressable potentiometric sensor (LAPS) to measure extracellular acidification rates (ECARs) in cultured cells due to the build-up of acidic by-products.[18-20] Recently, incorporation of oxygen, glucose and lactate electrodes into the sensor head platform have provided an effect means of concurrently measuring each extracellular analyte fluctuation using ion-selective and enzyme coated platinum electrodes via the amperometric detection of molecular oxygen and hydrogen peroxide, respectively.[15]

The Cytosensor microphysiometer operates by flowing a low-buffered medium in a series of cycles across cells seeded between two polycarbonate membranes (**figure 16**). The instrument consists of four channels, each with independent peristaltic pumps, a Teflon membrane debubbler, sensor chamber and reference electrode (**figure 15**). The flow cycles are composed of a pump on (flow) and pump off (stop-flow) phase. Experimental data points are collected in real-time and changes during a stop-flow phase measures the rate of consumption or production of each analyte based on the decrease/increase due to consumption or excretion of analyte. Data analysis is based on the changes in peak height or area under the peak which allows for monitoring metabolic changes over a finite period time.[16]

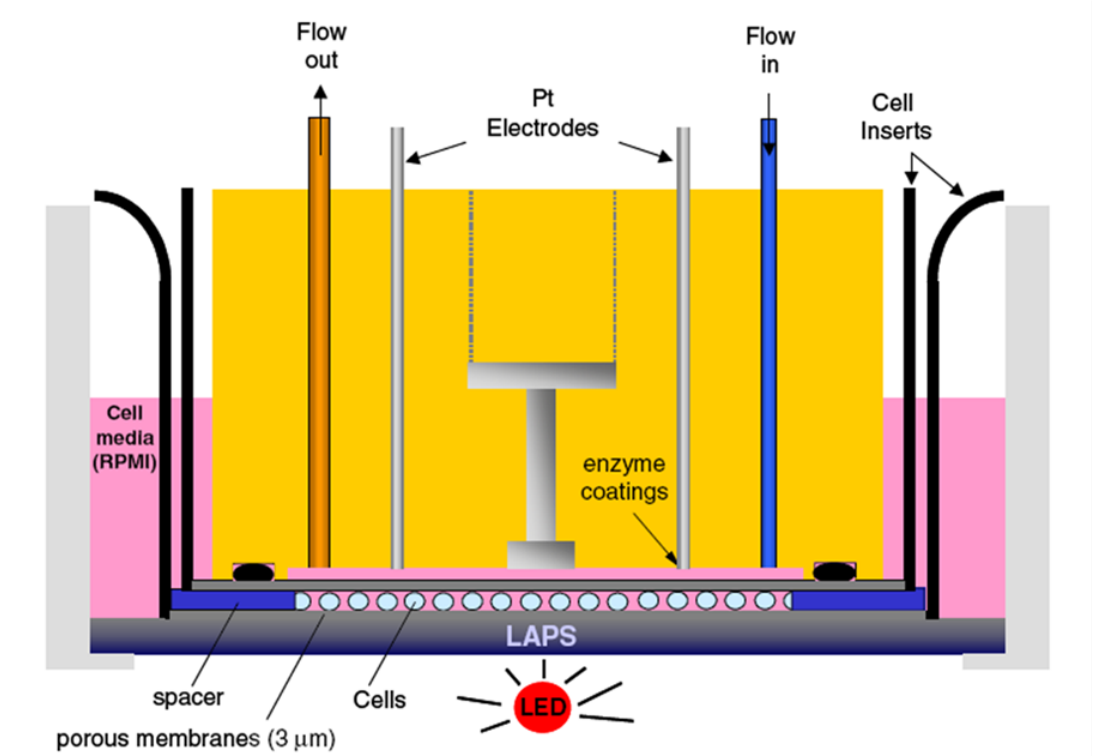

Figure 16. Schematic of the fully assemble MMP sensor head.[7] The LAPS sensor cup is fully submerged in low-buffered medium. with the cells immobilized between two polycarbonate porous membranes (3 µm). Running medium flows through the 3 µL measurement chamber . Analyte measurement and acidification measurements are performed in real-time.

This study is dedicated to understanding the metabolic changes imposed on macrophages upon exposure to HNE. Multianalyte microphysiometry was used to monitor real-time perturbations in acidification rate, lactate production and oxygen consumption. RAW 264.7 murine macrophages were exposed to increasing concentrations of HNE at various time intervals to assess both concentration and temporal dependence of HNE toxicity and immunosuppression. Following online HNE treatment, macrophage cells were activated with phorbol myristate acetate (PMA) to measure the corresponding change in metabolism upon initiation of oxidative burst. The

results of this study explicitly show that HNE is a potent modulator of cellular metabolism that readily inhibits PMA-induced oxidative burst in macrophages. The complex nature of HNE toxicity on macrophage function and resulting immunosuppression of oxidative burst suggests that covalent modification of downstream signaling proteins such as protein kinase C (PKC) are intimately involved with impairment of NADPH oxidase activity.

Experimental

Materials

Glucose oxidase (GOx, *aspergillus niger*), lactate oxidase (LOx, pediococcus), bovine serum albumin (BSA, Fraction V, 96%), glutaraldehyde (25 wt.% solution in water), and 3-aminophthalhydrazine (luminol) were purchased from Sigma Aldrich (St. Louis, MO). RPMI 1640 low-buffered medium and all Cytosensor consumable materials were obtained from Molecular Devices (Sunnyvale, CA). Nafion (perfluorosulfonic acid-PTFE copolymer, 5% w/w solution) and platinum wire (0.13 mm, 0.5 mm and 1.5 mm) was obtained from Alpha Aesar. 4-hydroxynonenal (HNE), phorbol-12-myristate-13-acetate (PMA) and the polyclonal anti-PKC (protein kinase C) antibodies were obtained from Calbiochem. Fetal bovine serum was purchased from Atlanta Biologicals. Penicillin/streptomycin was purchased from Mediatech. The mouse macrophage cell line, RAW 264.7 was obtained from the American Type Culture Collection.

Multianalyte Microphysiometer Enzyme-based Electrodes

Cytosensor microphysiometer plunger heads were purchased from Molecular Devices, Inc. and modified for multianalyte measurement by constructing multiple platinum electrodes at the face of the plunger head (see **figure 18**). Platinum wires were inserted into predrilled holes through the plunger head and sealed with a non-conductive white epoxy, polished with emery paper using a customized brass jig, and further polished with 1 μm diamond paste until flush with the plunger head surface. The enzyme

film solutions consisted of 5 mg GOx and 0.1 mg LOx dissolved in a 10% BSA/PBS solution and were cross-linked with either 5 μL or 1 μL of 25 % glutaraldehyde solution, respectively. Each enzyme film solution was prepared fresh and a minimal amount applied to the platinum electrode. Enzyme films were allowed to dry for 30 min and prior to use, GOx and oxygen electrodes were coated with a minimal amount of 5% Nafion (w/w).

Glucose measurements were obtained during each experiment but were excluded from the results analysis due to the lack of appreciable signal change throughout the study. Lactate measurements were performed indirectly by amperometrically measuring changes in hydrogen peroxide (+0.6 V) generated at the lactate oxidase (LOx) membrane on platinum electrode. Changes in oxygen consumption were measured amperometrically (-0.45 V) and all electrode potentials were set versus a Ag/AgCl reference electrode. Acidification rates were measured by traditional operation of the Cytosensor instrument as specified by the manufacturer.

MMP Instrument Operation

The MMP was operated under standard Cytosensor microphysiometer conditions utilizing an 60-s flow cycle and a 60-s stop-flow cycle. Prior to insertion of the modified plunger head, the MMP was conditioned by flowing low-buffered RPMI 1640 media through the system for 30 min. Sensor chambers and Teflon debubblers were preheated for 30 min in order to ensure an optimum temperature (37^{o}C) for data collection. After complete conditioning, the modified sensor head was placed in the sensor chamber and cells (5 x 10^5 RAW 264.7 cells/capsule cup) were allowed to equilibrate for 20 min.

MMP Metabolic Data Collection and Interpretation

Electrochemical measurements were allowed to run for 50 minutes prior to the addition of HNE (0-300 μM) and/or PMA (16 μM) in the running medium. For each experiment, metabolic measurement of four individual and independent RAW 264.7 cell populations were collected with the following treatment conditions each lane: (1) untreated control population; (2) 20 minute HNE exposure (1 mL); (3) 40 minute HNE exposure (2 mL); and (4) 60 minute HNE exposure (3 mL). Oxidative burst measurements following HNE treatment were collected after a 30 minutes equilibration period of fresh medium. Oxidative burst was initiatiated by introducing 16 μM PMA for 10 minutes (0.5 mL). Data points were collected in real-time and extracted from stop-flow measurements at 2 minute intervals (2 min = 1 cycle).

The extracellular acidification rate (ECAR) data was recorded in normal operating order by the Cytosensor microphysiometer. Electrochemical measurements for lactate and oxygen were collected on either a CHI 103 multipotentiostat (CH Instruments, Austin, TX) or an in-house custom quad-multiplexed multipotentiostat. ECAR data was plotted as -μV/s versus time (s). The changes in oxygen consumption and lactate production were quantified by calculating the change in signal (nA) during stop-flow events. Each cycle measurement was plotted as singal increase/decrease (nA) versus time (2 min). Baseline correction for all measurements was performed by linear-fit correction from the linear extension of the initial equilibration period. The linearized metabolic curves were normalized to 1 with experimental changes represented by percent

of control. Overall relative changes in metabolism were presented as the average percentage value of 10 cycles upon introduction of fresh medium.

Cell Culture

The adherent mouse macrophage cell line, RAW 264.7, was maintained in continuous culture with RPMI 1640 medium, supplemented with 10% (v/v) fetal bovine serum and 100 U/mL penicillin/streptomycin in a 5% CO_2, 37^{o}C atmosphere.

Inhibition of RAW 264.7 ROS Production with HNE

RAW 264.7 cells were plated overnight in 6 well plates at a density of 4E6 cells per well. The cells were washed once with sterile PBS followed by incubation with HNE (0-50 μM) for 3 hours. After HNE treatment, the cells were washed once with cold PBS and treated with 100 nM PMA in PBS for 5 minutes to initiate oxidative burst. After 5 minutes, the supernatant was removed and transferred to luminometer cuvettes. Upon addition of 50 μL of 1.0 mM luminol, luminescence was measured for ten seconds using a Moonlight 3010 luminometer.

Cell Treatment with HNE for Western Blot Analysis

RAW 264.7 mouse macrophage cells were plated overnight at a density of 4E6 cells per 100 mm dish. The following day, the cells were treated with 10 mL of 35 μM HNE prepared in media and incubated at 37^{o}C, 95% humidity and 5% CO_2. Once the allotted time (0, 0.5, 1.0, 1.5, 2.0, 2.5 and 3.0 hours) had passed, the samples were removed from the incubator, washed 3 times with cold PBS and treated with 400 μL of

cold lysis buffer (25 mM Tris-HCl, pH 7.4, 0.25 mM sucrose, 2.5 mM EDTA, 2.5 mM DTT). After five minutes of rapid agitation, the samples were scrapped, pipetted to microcentrofuge tubes, and gently sonicated with a probe sonicator. Next, the samples were centrifuged for 45 minutes at 13,200 RPM. The supernatant was collected and protein content was analyzed using the Biorad DC assay kit.

Western Blot Analysis of Cell Lysates

All samples examined by gel electrophoresis/western blotting, were prepared at a 2 μg/μL concentration and run on Novex 10 % Tris-glycine gels (Invitrogen) followed by transfer to polyvinylidene difluoride (PVDF) membranes (Invitrogen). After complete transfer, the membranes were blocked for 1 hour or overnight with 5 % nonfat dry milk dissolved in Tris-Tween buffer (TBST) composed of 25 mM Tris-HCl, pH 7.4, with 137 mM NaCl, 2.7 mM KCl, and 0.01 % Tween 20, TBST. PKC obtained from the cells was detected by incubation with rabbit polyclonal anti-protein kinase C (α/β) (371-388) antibodies (diluted 1:230 in 5% nonfat dry milk) for 2 hours at room temperature. Standard PKC βII was detected by incubation with rabbit polyclonal anti-PKC βII primary antibody (diluted 1:100 in 5 % nonfat dry milk) for 2 hours at room temperature. For both, incubation with the primary was followed by TBST washing and incubation with a horseradish peroxidase-conjugated goat anti-rabbit secondary antibody (diluted 1:2000 in 5 % nonfat dry milk) for 1 hour at room temperature. HNE adducted proteins were detected by incubation with mouse monoclonal anti-HNE primary antibody (diluted 1:500 in 5 % nonfat dry milk) for 2 hours at room temperature, followed by incubation with a horseradish peroxidase-conjugated goat anti-mouse secondary antibody (diluted

1:2000 in 5 % nonfat dry milk) for 1 hour at room temperature. An ECL Western blotting analysis detection system (Amersham Biosciencees) was used to visualize the bands in all cases.

Results and Discussion

A Simple Model of Cellular Metabolism

In general, cellular metabolism is a complex network of small molecule fluxes that varies among organisms, cell type and in some cases, individual cells of the same phenotype. Glycolysis accounts for the majority of metabolic output within a cell due to the requisite need of energy in the form of ATP. Glycolysis occurs by means of two major pathways: (1) anaerobic conversion of glucose into lactic acid and (2) aerobic glucose metabolism via the Krebs' tricarboxylic acid (TCA) cycle (**figure 17**).[21,22] The TCA cycle is the dominant mode of ATP production within a normal resting cell. The

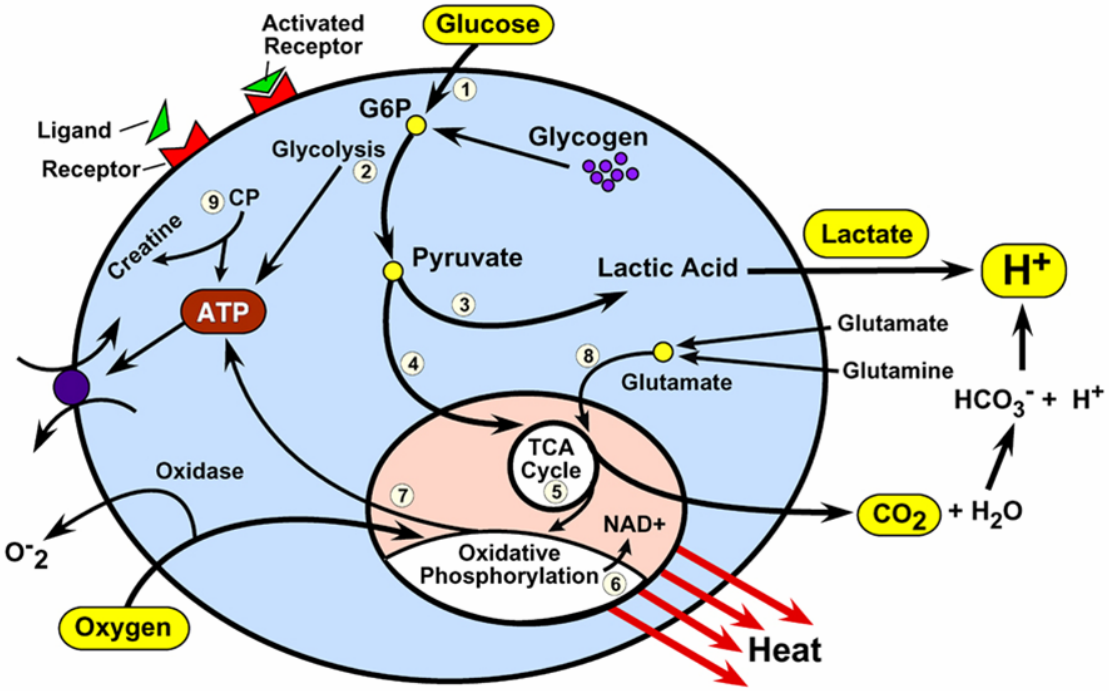

Figure 17. Cellular Energy Metabolism (Copyright, MDPI 2009)[7]

TCA cycle ultimately oxidizes glucose to carbon dioxide and water. In the case of anaerobic glucose metabolism, glycolysis proceeds to form pyruvate followed by an oxygen-independent conversion to lactic acid by means of LDH. Measurement of cellular oxygen consumption (aerobic) and lactate production (anaerobic) in concert allows for metabolic changes to be accurately assessed for each independent energy pathway. By integrating both an oxygen sensor and a lactate sensor with the acidification LAPS sensor, a more complex metabolic profile of energy metabolism can be achieved.

MMP Sensor Head Design and Operation

To achieve simultaneous measurements for key metabolites for each glycolytic

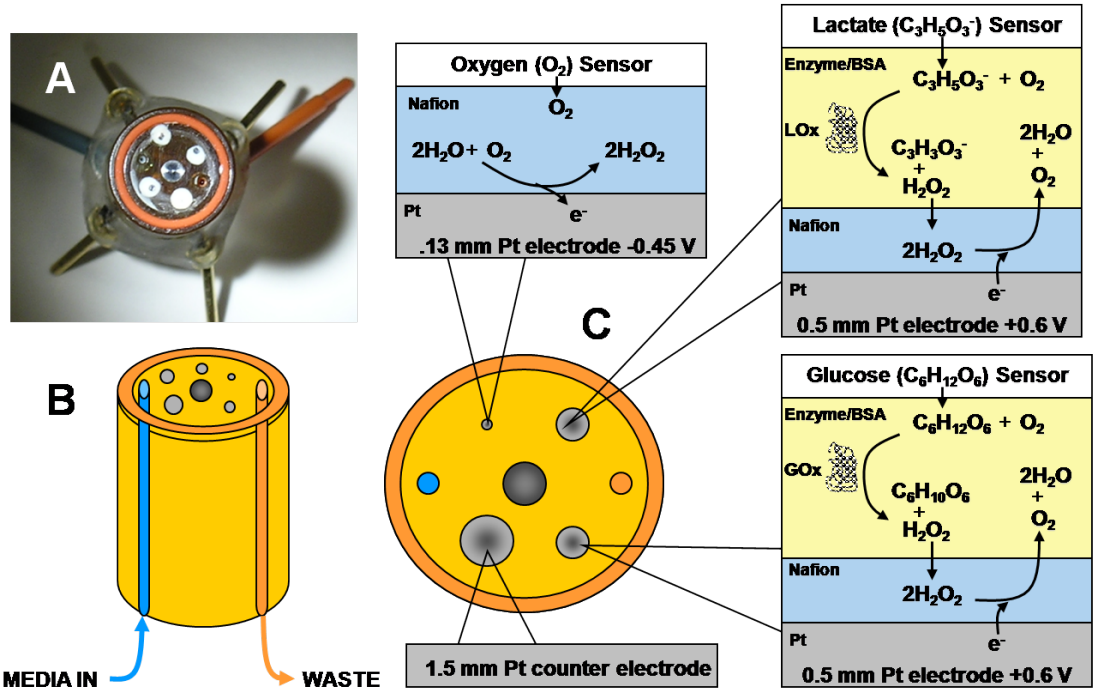

Figure 18. Modified MMP sensor head. (A) Fully constructed MMP sensor head with embedded platinum wire electrodes. (B) Schematic of the MMP sensor head media pathway. (C) Schematic representation of direct and enzymatic electrochemical detection of glycolysis metabolites.

pathway, enzyme-immobilized membranes were utilized for the indirect measurement of glucose and lactate concentrations within the cell chamber (**figure 18**). Both GOx and LOx convert their respective substrate to hydrogen peroxide which is then detected amperometrically by applying a +0.6V potential to oxidize two hydrogen peroxide molecules to water and oxygen. The oxygen electrode directly (-0.45V) reduces molecular oxygen but with the aid of a negatively charged Nafion membrane to eliminate background noise.

Metabolic Impact of HNE on Steady State Macrophage Metabolism

The complex biochemical interactions that occur between cellular macromolecules and HNE results in a variety of cellular perturbations including disruption of cytoskeletal integrity, impairment of mitochondrial respiration, inhibition of DNA, RNA and protein synthesis as well as impairment of specialized cellular functions such as oxidative burst in professional phagocytes.[11,14,23] During periods of oxidative stress, the surrounding cellular environment is exposed to errant reactive oxygen species that can potentially interact with membrane-derived unsaturated fatty acids resulting in the accumulation of HNE at significant concentrations. To date, malaria-derived hemozoin-laden monocytes were measured to have the highest intracellular HNE concentration at 23 pmols/10^6 cells (~46 μM).[10]

Real-time monitoring of lactate, oxygen and acidification rate changes for live cells is an attractive tool for assessing perturbations to cellular energy metabolism as a result of outside stimuli. To explore the metabolic impact HNE imposes on energy metabolism, RAW 264.7 murine macrophages were subjected to HNE treatment in a concentration and time dependent experimental design. In each experiment, RAW

264.7 cells were seeded at a density of 3E5 cells per polycarbonate cell capsule 4 hours prior to assembly of the full MMP instrumental setup. The following time course was performed for each experiment: (A) 60 minute equilibration period; (B) 0, 20, 40 or 60 minute HNE exposure (0, 50, 100, 200 or 300 µM); (C) 30 minute stabilization period.

Changes in cellular steady state metabolism were determined by taking the average of the last five measurements during the stabilization period (**figure 19**). The

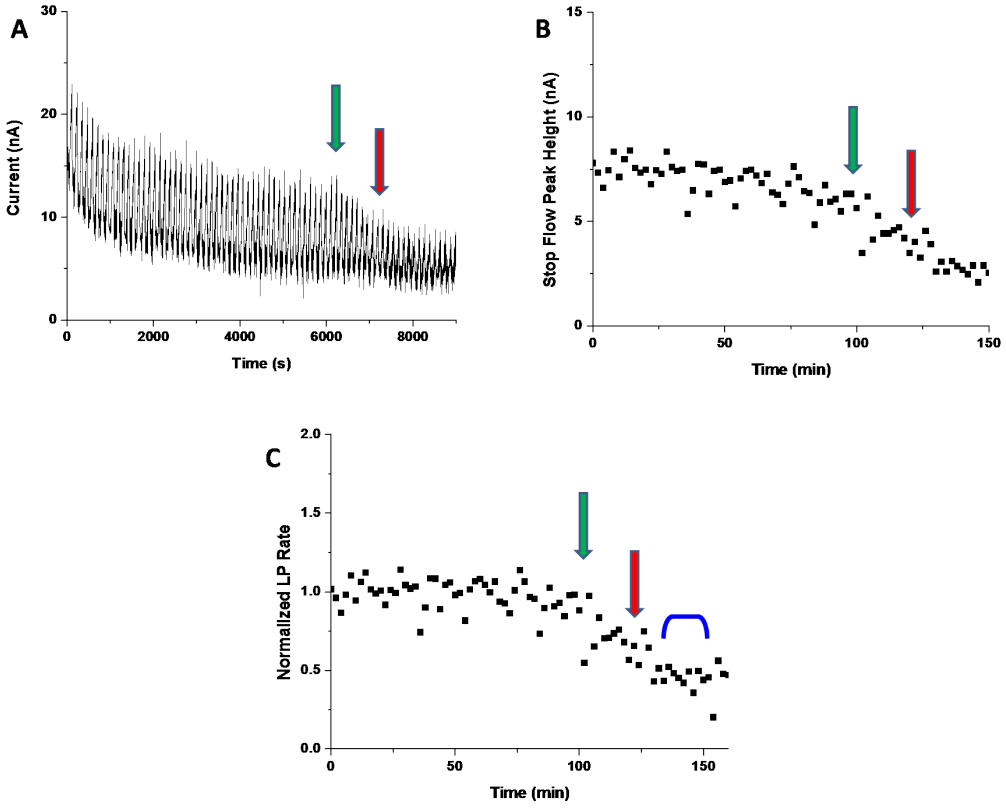

Figure 19. Conversion of Raw MMP Measurements to Metabolic Rate Values. (A) Raw LP data for 20 min exposure to 300 µM HNE. (B) Scatter plot of stop-flow peak height measurements. (C) Linear normalized rate plot. *(Green arrows): start of HNE treatment; (Red arrows): start of fresh media; (Blue): Average LP Rate Value (n=5).

change in metabolic output for each sensor was measured in real-time and is represented

as acidification rate (AR), lactate production rate (LPR) and oxygen consumption rate (OCR).

Table 1. HNE-induced Metabolic Rate Changes in Steady State Macrophage Metabolism

Acidification Rate (AR)

	HNE Concentration			
Exposure Time	50 μM	100 μM	200 μM	300 μM
Control	103.90 ± 0.73%	103.15 ± 5.72%	101.46 ± 3.66%	102.98 ± 2.01%
20 min	83.80 ± 1.14%	72.43 ± 8.16%	58.65 ± 5.46%	47.19 ± 6.12%
40 min	65.21 ± 1.01%	59.57 ±2.68%	50.22 ± 3.65%	32.53 ± 3.74%
60 min	53.67 ± 0.47%	49.43 ± 4.40%	41.91 ± 0.79%	21.54 ± 3.08%

Lactate Production (LP) Rate

	HNE Concentration			
Exposure Time	50 μM	100 μM	200 μM	300 μM
Control	99.63 ± 0.22%	101.83 ± 0.53%	100.96 ± 4.18%	101.74 ± 7.54%
20 min	81.56 ± 0.63%	68.87 ± 2.94%	55.11 ± 5.19%	45.76 ± 10.12%
40 min	58.21 ± 0.54%	64.90 ±2.07%	48.28 ± 6.93%	17.92 ± 10.05%
60 min	42.48 ± 0.75%	45.77 ± 2.21%	25.99 ± 9.13%	10.75 ± 6.31%

Oxygen Consumption (OC) Rate

	HNE Concentration			
Exposure Time	50 μM	100 μM	200 μM	300 μM
Control	99.78 ± 0.80%	100.25 ± 0.29%	103.26 ± 4.62%	100.01 ± 1.17%
20 min	80.93 ± 0.19%	87.71 ± 0.92%	90.77 ± 1.38%	72.72 ± 3.64%
40 min	83.18 ± 0.23%	93.59 ±0.31%	89.61 ± 0.96%	60.25 ± 7.80%
60 min	59.42 ± 2.39%	90.00 ± 0.46%	86.24 ± 1.37%	12.68 ± 5.98%

The experimental results displayed in **table 1** and **figures 20** and **21** clearly show that macrophage metabolism is disrupted by HNE exposure in both a concentration and time-dependent manner. The effect of HNE on acidification rates was a linear dose-

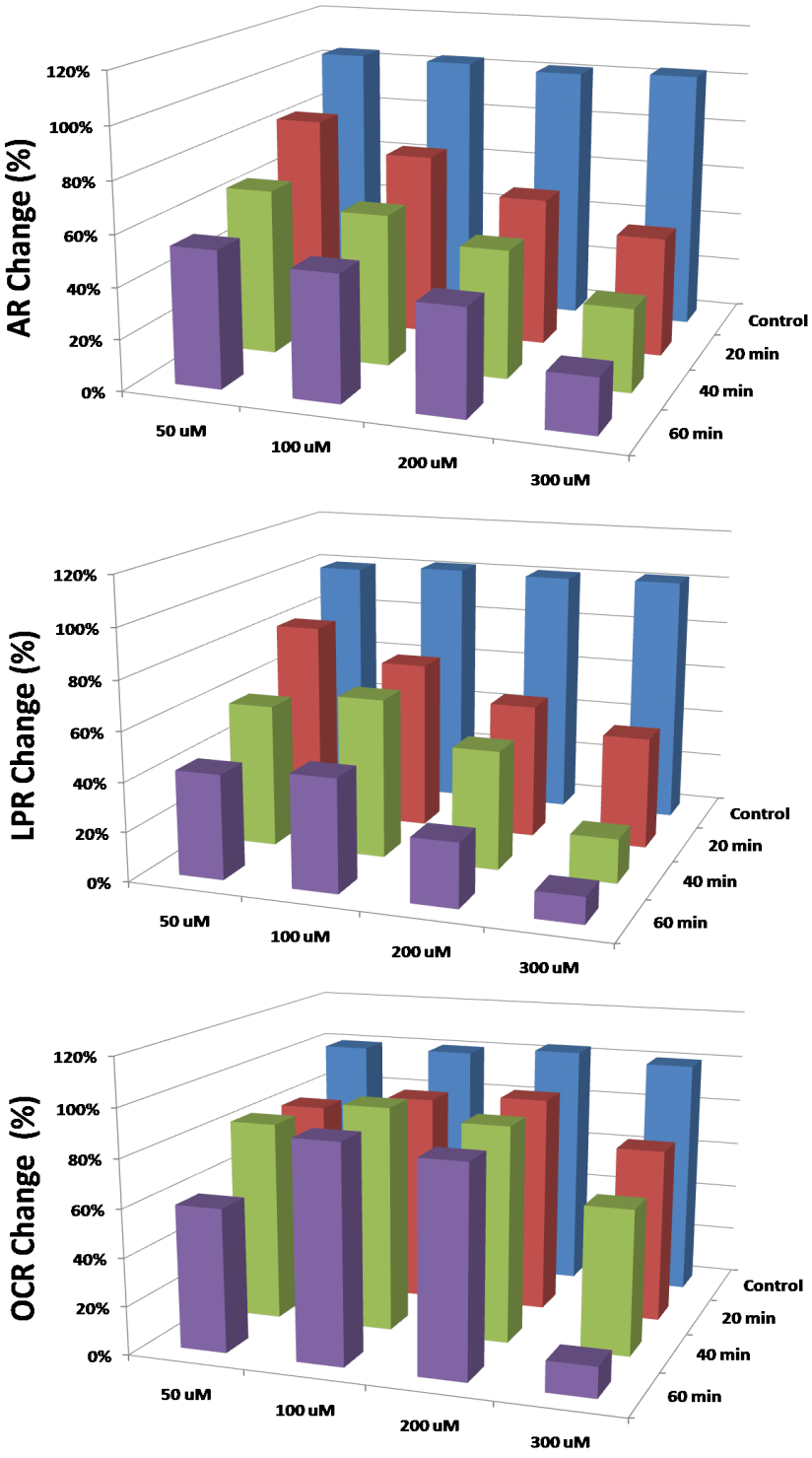

Figure 20. 3D Composite of HNE-treated Steady State Macrophage Metabolism. (top) AR rate changes, (middle) LP rate changes, and (bottom) OC rate changes. Rate changes are representative of final metabolic rate post-HNE exposure.

dependent reduction in extracellular acidification with all HNE treatment eliciting a reduction in AR. At the highest concentration (300 µM) and longest exposure (60 min), the steady state macrophage acidification rate dropped to 21.54 % of baseline.

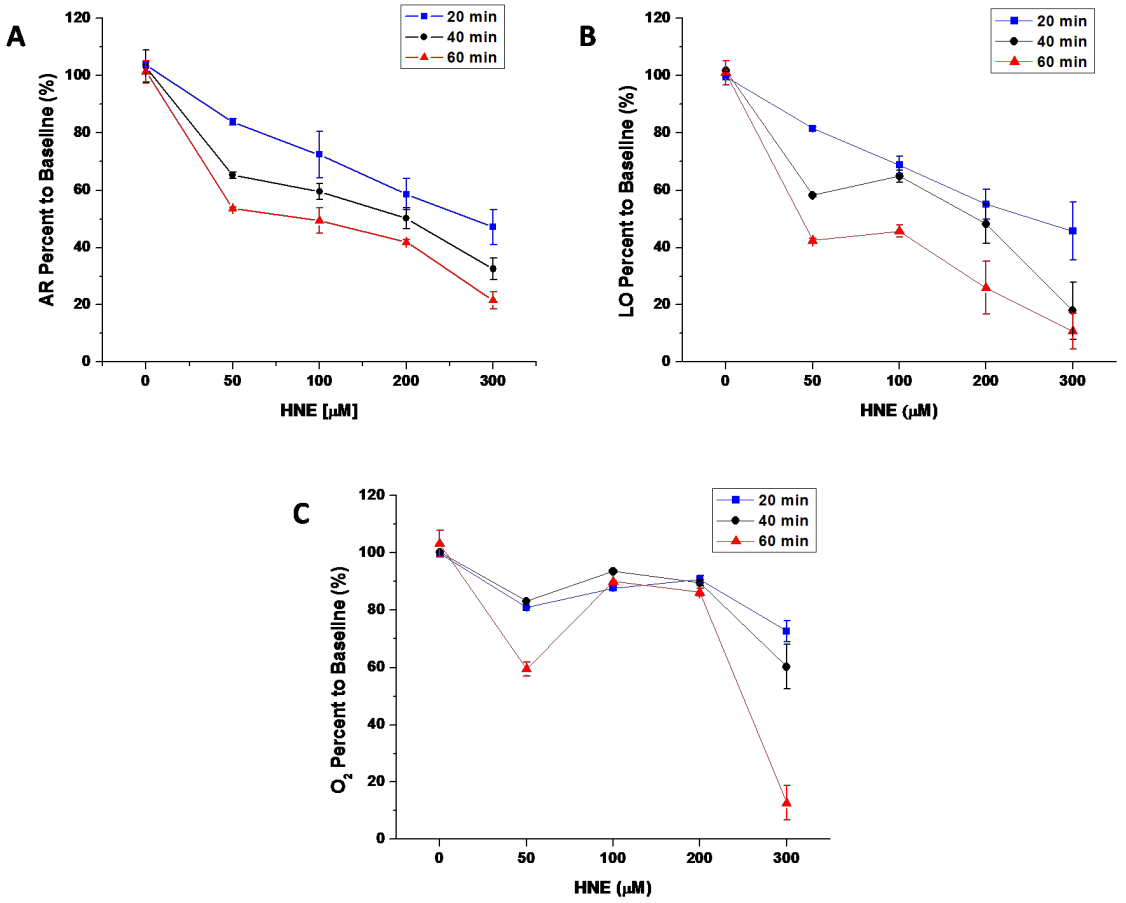

Figure 21. HNE Effects on Macrophage Metabolism as a Function of Concentration. (A) AR rate chages, (B) LP rate changes, and (C) OC rate changes.

In terms of anaerobic metabolism, lactate production rates experienced a similar dose-dependent response in terms of both concentration as well as exposure. As with AR metabolism, lactate production rates followed a concentration-dependent recession with a reduction in LO rate to 10.75% of baseline after 60 minutes of exposure to 300 µM. The

LO rate profile suggests that lactate response is slightly more sensitive to HNE in a concentration-dependent manner.

On the contrary, OC rates proved to be much more resilient to HNE toxicity as a whole. At HNE concentrations of 0-200 μM, oxygen consumption remained stable at >80% OC rates with very little discrimination between exposure times. At the highest concentration (300 μM), a dramatic drop in oxygen consumption was observed for each treatment in a time-dependent manner. Macrophage oxygen consumption was essentially attenuated (12.7%) after 60 minutes of exposure to 300 μM HNE and is indicative of cell death. This same conclusion can be made for both LOR (10.7%) and AR (21.5%) at high concentration and exposure. Cell death was confirmed by carefully removing the polycarbonate membrane and visual inspection with trypan-blue using a standard microscope.

Overall, the metabolic rate data suggests that RAW 264.7 macrophages are susceptible to HNE toxicity as concentrations as low as 50 μM with an exposure time of 20 minutes. The MMP data is collected in a series of stop-and-go flow cycles at intervals of 60 s flow/60 s stop-flow. With a flow rate of 100 μL/minute, a total volume of 1 mL can be assigned to each 20 minute intervals of exposure. This would represent a total molar HNE flux of 50-900 nmols for the lowest and highest concentration and exposure time, respectively. Each cell capsule is seeded with 3E5 cells and the fully assembled MMP sensor chamber amasses 30% of the culture area. This equates to a toxicity profile that spans 50-900 nmols per 10^4 cells.

Metabolic Rate Profile PMA-induced Oxidative Burst in RAW 264.7 Macrophages

To examine the energy metabolism of oxidative burst during macrophage activation, RAW 264.7 cells were treated for 10 minutes (5 cycles) with 16 µM phorbol-12-myristate-13-acetate (PMA) and metabolic changes were monitored thereafter for 30 minutes (**figure 22A**). PMA is a small organic molecule that mimics intracellular diacylglycerol and acts through activation of protein kinase C (PKC).[24] PKC is an enzyme that is a key intermediate for many cellular signaling processes.[25,26] PKC functions by means of intracellular phosphorylation of serine and threonine resides.[26]

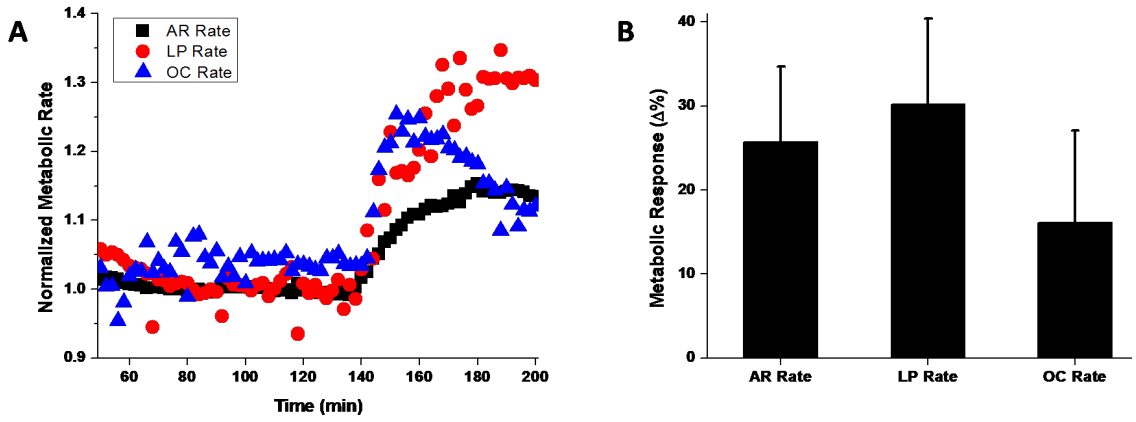

Figure 22. PMA-stimulated Macrophage Metabolic Response. (A) Normalized metabolic rate curves showing PMA introduction at t = 140 min. (B) Average metabolic response of each cellular metabolic rate. Determined from three independent experiments (n = 4).

PMA initiation of oxidative burst begins with phosphorylation of cytosolic p47phox followed by membrane assembly of multicomponent NADPH oxidase.[25]

Immediately following PMA exposure, a dynamic change for each metabolic rate with lactate production exhibiting the most dynamic change (+30.2%) followed by AR

rate (25.8%) and OC rate (+16.1%) (**figure 22B**). An overall increase in metabolic activity is to be expected due to the energy dependent assembly and activation of NADPH oxidase. PMA activation of RAW 264.7 cells displayed a gradual but pronounced increase in AR rate immediately upon exposure. When PMA was removed from the medium, AR rate was sustained at an elevated rate constant for >2hr. Unlike the gradual increase observed for AR rate, the LP rate displayed a more pronounced temporal increase reaching a maximum LP rate after 50 miniutes post PMA treatment. The increased LP rate is directly related to an increase in anaerobic respiration. In the case of oxygen consumption, an increase in OC rate would be expected due to NADPH oxidase conversion of extracellular molecular oxygen to superoxide. PMA-induced oxidative burst of RAW 264.7 cells displayed a sharp increase in oxygen consumption initially (t=0-10 min) that peaked after PMA was removed from the running media. A gradual decrease in OC rate was observed for the remainder of the experiment but remained elevated above baseline after 2 hours.

Collectively, these results paint a detailed metabolic picture of macrophage cellular respiration upon activation of NADPH oxidase by PMA. Immediately following PMA introduction, macrophage AR, LP and OC rates rapidly increases due to increased demand for requisite cellular energy (ATP) and molecular oxygen. Following removal of PMA from the running media, a pronounced initial decline in oxygen consumption was observed most likely due to the absence of NADPH oxidase activation which was followed by down regulation of the enzyme. In regards to energy metabolism, removal of PMA from the medium stabilizes elevated AR and LP rates but without an appreciable

decline (>2hr). The "primed" macrophage appears to retain an elevated state of cellular respiration and energy metabolism before returning to a normal state metabolism.

Metabolic Impact of HNE exposure on PMA-induced RAW 264.7 Oxidative Burst

HNE has been shown to impair and modulate key innate immune function in professional phagocytic cells, including oxidative burst and inducible nitric oxide synthase (iNOS).[11,12,27,28] Consequently, the exact mode by which HNE inhibition of oxidative burst occurs lies within the complex protein network involved in NADPH oxidase assembly and activation. To investigate HNE inhibition of PMA-induced

Table 2. HNE Effect on Metabolic Rate Changes in PMA-induced Oxidative Burst

Acidification Rate Change

	HNE Concentration			
Exposure Time	50 µM	100 µM	200 µM	300 µM
Control	18.73 ± 1.97%	17.74 ± 6.98%	30.54 ± 7.20%	36.00 ± 3.07%
20 min	10.78 ± 2.00%	40.87 ± 11.30%	27.59 ± 6.76%	0.67 ± 8.95%
40 min	9.69 ± 2.13%	45.03 ± 6.98%	8.04 ± 5.14%	-21.40 ± 4.35%
60 min	8.33 ± 2.00%	32.29 ± 6.18%	16.07 ± 3.12%	-23.46 ± 4.17%

Lactate Production Rate Change

	HNE Concentration			
Exposure Time	50 µM	100 µM	200 µM	300 µM
Control	16.36 ± 5.89%	39.15 ± 1.77%	29.22 ± 4.85%	36.21 ± 8.74%
20 min	25.84 ± 1.25%	21.31 ± 7.92%	7.00 ± 7.06%	-10.89 ± 14.61%
40 min	48.00 ± 3.07%	38.77 ± 3.29%	-10.71 ± 9.74%	-47.84 ± 11.18%
60 min	38.94 ± 2.00%	-25.54 ± 2.48%	-38.30 ± 3.55%	-48.45 ± 8.01%

Oxygen Consumption

	HNE Concentration			
Exposure Time	50 µM	100 µM	200 µM	300 µM
Control	30.93 ± 2.67%	5.67 ± 0.52%	17.31 ± 5.75%	10.63 ± 1.93%
20 min	1.91 ± 0.28%	-5.29 ± 2.18%	4.91 ± 2.48%	4.70 ± 4.28%
40 min	-12.33 ± 0.61%	-2.67 ± 0.53%	1.26 ± 1.77%	-21.49 ± 9.48%
60 min	-15.81 ± 2.90%	-2.28 ± 0.64%	0.39 ± 1.96%	-61.65 ± 8.74%

oxidative burst in macrophages, RAW 264.7 cells were treated with HNE (0-300 μM) at variable exposure times (0-60 min) followed by PMA activation. Each experiment was performed using the following experimental design: (1) 60 min equilibration period (Media); (2) 0-60 min HNE exposure (0-300 μM HNE in media); (3) 30 minute equilibration period; (4) 10 min 16 μM PMA exposure; (5) 50 min equilibration period. Metabolic rate changes were determined immediately following PMA exposure an average of five sequential data points, and are presented as percent to corrected baseline.

While MMP measurements do not directly measure NADPH oxidase generation of superoxide, the metabolic changes that are elicited by PMA activation provide a unique metabolic fingerprint for comparison against HNE-treated samples. As illustrated in **table 2** and **figures 23** and **24**, pretreatment of RAW 264.7 cells with HNE suppresses PMA-induced metabolic changes to some degree and induces a negative response for each metabolite at high concentration and exposure time.

The metabolic treads for PMA activation as a function of concentration are not nearly as straight-forward in comparison to the metabolic trends of the HNE toxicity analysis above. Looking first at metabolic rates at low HNE concentrations (50 and 100 μM), metabolic measurements revealed only minor changes in metabolic response with respect to HNE exposure time. For cells exposed to 100 μM HNE, PMA stimulation immediately increased AR at a 2-fold higher AR rate as compared to control. At higher HNE concentrations (200 and 300 μM), AR rates start to drop off and terminate with negative AR rate changes. For LP rate changes, a steep regression into negative LP rates begins at the 100 μM-60min data point and terminates at 300μM-60min with a 50% reduction in lactate signal. At these concentrations, PMA treatment at 16 μM for 5 cycles

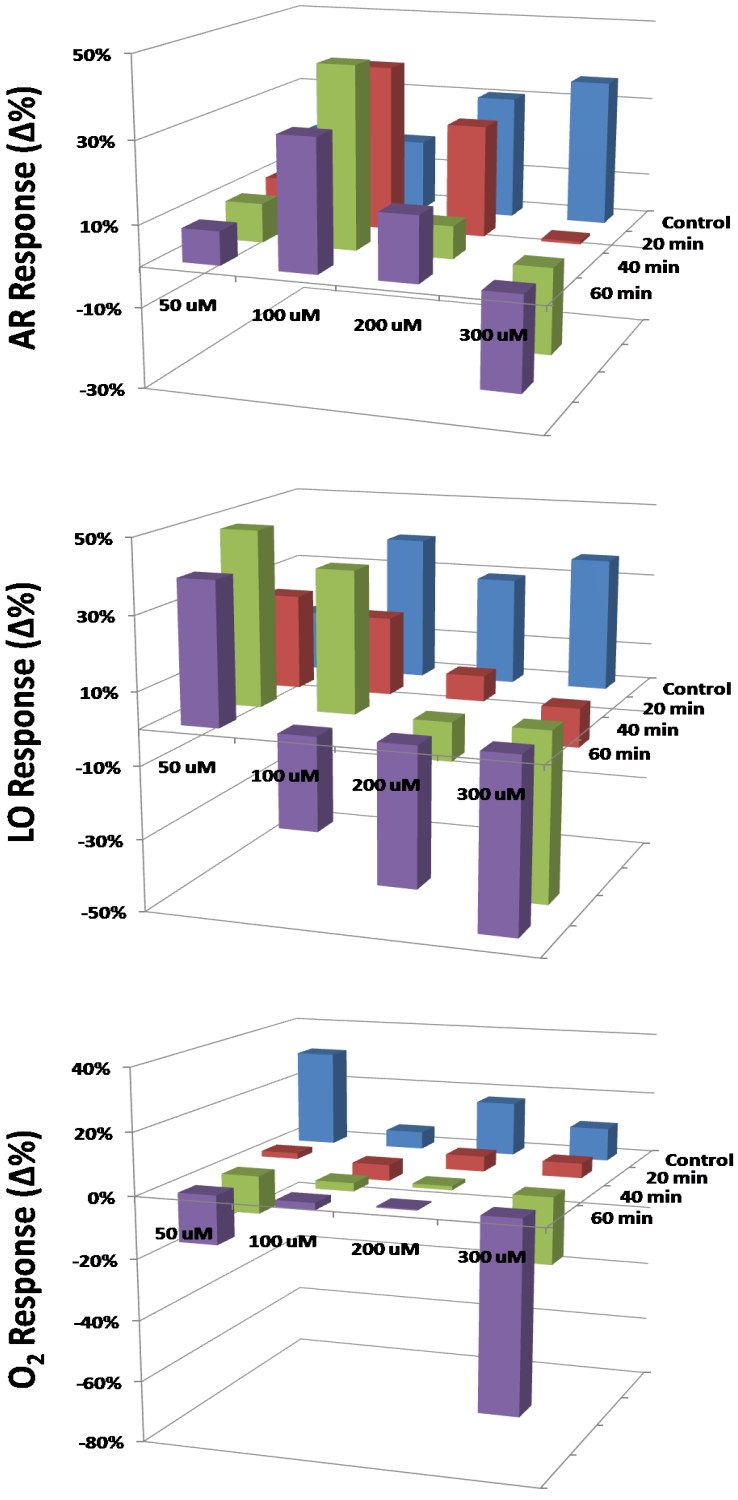

Figure 23. 3D Composite of HNE effects on macrophage oxidative burst metabolism (top) AR rate changes, (middle) LP rate changes, and (bottom) OC rate changes. Rate changes are representative of deviation change as compared to steady state values.

(8 nmols) severely attenuates anaerobic metabolism. The corresponding OC rates for

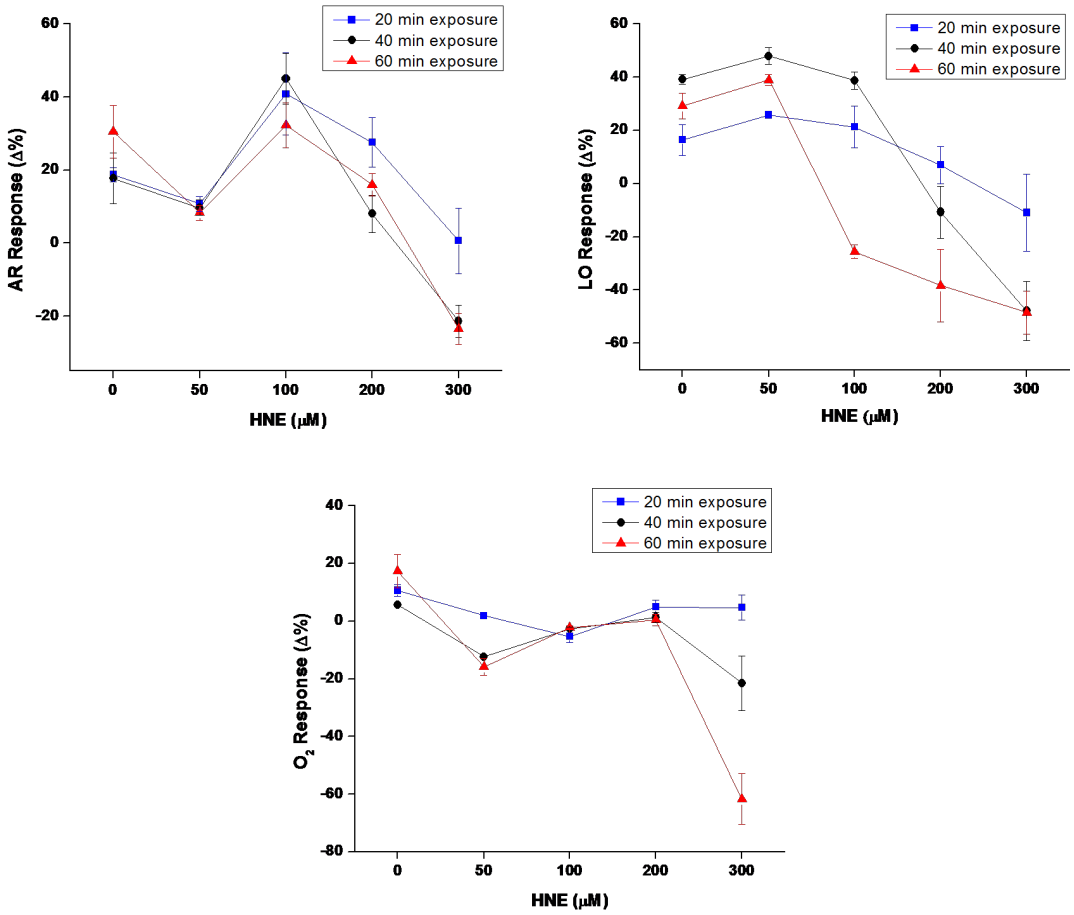

Figure 24. HNE Effects on Macrophage Oxidative Burst Metabolism as a Function of Concentration

high HNE concentrations remain relatively stable without any distinguishable fluctuations, excluding the 300 μM-40min and 300 μM-60min time points.

Collectively, the results of MMP PMA-stimulation measurements show that typical metabolic increases upon PMA activation of NADPH oxidase are severely impaired at concentrations greater than 200 μM HNE and issue a negative metabolic effect at high concentrations. While the effects of HNE on steady state macrophage metabolism occurs in a concentration and time-dependent manner, changes in PMA-activation metabolism were not consistent with respect to cellular metabolism as a whole.

This leads one to believe that inhibition of oxidative burst by HNE is not simply inactivation of the superoxide generating enzyme but the result of changes in downfield intracellular signaling pathways which can lead to incomplete assembly.

HNE Inhibition of Oxidative Burst in RAW 264.7 Cells Assessed by Luminol

To directly determine NADPH oxidase HNE inhibition, RAW 264.7 cells (4E6

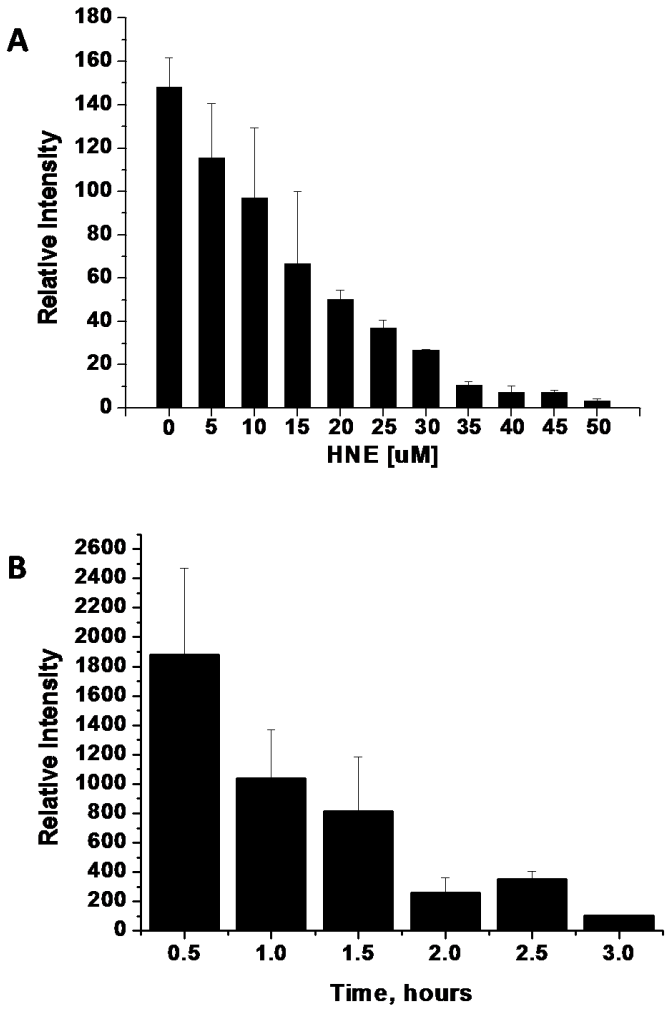

Figure 15. HNE Inhibition of PMA-induced ROS. (A) Concentration-dependent (0-50 μM HNE) and (B) Time-dependent (0-3 hr, 35 μM HNE) inhibition of ROS generation assessed by luminol enhanced chemicluminescence.

cells) were treated with increasing concentrations (0- 50 μM) of HNE for 3 hrs prior to PMA-stimuation and luminol detection of extracellular reactive oxygen species (ROS). RAW 264.7 cells exhibited a concentration-dependent inhibition of ROS with an EC_{50} value of 18.4 ± 1.2 μM (**figure 25A**). This value is consistent with previously published values for murine macrophages which reported an EC_{50} value of 27 μM.[29] To examine the temporal effects of HNE on PMA-induced ROS generation, RAW 264.7 cells were treated with 35 μM HNE for 0-3 hours and subsequently activated with 16 μM PMA to determine the change in ROS generation. The results indicate a time-dependent inhibition of macrophage oxidative burst with a 50% reduction of ROS generation after 1 hour (**figure 25B**). ROS generation was further reduced to 20% following 2 hours of exposure and completely attenuated after 3 hrs. The potent ability of HNE to inhibit ROS generation combined with the time-dependent sensitivity of HNE oxidative burst suggests that other cellular proteins and enzymes are involved.

Formation of HNE Adducts to Protein Kinase C (PKC)

The potent ability of HNE to inhibit ROS generation in a dose and time-dependent manner combined with the HNE-induced disruption of metabolic rates before and after PMA stimulation suggest that the inhibitory effects of HNE originate from downstream signaling or in concert with multiple protein signaling pathways. To investigate the inactiviation of the well documented downstream signaling protein[26], we explored the ability of HNE to chemically modify protein kinase C (PKC) in cultured RAW 264.7 macrophages.

Inhibition of PKC activity has been shown to occur an HNE levels as low as 10 μM.[30] Once activated, PKC functions by phosphorylating a number of downstream

substrate proteins that regulate multiple cellular processes including oxidative burst.[26] Of the eleven known isoforms of PKC, the βII isoform has been implicated in the phosphorylation of p47 phox which ultimately results in the translocation of the cytosolic components of NADPH oxidase to the cellular membrane. Therefore, inhibition of PKC would prevent the assembly of NADPH oxidase. Since HNE readily forms covalent protein modifications, it is plausible that the observed oxidative burst inhibition is due to formation of HNE adducts on key amino acid residues of PKC. While there are several potential protein targets that may be affected by HNE adduction, the connection between increased levels of HNE and decreased PKC activity provides an intriguing target of interest.

To examine the possiblity of HNE adduct formation on intracellular PKC, RAW 264.7 cell lysates were isolated from samples treated in a time-dependent manner (0-3 hr) with 35 μM HNE and examined for the presence of HNE adducts on PKC by western blot analysis. In **figure 26**, a reproducible PKC-labeled band for each untreated time

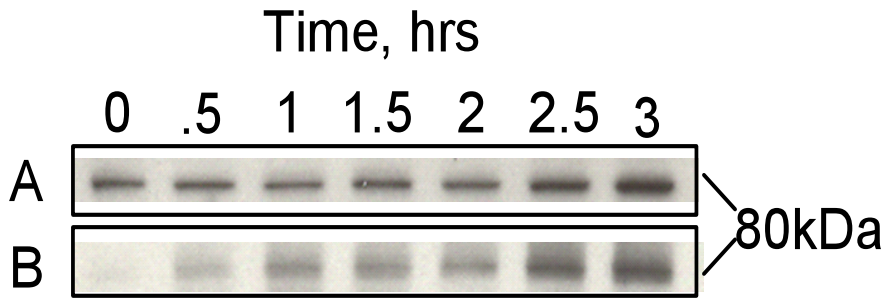

Figure 26. Western blot analysis of HNE-modified PKC from cell lysates. (A) PKC protein bands labeled with monoclonal anti-PKC antibody, (B) 35 μM HNE-treated PKC protein bands labeled with monoclonal anti HNE antibody.

point suggesting cellular integrity remained consistent from 0-3 hrs. After the initial 0 hr time point, HNE-adduct formation became increasingly prominent as a function of exposure time (**figure 26**). The temporal component associated with HNE protein adduction has also been documented for other proteins such as myoglobin which indicated that sterically available basic amino acid residues were requisite for HNE-protein adduct formation. The propensity of HNE to form intracellular protein adducts with PKC in a temporal and concentration-dependent manner clearly demonstrates the complex experimental approach needed to identifying the key proteins, enzymes and other cellular signaling molecules involved HNE impairment of macrophage oxidative burst.

Conclusions

The highly reactive electrophile HNE is a potent fatty acid oxidation byproduct which has been implicated in a wide range of diseases as a marker of oxidative stress.[10] The main mode of cellular HNE toxicity results from covalent adduction and modification of susceptible proteins and enzymes.[31] This body of work set out to examine the metabolic impact of HNE exposure on macrophage function and activation. Using RAW 264.7 macrophages coupled to a modified multianalyte microphysiometer (MMP), three key metabolic species associated with cellular respiration and energy metabolism (oxygen, lactate, and acidification) were monitored in real-time. Upon introduction of HNE in the running media, each metabolic rate displayed a dose and time-dependent reduction in comparison to control experiments.

When treated with 16 μM PMA to induce oxidative burst, a significant increase in metabolic rate was observed for each metabolite suggesting a significant total increase in cellular metabolism as a result of activation. RAW 264.7 cells treated with HNE prior to PMA activation exhibited a reduction in the expected metabolic flux at low concentrations/exposure (0-100 μM) and was completely attenuated or cytotoxic at high concentrations/exposure of HNE (200-300 μM). The one exception was observed for lactate production rates at 100 μM HNE exposure that displayed a 2-fold increase in LP rate, independent of time. Luminol-based studies of PMA-treated cells showed a dose and time-dependent inhibition of ROS production (oxidative burst). The discrepancies in temporal effects associated with lactate measurements and luminol experiments suggest that other requisite signaling proteins/enzymes are involved in oxidative burst inhibition.

Western blot analysis of PKC from RAW 264.7 cell lysates exposed to 35 μM HNE displayed a time dependent sensitivity to HNE adduct formation.

The results of this study clearly show that HNE exposure reduces energy metabolism of RAW 264.7 macrophages in a concentration and time-dependent manner. At high concentrations of HNE (>100 μM), PMA-induced metabolic flux was completely attenuated and even cytotoxic at pretreatment concentrations of 300 μM. In addition, a new signaling protein target of interest (PKC) was indentified which leads to speculation of the exact nature of HNE toxicity. In order to understand the dynamics of HNE inhibition of oxidative burst, a further analysis of HNE interaction with the NADPH oxidase signaling pathway is needed.

References

1. Grune, T.; Siems, W. G.; Schonheit, K.; Blasig, I. E. *Int J Tissue React* **1993**, *15*, 145-50.

2. Montine, T. J.; Huang, D. Y.; Valentine, W. M.; Amarnath, V.; Saunders, A.; Weisgraber, K. H.; Graham, D. G.; Strittmatter, W. J. *J Neuropathol Exp Neurol* **1996**, *55*, 202-10.

3. Sayre, L. M.; Zelasko, D. A.; Harris, P. L.; Perry, G.; Salomon, R. G.; Smith, M. A. *J Neurochem* **1997**, *68*, 2092-7.

4. Selley, M. L. *Free Radic Biol Med* **1998**, *25*, 169-74.

5. Soares, A. F.; Guichardant, M.; Cozzone, D.; Bernoud-Hubac, N.; Bouzaidi-Tiali, N.; Lagarde, M.; Geloen, A. *Free Radic Biol Med* **2005**, *38*, 882-9.

6. Uchida, K.; Toyokuni, S.; Nishikawa, K.; Kawakishi, S.; Oda, H.; Hiai, H.; Stadtman, E. R. *Biochemistry* **1994**, *33*, 12487-94.

7. Eklund, S. E.; Thompson, R. G.; Snider, R. M.; Carney, C. K.; Wright, D. W.; Wikswo, J.; Cliffel, D. E. *Sensors* **2009**, *9*, 2117-2133.

8. Marnett, L. J.; Riggins, J. N.; West, J. D. *J Clin Invest* **2003**, *111*, 583-93.

9. Hill, B. G.; Dranka, B. P.; Zou, L.; Chatham, J. C.; Darley-Usmar, V. M. *Biochem J* **2009**, *424*, 99-107.

10. Poli, G.; Schaur, R. J. *IUBMB Life* **2000**, *50*, 315-21.

11. Carney, C. K.; Schrimpe, A. C.; Halfpenny, K.; Harry, R. S.; Miller, C. M.; Broncel, M.; Sewell, S. L.; Schaff, J. E.; Deol, R.; Carter, M. D.; Wright, D. W. *J Biol Inorg Chem* **2006**, *11*, 917-29.

12. Schwarzer, E.; Kuhn, H.; Valente, E.; Arese, P. *Blood* **2003**, *101*, 722-8.

13. Forman, H. J.; Torres, M. *Mol Aspects Med* **2001**, *22*, 189-216.

14. Neely, M. D.; Amarnath, V.; Weitlauf, C.; Montine, T. J. *Chem Res Toxicol* **2002**, *15*, 40-7.

15. Eklund, S. E.; Taylor, D.; Kozlov, E.; Prokop, A.; Cliffel, D. E. *Anal Chem* **2004**, *76*, 519-27.

16. Eklund, S. E.; Cliffel, D. E.; Kozlov, E.; Prokop, A.; Wilkswo, J.; Baudenbacher, F. *Analytica Chimica Acta* **2003**, *496*, 93-101.

17. Eklund, S. E.; Snider, R. M.; Wikswo, J.; Baudenbacher, F.; Prokop, A.; Cliffel, D. E. *J. of Electroanalytical Chemistry* **2006**, *587*, 333-339.

18. Hafner, F. *Biosens Bioelectron* **2000**, *15*, 149-58.

19. McConnell, H. M.; Owicki, J. C.; Parce, J. W.; Miller, D. L.; Baxter, G. T.; Wada, H. G.; Pitchford, S. *Science* **1992**, *257*, 1906-12.

20. Wille, K.; Paige, L. A.; Higgins, A. J. *Receptors Channels* **2003**, *9*, 125-31.

21. Owicki, J. C.; Parce, J. W. *Nature* **1990**, *344*, 271.

22. Owicki, J. C.; Parce, J. W.; Kercso, K. M.; Sigal, G. B.; Muir, V. C.; Venter, J. C.; Fraser, C. M.; McConnell, H. M. *Proc Natl Acad Sci U S A* **1990**, *87*, 4007-11.

23. Schrimpe, A. C.; Wright, D. W. *Chem Res Toxicol* **2009**.

24. Mosior, M.; Newton, A. C. *J Biol Chem* **1995**, *270*, 25526-33.

25. Greene, N. M.; Williams, D. S.; Newton, A. C. *J Biol Chem* **1995**, *270*, 6710-7.

26. Newton, A. C. *J Biol Chem* **1995**, *270*, 28495-8.

27. Schwarzer, E.; Turrini, F.; Ulliers, D.; Giribaldi, G.; Ginsburg, H.; Arese, P. *J Exp Med* **1992**, *176*, 1033-41.

28. Siems, W. G.; Capuozzo, E.; Verginelli, D.; Salerno, C.; Crifo, C.; Grune, T. *Free Radic Res* **1997**, *27*, 353-8.

29. Dianzani, C.; Parrini, M.; Ferrara, C.; Fantozzi, R. *Cell Biochem Funct* **1996**, *14*, 193-200.

30. Schwarzer, E.; Arese, P. *Biochim Biophys Acta* **1996**, *1316*, 169-75.

31. Vila, A.; Tallman, K. A.; Jacobs, A. T.; Liebler, D. C.; Porter, N. A.; Marnett, L. J. *Chem Res Toxicol* **2008**, *21*, 432-44.

CHAPTER IV

NOVEL HAIRPIN DNA-COATED GOLD NANOPARTICLES FOR THE DETECTION OF METASTATIC MELANOMA

Introduction

In the United States alone, one in three people are at risk of developing some form of cancer during their lifetime.[1] With more than one million new cases in the US this year alone, skin cancer has become the prevalent diagnosis among all forms of cancer.[1] Melanoma is one of the fastest growing forms of diagnosed cancer in the United States with nearly 70,000 new cases in the US this year alone.[1] Early detection of melanoma is essential for a positive outcome, given that nearly 80% of all cases diagnosed early result in a ten year survival rate.[3] This highlights the need for new and sensitive diagnostic approaches capable of providing early and accurate assessment.

The most common method for diagnosis of malignant melanoma is histological examination which is invasive, highly interpretable, and requires a significant accumulation of cancerous cells.[4] Once metastasis occurs, screening methods are ineffective because of melanoma heterogeneity and a lack of accumulation of melanoma cells in the peripheral blood. Current techniques for diagnosing late stage melanoma utilize both antibody-assisted protein detection and reverse transcription-polymerase chain reaction (RT-PCR) to identify proteins and protein expression targets associated with metastatic melanoma.[5-8] Both techniques have proven to be effective in identifying melanoma metastasis but suffer from tedious sample processing and conflicting results.[8,9]

Several melanoma markers have been indentified to date which specifically detect tumor cells derived from the melanocyte lineage.[8] The most widely studied melanoma-specific marker is the expression of the tyrosinase gene.[4,5,10] Tyrosinase (TYR) is an enzyme involved in the conversion of tyrosine to melanin during melanin biosynthesis (**figure 27**).[2] TYR is expressed by normal melanocytes, melanoma cells, as well as some forms of brain and colon cancers.[2] The cell specificity of TYR gene expression makes it an ideal target for detecting metastatic melanoma in the blood, lymph nodes or other organs.[11]

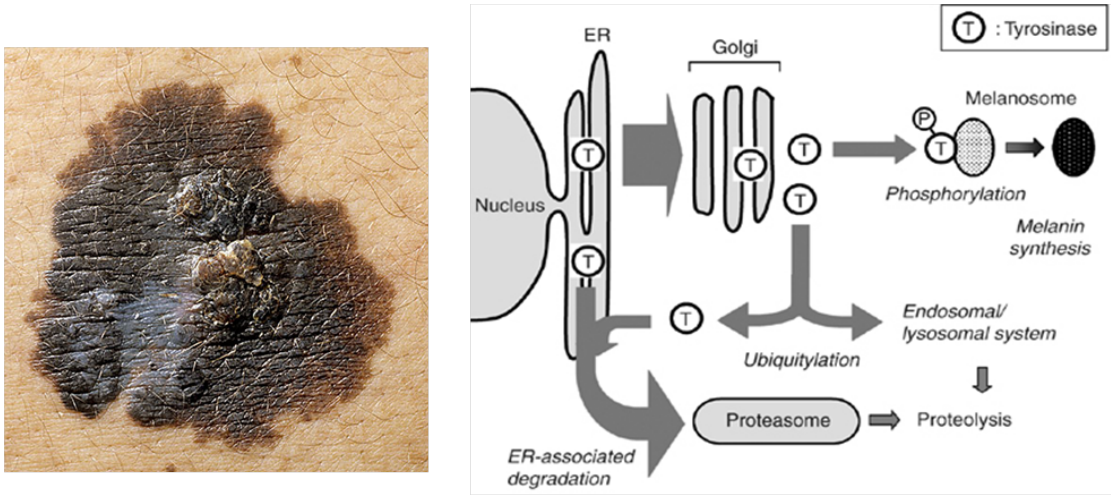

Figure 27. Tyrosinase-mediated Melanin Biosynthesis. (left) Assymetrical melanoma lesion. (right) Melanin biosynthetic pathway. (Copyright, FASEB 1991) [2]

Gene expression refers to the mRNA signaling process that is responsible for translation and assembly of the intact proteins. RT-PCR is considered the gold standard for identification and quantification of cellular mRNA and has been used for a variety of studies to identify TYR mRNA in melanoma patients with conflicting results.[7,8,12] RT-PCR is a technique that proceeds via (1) reverse transcriptase-dependent conversion of

RNA into complement DNA (cDNA), (2) PCR amplification of the ensuing cDNA and (3) detection of amplification products in real-time. While a powerful technique with excellent sensitivity, RT-PCR requires extensive sample preparation, terminal cell lysis for RNA harvesting, and laborious reaction optimization. Additionally, spatial and temporal information of mRNA-specific processes are not available.

Several live cell imaging probes and techniques have been developed for intracellular mRNA imaging and include linear oligonucleotide probes, hairpin oligonucleotide probes (or molecular beacons) and Förster resonance energy transfer reporters.[13-16] While effective, these mRNA imaging techniques require additional reagents for delivery into the cytoplasm by means of electroporation[17], chemically-mediated membrane permeabilization[17,18] and/or cationic cell-penetrating peptides.[13] Additionally, free oligonucleotide imaging probes, such as molecular beacons, are highly succeptible to endogenous nuclease-degradation, and readily exhibit false-positive signals using artifical transfection methods.[17,19-21]

The use of nanotechnology coupled with traditional biodiagnostics has recently shown to be beneficial in developing noninvasive diagnostic platforms.[22,23] Current advances in oligonucleotide-functionalized gold nanoparticles (AuNP) have proven to circumvented the potential pitfalls of traditional molecular beacon imaging by eliminating the need for invasive transfection agents.[24,25] Additionally, hypothesized steric bulk effect associated with the gold nanoparticle scaffold reduced intracellular nuclease degradation by an order of magnitude as compared to free molecular beacons.[25]

Applications of nanotechnology to the biodiagnostic field hold promise for the development of new platforms capable of improving current melanoma detection.

Herein, we present a new hairpin DNA functionalized gold nanoparticle that positively identifies tyrosinase mRNA in both melanoma cell lines and primary tumor cultures. A multiplexed analysis of multiple melanoma markers was explored by incorporation of two additional melanoma marker inspired probes and a standard housekeeping gene probe for investigating intracellular gene expression in multiple melanoma cell lines.

Experimental

Materials and Methods

All chemicals were used as received unless otherwise noted. The human cell lines, SK-MEL-28 and HEp-2, were obtained from the American Type Culture Collection (ATCC). Additional human melanoma cell lines used in profiling experiments (Wm115, MeWo and HS-294T) were kindly provided by Donna Hick, Vanderbilt Ingram Cancer Center (VICC). 15 nm gold colloid solutions were obtained from Ted Pella, Inc (Redding, CA). Syto-13 nuclear dye (Sy13), Sytox Green viability dye (SxG), Mito-tracker Orange (MO) and sterile nuclease free phosphate buffered saline without $MgCl_2$ and $CaCl_2$ (PBS, pH 7.4) were obtained from Invitrogen Corp (Carlsbad, CA). Bovine deoxyribonuclease I (DNase I) was purchased from Promega (Madison, WI). Molecular beacons (MB), unmodified oligonucleotides, custom oligonucleotides and PCR primers were purchased from Biosearch Technologies, Inc (Novato, CA). All other chemicals were purchased from Sigma Aldridge, Inc (St. Louis, MO).

Hairpin Oligonucleotides

The mRNA recognition sequences used for this study were as follows: (TYR Rec. Seq) 5'-attgtgcatgctgctttgag-3'; (S100β Rec. Seq) 5'-cagtagtaaccatggcaaca-3'; (MIA Rec. Seq) 5'-aggtttcagggtctggtcct-3'; (βactin Rec. Seq) 5'-ggagttgaaggtagtttcgt-3' and (MisMatch Rec. Seq) 5'-gtattggaagtcgttcgatgatcactcgc-3' or 5'-ggagttgaaggtagtttcgt-3'. Each recognition sequence was extensively BLAST searched to confirm either target specificity (100% overlap) or non-specificity (MM rec seq) with minimal overlap with

other potential human gene transcripts (<70%). Prior to use, thiol-terminated oligonucleotides were subjected to 0.1 M dithiolthreitol (DTT) reduction of the 5' thiol moiety. Excess reducing agent was removed by 3K molecular weight centrifugal filtration and washed three times with PBS (Amicon Ultracel 3K, Millipore). Freshly reduced oligonucleotides were stored in 1X Tris EDTA (TE) buffer (pH 8) at -80^{o}C until use.

hAuNP Sysnthesis

Briefly, a 10 nM solution of citrate-stabilized AuNPs (15 nm) was incubated with 2 μM freshly reduced DNA overnight at room temperature and protected from light. After the initial loading period, the resulting solution was buffered to 10 mM phosphate buffer (PB, pH 7) with 0.1% Tween-20 and vortexed for 30 sec. Three successive aloquots of 5M NaCl were added to the buffered solution in 2hr intervals until a final concentration of 0.3 M NaCl was achieved. The resulting hAuNPs were purified by three centrifugation washes (30 min, 17,000 x g) and stored in phosphate buffered saline (PBS, pH 7.4) at 4^{o}C.

Cell Viability

The cell viability dye Sytox Green was employed for all flow cytometric analysis. Trypan blue exclusion was utilized for all other experiments.

Cell Culture

SK-MEL-28, Wm115, MeWo, HS-294T and HEp2 cells were cultured in high glucose DMEM growth medium supplemented with 10% fetal bovine serum (FBS), 100 units of penicillin/streptomycin and 2% L-glutamine. Primary cell cultures were maintained in RPMI 1640 growth medium supplemented with 10% fetal bovine serum (FBS) , 100 units of penicillin/streptomycin and 2% L-glutamine. Phenol-red free RPMI 1640 supplemented with 5% FBS was used for all live-cell fluorescence experiments. Co-culture experiments were performed by adding equal cell volumes (e.g. 5e5 Mels / 5e5 HEp2, total cell count = 1e6) to either a 35mm Mattek microwell dish or well plates and allowed to adhere to the surface > 4hrs before treatment with hAuNPs in complete growth medium.

Dynamic Light Scattering (DLS)

All DLS measurements were performed on a Malvern Zetasizer Nano ZS. Particle measurements were performed at a concentration of 1 nM in water and measured in triplicate. To determine the size of 'open' TYR hAuNPs, a 1 nM solution of TYR hAuNPs was treated with 1 μM TYR recognition complement and incubated at 37^{o}C for 2 hours prior to measurement.

Absorption and Fluorescence Measurements

Absorption measurements were performed on an Agilent 8453 diode-array spectrophotometer. The concentration of AuNPs and hAuNPs was determined by measuring the absorbance at 520 nm ($\varepsilon = 3.64 \times 10^8$ $M^{-1}cm^{-1}$).[26] The emission spectrum

of 'open' TYR hAuNPs was obtained by treating a 5 nM solution of TYR hAuNPs (PBS, 0.1% Tween-20) with 1 μM TYR recognition complement and incubating at 37°C for 2 hours. Fluorescence spectra of the resulting 'open' TYR hAuNP solution was generated on a Cary Eclipse Fluorescence Spectrophotometer by exciting at 620 nm and measuring the emission from 650 to 750 nm. Target selectivity assays and DNase I susceptibility measurements were performed using a Bio-Tek Synergy HY multidetection fluorescent microplate reader using a 590/35 excitation filter and a 645/40 emission filter.

hAuNP Target Selectivity

To measure selectivity of the hAuNP probe, TYR hAuNPs (1 nM, PBS, 0.1% tween-20) were titrated with increasing concentrations of TYR recognition complement (0-1 μM) and MM DNA (0-1 μM) keeping a total volume of 200 μl. The resulting solutions were sealed, protected from light and allowed to hybridize for 2 hours at 37°C. Fluorescence intensities were measured as described above and plotted as a function of complement concentration. Signal to noise was determined by the ratio of TYR target fluorescence versus MM background fluorescence.

Specificity of additional probe designs for S100β, MIA and β-actin were performed in a similar manner by incubating each hAuNP (1 nM) with 1 μM target complement and 1μM MM DNA. As before, solutions were sealed, protected from light and allowed to incubate for 2 hr at 37°C. Signal to noise was determined by the ratio of target fluorescence versus MM background fluorescence.

DNase I Susceptibility

To determine hAuNP suceptibility to nuclease degredation, TYR hAuNPs and free molecular beacons were analyzed. The following tyrosinase-specific molecular beacon was employed: (TYR MB Seq) 5'-Cy5-cgacgattgtgcatgctgctttgagcgtcg-BHQ3-3'. TYR hAuNP solutions (2.2 nM) and TYR MBs (200 nM) were diluted in nuclease reaction buffer (100 mM Tris-HCl, 5 mM $MgSO_4$, 1 mM $CaCl_2$, pH 8.0) and 100 µl aliquots of each added to a 96-well black wall microplate. Both TYR hAuNPs and TYR MBs were treated with 10 µl of either: 1 U/mL DNase (excess, endpoint determination), 1 U/L DNase (optimum), or PBS (baseline) and transferred immediately to a preheated fluorescent microplate reader (37^{o}C). Fluorescence output for each well was monitored every 300 seconds for 3 hours to generate degradation progress curves for each sample. DNase susceptibility was evaluated by the slope of the initial linear region.

Scanning Confocal Microscopy

Cells were grown in 35 mm Mattek dishes and kept at approximately 50% confluence. Cells were treated with 0.5 nM hAuNPs in complete media. After the 4 hr loading period, the cells were washed twice with PBS and fresh medium was added to the dish. After incubating for 12 hours at 37^{o}C, the media was removed and fresh phenol-red free media added to the dish. For images with a green nuclear stain, cells were treated with 25 nM Syto-13 for 15 minutes prior to imaging. For images with an orange mitochondrial stain, cells were treated with 5 nM Mito-Tracker Orange for 15 minutes prior to imaging. All images were captured on a Zeiss LSM 510 Meta inverted confocal microscope with identical optical settings for each session. Fluorescent images were

captured using the following excitation lasers and corresponding filter sets: Syto13 nuclear stain (488nm; bandpass 505-530nm) and quasar 670 hAuNP probe (633nm; longpass 650nm).

Flow Cytometry

Cells were grown in 6 well plates (1e6 cells/well) and treated with 0.5 nM hAuNPs as described above. After a 12 hr hybridization period, cells were lifted from the plate with 0.05% trypsin-EDTA, washed twice with cold PBS, resuspended in 500 µl of cold phenol-red free media containing 5% FBS and stored on ice until analyzed. The addition of Sytox Green (50 nM) to each sample was used to assess cellular integrity and tolerance of hAuNPs. Samples were analyzed on a Custom Becton Dickinson five-laser LSRII analytical flow cytometer using forward and side scatter focusing. Sytox Green and Cy5 emissions were monitored simultaneously for 10,000 events and a mean fluorescence for each fluorescent signal was recorded.

Reverse-transcription polymerase chain reaction (RT-PCR)

To confirm the presence, absence and comparative expression levels of each melanoma marker, RT-PCR was performed for all cell lines. Cellular mRNA was extracted from each cell line using the RNeasy Mini Kit (Qiagen) according to the manufacturers protocol. Purified mRNA was quantified by UV-Vis. RT-PCR was performed using a Rotor-Gene Q real time cycler (Qiagen) and QTaq One-Step qRT-PCR SYBR Kit (Clontech). Briefly, 15 ng (5 µL) of RNA from each cell line was reverse-transcribed and amplified in a 25 µL reaction volume with the following components:

12.5 μL of 2X One-Step qRT-PCR Buffer plus SYBR, 0.5 μL of 50X QTaq DNA Polymerase Mix, 0.4 μL of 60X qRT Mix, 200 nM forward and reverse primers, and DNase/RNase free water. The following primers were employed: TYR Forward (5'-ttggcagattgtctgtagcc-3'), TYR Reverse (5'-aggcattgtgcatgctgctt-3'), S100β Forward (5'-atgtctgagctggagaaggccat-3'), S100β Reverse (5'-actgcctgccacgagttctttgaa-3'), MIA Forward (5'-catgcatgcggtcctatgcccaagctg-3'), MIA Reverse (5'-gataagctttcactggcagtagaaatc-3'), β-Actin Forward (5'-gcgggaaatcgtgcgtgacatt-3') and β-Actin Reverse (5'-gatggagttgaaggtagtttcgtg-3'). Cycling conditions were as follows: 45 min at 48^{o}C, 3 min at 95^{o}C, followed by 40 cycles each of 1 min at 55^{o}C and 2 min at 72^{o}C. 5 μL of the TYR and β-actin PCR products were subjected to electrophoresis on a 1.2% agarose E-gel (Invitrogen) and visualized under UV light. The expected sizes of the PCR products were 289 bp (tyrosinase) and 232 bp (β-actin). For profiling experiments, Ct values were process based on the comparative Ct method where the relative transcript level of each target gene was calculated according to the equation $2^{-\Delta Ct}$, where ΔCt is defined as Ct target gene - Ct βactin gene.

hAuNP Melanoma Profile Experiments

hAuNP profile experiments were carried out in a similar manner in comparison to flow cytometric analysis as described above. The human melanoma cell lines SK-MEL-28, Wm115, MeWo and HS-294T as well as the non-melanoma cell line HEp2 were employed for all profiling experiments. Cells were plated at a concentration of 1E6 cells per well in 6 well plates and treated with 0.25 nM melanoma target hAuNPs / 0.25 nM

βactin hAuNPs simultaneously for 4 hrs followed by a 12 hr hybridization period and analyzed by flow cytometry.

Results and Discussion

AuNPs offer unique physical and optical properties as potential probes in that they readily enter cells without the need for transfection agents, are non-cytotoxic and can efficiently quench fluorescent molecules when in close proximity to the particle surface.[24,25,27-30] To circumvent the inherent pitfalls associated with current mRNA detection methods such as RT-PCR and molecular beacons, an mRNA imaging probe combining gold nanoparticles with current molecular beacon-based technologies, termed hairpin DNA-coated gold nanoparticles (hAuNP), was developed.

This modular nanoscale construct consists of a core gold nanoparticle (15 nm

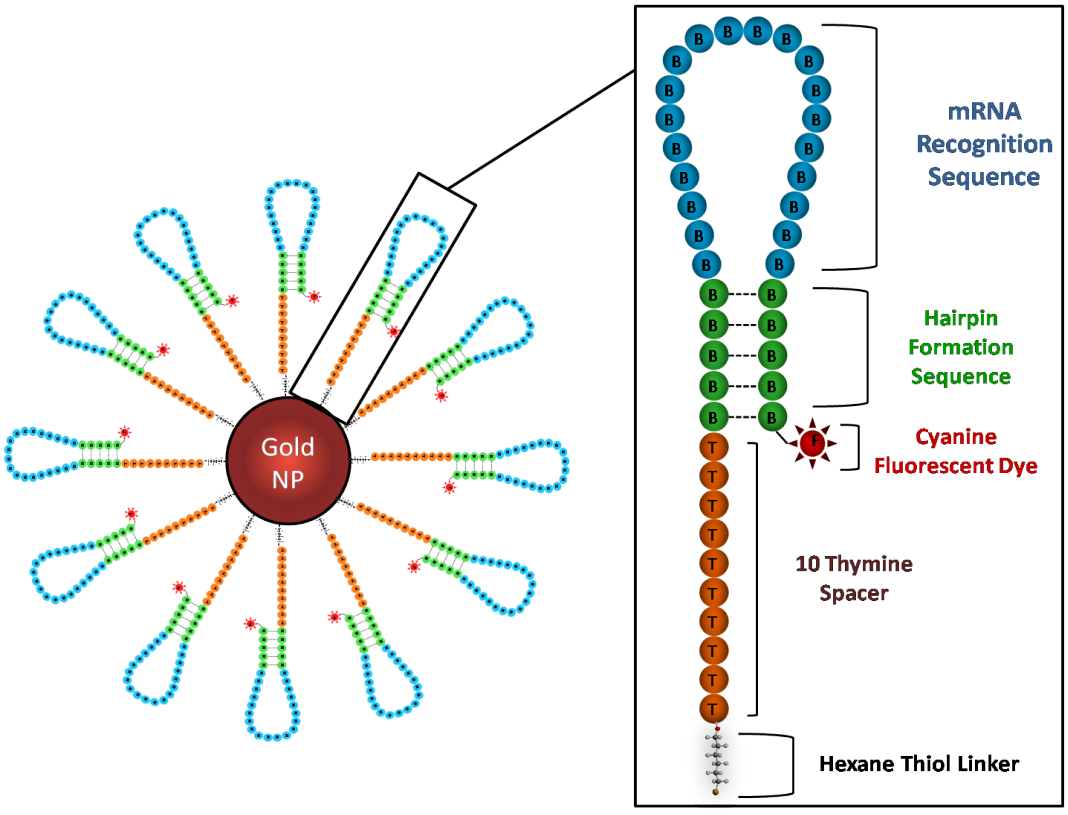

Figure 28. Schematic of hAuNP Design

diameter) with covalently attached thiol-terminated DNA hairpin oligonucleotides. (**figure 28**) Each DNA hairpin beacon is constructed of a 5' hexane thiol linker covalently attached to a 10 thymine extension followed by a 20 base recognition hairpin loop complementary to its mRNA target. The recognition loop is flanked on each side by five complementary bases to create the hairpin secondary structure. When the hairpin DNA is in the closed position, a 3' modified fluorescent dye is quenched by its proximity to the AuNP surface. In the presence of its target complement, hybridization of the twenty base recognition loop releases the fluorescent molecule from its closed state to an open fluorescent state (**figure 29**).

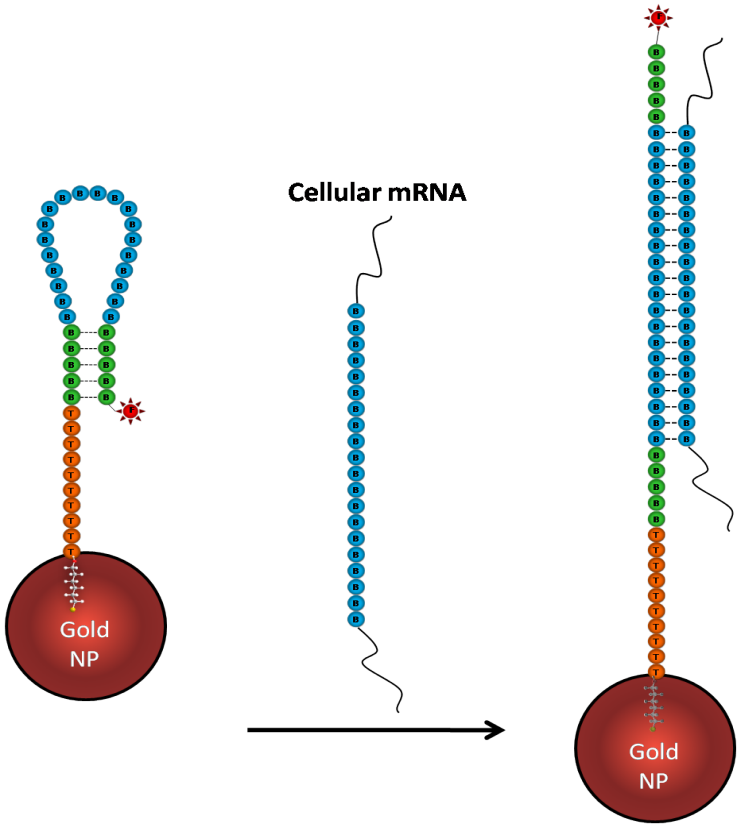

Figure 29. hAuNP mRNA Detection Scheme

To test this modular mRNA probe, we designed the recognition loop to be complementary to the common melanoma gene target tyrosinase. When designing the recognition loop, extensive BLAST search analysis was performed to ensure specificity to its cellular mRNA target. The oligonucleotide loading for each particle was determined by subjecting a 10 nM solution of hAuNPs to dithiolthreitol reduction to reduce the Au-thiol bonds and precipitate the gold particles. The oligonucleotide-to-particle ratio was determined to be ~90 DNA strands per hAuNP. Dynamic light scattering (DLS) confirmed the conformational change of hairpin DNA on the surface of the AuNP resulting in an average diameter of 23.1 ± 1.2 nm post synthesis and 27.6 ± 0.8 nm in the presence of excess complementary DNA. Absorption spectroscopy confirmed that the characteristic 522nm plasmon peak remains unchanged after covalent attachment of DNA to the particle surface. The fluorescent spectral properties of the 3' fluorophore, Quasar 670, were fully retained with an excitation maximum of 647 nm and emission maximum of 667 nm when reacted with complement.

To determine the specificity and robustness of the TYR hAuNP probe, specificity of tyrosinase hAuNPs (TYR hAuNPs) was determined by titration with a 20 base complement versus a 20 base non-complementary oligonucleotide (both having an equal GC content) for 2 hr at 37^{o}C (**figure 30**). As expected, TYR hAuNPs showed good specificity with a 3 fold increase in signal for the proper TYR complement when compared to mismatch DNA.

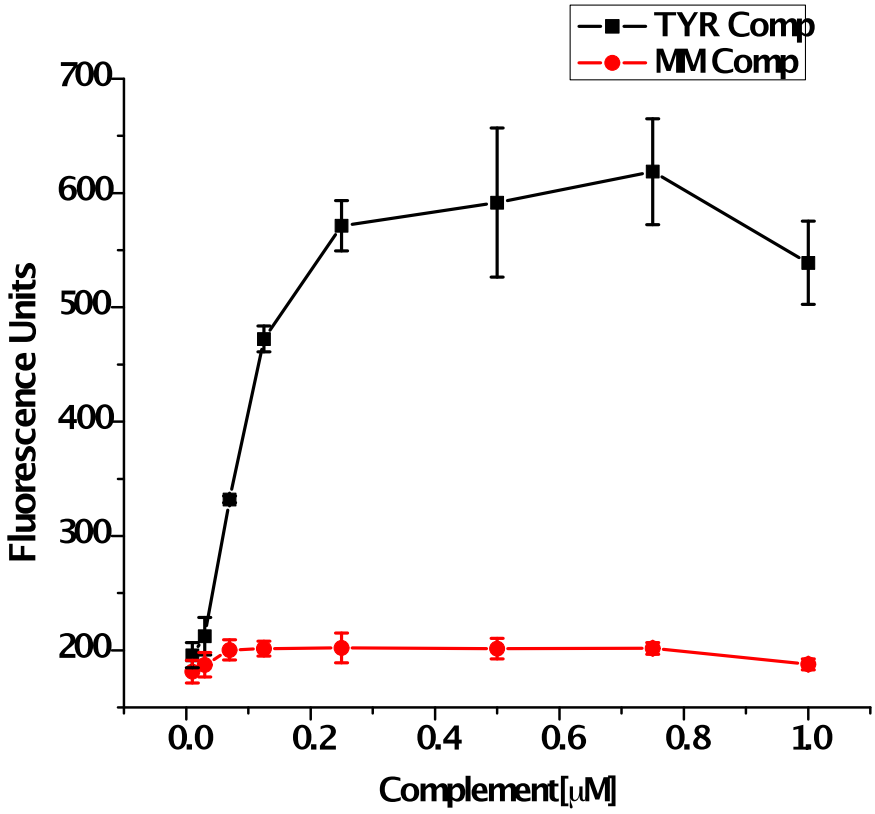

Figure 30. TYR hAuNP Target Selectivity Assay. TYR hAuNPs (1 nM) treated with increasing amounts of TYR recognition complement (black) and MM complement (red). The ratio of TYR target fluorescence versus MM background fluorescence yielded a S/N =3 at complement concentrations > 250 nM.

With any intercellular fluorescent oligonucleotide probe, endogenous nuclease degradation is of particular concern and often results in a high background and/or false positives.[17] The stability of TYR hAuNPs against nuclease degradation was determined by comparison of TYR hAuNPs (2.2 nM) and TYR molecular beacons (TYR MB, 200 nM) when treated with DNAse I (0.1 U/L) at 37°C for 3 hr. Over time, TYR hAuNPs proved to be far superior with a 12.5 fold decrease in nuclease degradation (0.097 nmol/min) as compared with TYR MBs (1.22 nmol/min) (**figure 31**). Such a decrease in

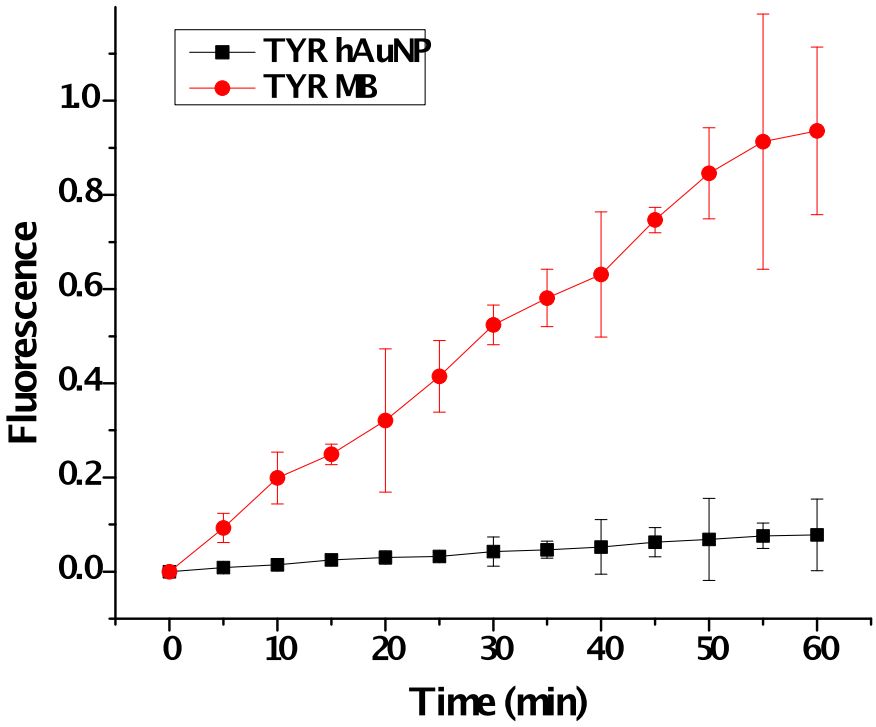

Figure 31. DNase I Susceptibility Assay. TYR hAuNPs (2.2 nM, black) and TYR MBs (200 nM, red) treated with DNase (1U/L). Rate of enzymatic degradation was determined by the slope of the initial linear region (shown above). TYR hAuNPs rate of degradation: 0.097 nmols/min. TYR MB rate of degradation: 1.22 nmols/min.

nuclease susceptibility makes these probes much more attractive than free MBs within the cytoplasm of the cell.

To examine the utility of TYR hAuNPs as intracellular mRNA probes, the SK-MEL-28 melanoma cell line was used as a testing platform due to their inherent elevated tyrosinase gene expression.[31] SK-MEL-28 cells were incubated with 0.5 nM TYR hAuNPs in complete media for 4 hrs followed by a 12 hr hybridization period during which fresh media was added to the cells. After incubation, treated melanoma cells were lifted from the plate and analyzed by flow cytometry which confirmed both a > 99%

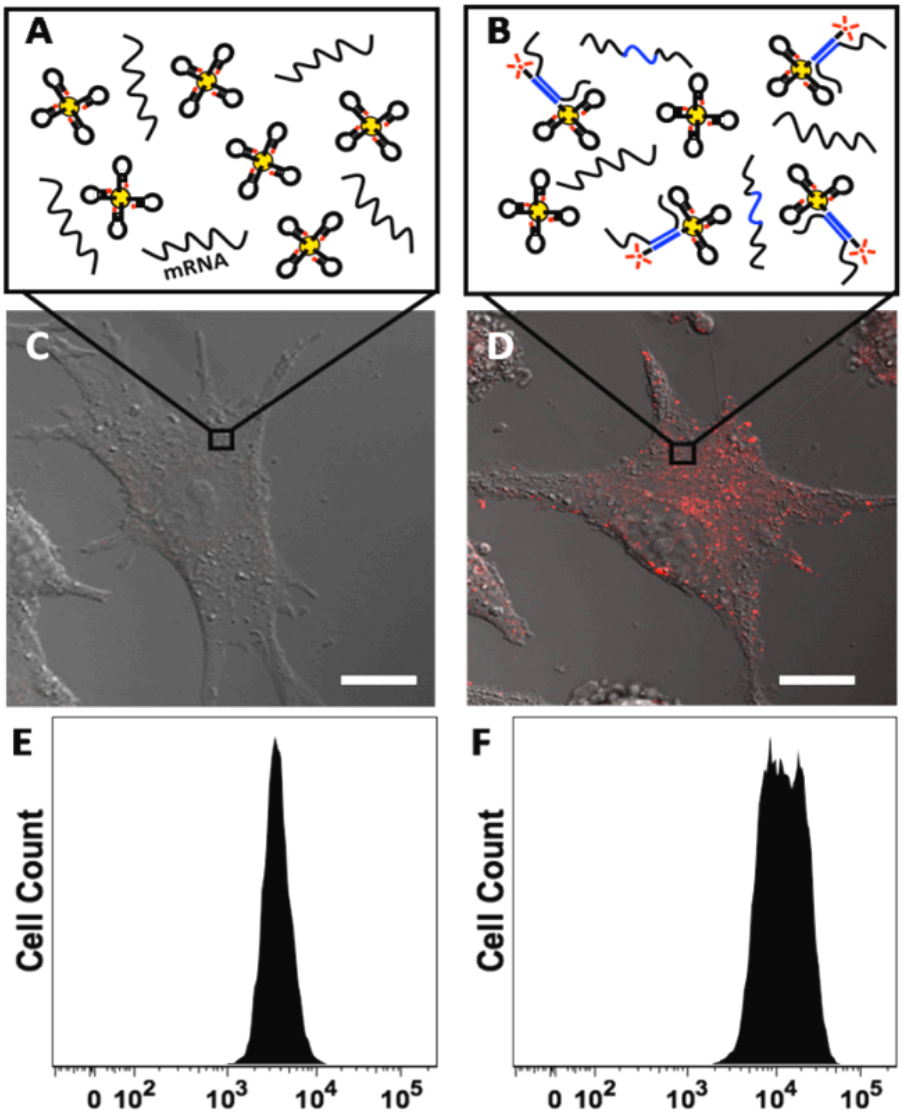

Figure 32. Hairpin DNA-coated gold nanoparticle (hAuNP) labeling of SK-MEL-28 melanoma cells. Schematic representation of the intercellular activity of non-specific mismatch (MM) hAuNPs (A) and tyrosinase-specific (TYR) hAuNPs (B). Confocal imaging of SK-MEL-28 cells treated with MM hAuNPs (C) and TYR hAuNPs (D). Flow cytometric analysis of SK-MEL-28 cells treated with MM hAuNPs (E) and TYR hAuNPs (F) with corresponding mean fluorescence values of 4k and 14K, respectively. Scale bars: 20 μm

transfection efficiency of nanoparticles and > 95% cell viability as compared to untreated cells. When compared to similar constructs such as nano-flares[25], these hAuNP probes similarly diffuse into the mRNA-rich cytoplasm of the cell and maintain high cell viability.[25] Since TYR hAuNPs readily enter cells without the need for transfection

reagents, the ability of TYR hAuNPs to discriminate a specific intracellular mRNA target was investigated. SK-MEL-28 cells were treated with TYR hAuNP and nonspecific mismatch (MM) hAuNPs and imaged by confocal microscopy. TYR hAuNPs treated cells displayed a strong fluorescent signal while those treated with MM hAuNP treated cells showed none (**figure 32C-D**). Flow cytometry was performed to quantitatively confirm the strong fluorescent signal observed in TYR hAuNP treated cells. TYR hAuNP and MM hAuNP treated SK-MEL-28 cells exhibited a substantial difference in cellular fluorescence by which TYR hAuNP treated cells displayed a 3.5 fold increase in fluorescence as compared to MM hAuNP treated cells (**figure 32E-F**).

To test the ability of TYR hAuNPs to discern positive and negative expression of tyrosinase, SK-MEL-28 cells only, HEp2 cells only and a 50/50 mixed coculture of each were treated with 0.5 nM TYR hAuNPs and analyzed by scanning confocal microscopy.

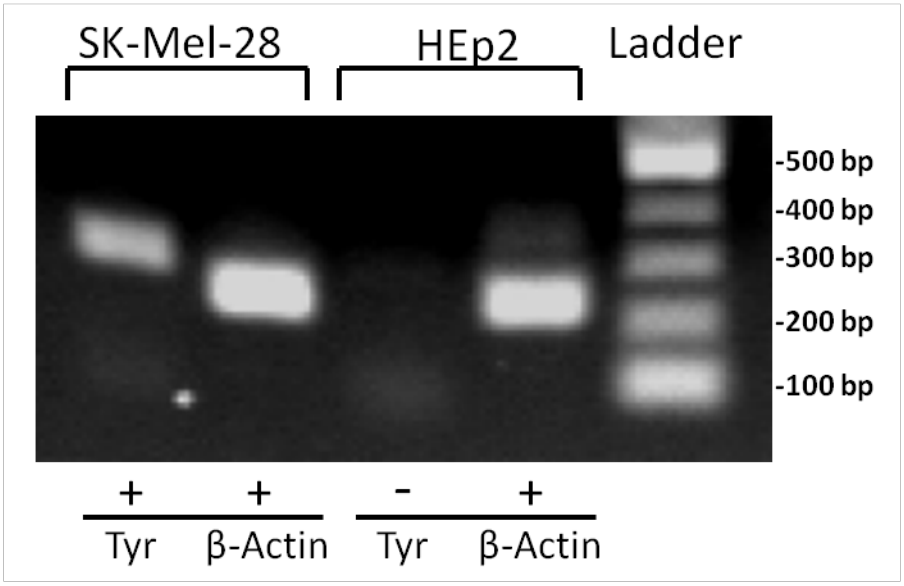

Figure 33. RT-PCR Analysis of Tyr expression in SK-MEL-28 and HEp2 cells. RNA isloated from SK-MEL-28 and HEp2 cells was subjected to RT-PCR and visualized by agarose gel electrophoresis. The 289 bp tyrosinase PCR fragments were present in SK-MEL-28 cells and absent from HEp2 cells. The 232 bp β-actin PCR fragments were abundant for both cells lines.

HEp2 cells provide a viable non-melanocytic cellular control as they have a comparable hAuNP transfection rate (>99%), do not express tyrosinase and can be simultaneously cultured with SK-MEL-28 cells without compromising cell viability. RT-PCR of cellular mRNA isolated from both SK-MEL-28 and HEp2 cells confirmed the presence and absence of tyrosinase mRNA, respectively (**figure 33**).

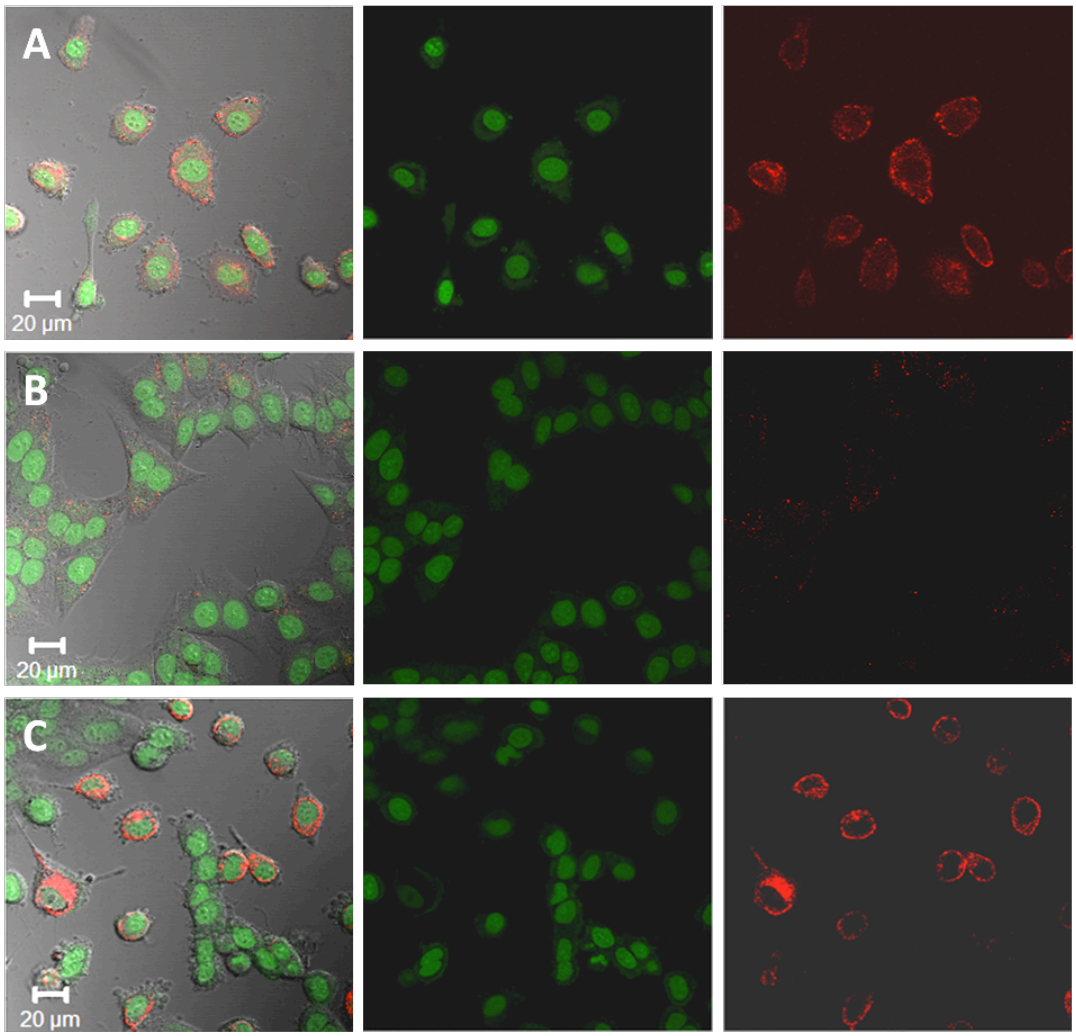

Figure 34. Coculture composite confocal imaging of hAuNP. Confocal fluorescence imaging of SK-MEL-28 cells only (A), HEp2 cells only (B), and a coculture of SK-MEL-28 and HEp2 cells(C) treated with 0.5nM TYR hAuNPs (red) and a live-cell nuclear stain, Syto13 (green). DIC composite (left), Syto13 (center) and TYR hAuNP (right). All images were captured with identical optical settings. Scale bar: 20 µm

Thirty minutes prior to confocal imaging, cell cultures were treated with 100 nM Syto-13 to provide a comprehensive cellular marker that is ubiquitous to each cell type (Fig 2). The tyrosinase expressing SK-MEL-28 cells displayed a strong TYR hAuNP signal localized to the cytosolic portion of the cell while TYR hAuNP fluorescence in HEp2 cells was not apparent at analogous detector gains. Additionally, a TYR hAuNP treated coculture of SK-MEL-28 and HEp2 cells (50/50) unequivocally shows the potential of these novel mRNA probes to discriminate individual cells based on inherent gene expression.

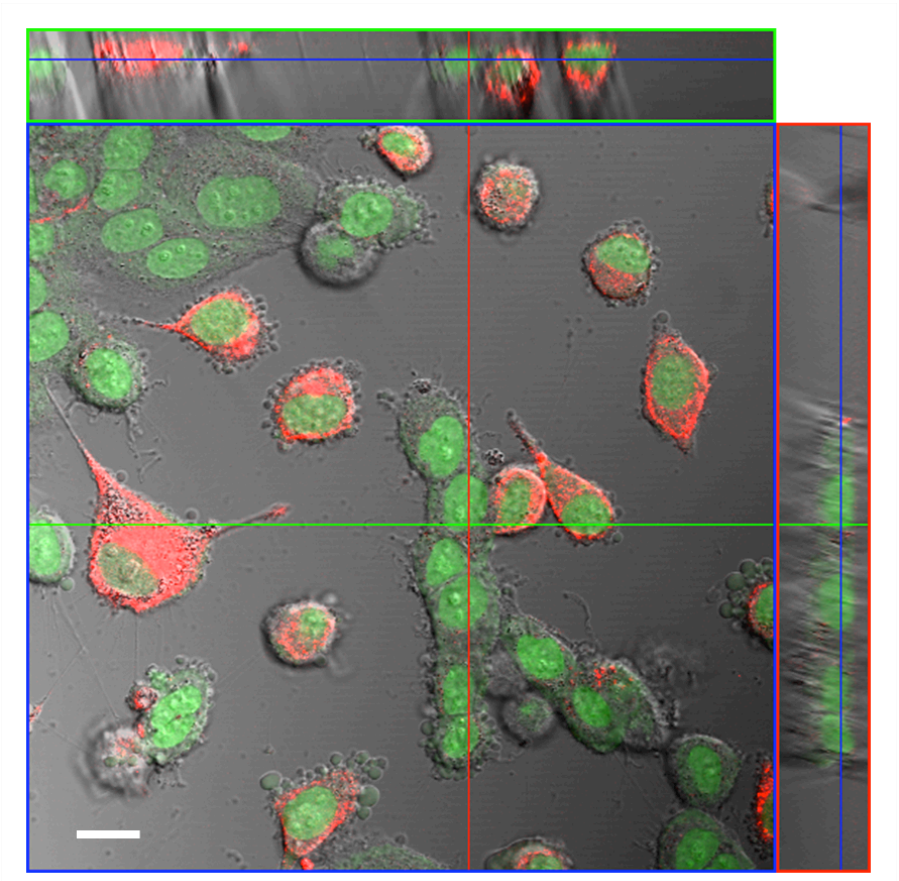

Figure 35. Z-stack confocal image of cocultured SK-MEL-28 and HEp2 cells. Cells were treated with TYR hAuNPs (red) and the nuclear stain Syto13 (green). The 3 dimensional cutout at the top of the image shows TYR hAuNPs localized to the cytosolic portion of the cell and do not penetrate nucleus. Scale bar: 20 µm

Examination of the 3D confocal image obtained for the coculture image revealed the absence of colocalization with respect to the nucleus of the cell (**figure 35**). The top z-plane explicitly shows the presence of the TYR hAuNPs evenly distributed in the cytoplasm while not colocalizing with the Syto13 stained nucleus. Collectively, these results prove that TYR hAuNP probes are not only capable of detecting specific mRNA within the cell but that this information can be used to discriminate a cancerous cell from non-cancerous cell within a complex background. Flow cytometry of the labelled 50/50 mix of SK-MEL-28 and HEp2 cells confirmed two distinct populations (SK-MEL-28, 51.3%; HEp2, 46.1%) with SK-MEL-28 cells exhibiting a 3-fold increase in cellular mean fluorescence as compared to the HEp2 cells (**figure 36**).

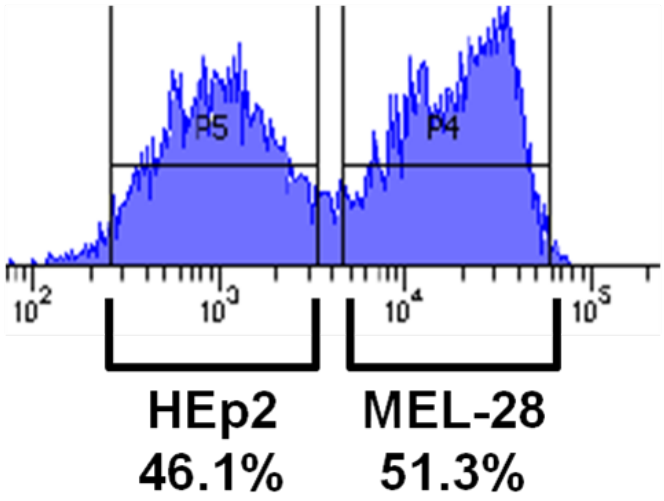

Figure 36. Co-culture Flow Cytometric Analysis. An equal number of SK-MEL-28 and HEp2 cells were treated with TYR hAuNP (0.5 nM) simulatiously in the same culture well. Flow cytometric analysis confirms the expected 50/50 cell type ratio with SK-MEL-28 cells exhibiting a 20-fold increase in Cy5 mean fluorescence (mean: 21K) as compared to the HEp2 cell population (mean: 1.2K).

While the use of immortalized cell lines for the development of biodiagnostic tools is a common procedure, results do not always translate when applied to primary cell

culture conditions. For this reason, we obtained primary melanoma cells excised from a 66 year-old stage IIIC melanoma patient and treated them with both TYR hAuNPs and MM hAuNPs as previously described. Confocal imaging confirmed the utility of this novel mRNA probe as shown by the intense fluorescence exhibited in the TYR hAuNP treated melanoma cells as compared to the MM hAuNP treated culture (**figure 37**). These results collectively demonstrate the ability of TYR hAuNPs to positively identify tyrosinase mRNA in primary melanoma cells.

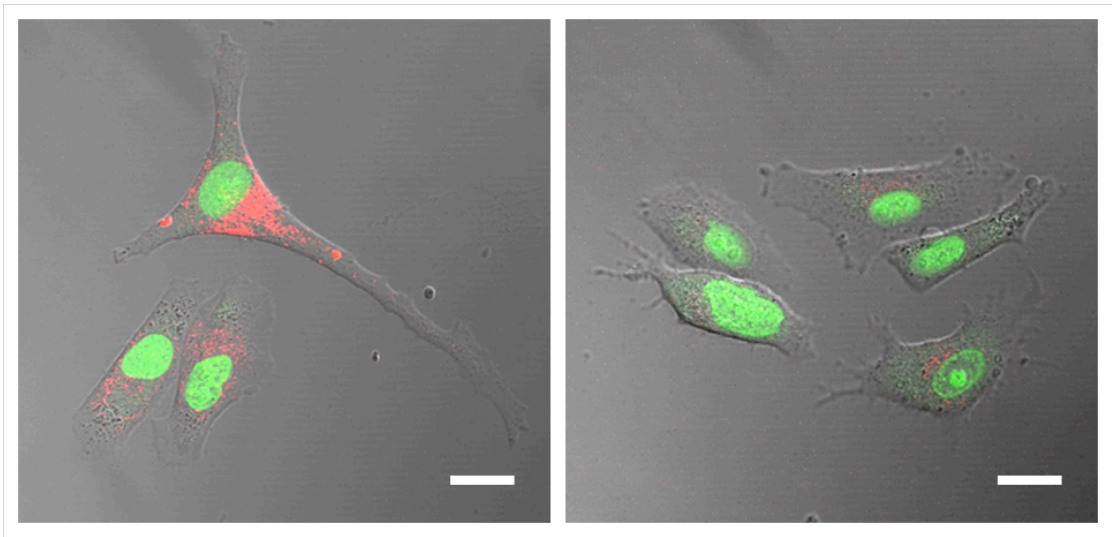

Figure 37. Confocal fluorescence imaging of primary melanoma cells from a 66 year-old stage IIIC melanoma patient. Melanoma cells were treated with either TYR hAuNPs (left) or MM hAuNPs (right). Images were captured with identical optical parameters. hAunPs (red) and Syto13 (green). Scale bars: 20 μm

Hairpin DNA functionalized gold nanoparticles represent an effective intercellular mRNA imaging tool. These novel intercellular probes maintain advantages over traditional molecular mRNA imaging techniques in that no transfection reagents are needed, they are resistant to nuclease degradation and they provide an assessment of gene expression at the single cell level. Their efficacy in primary cell cultures provides an

avenue for exploring more complex diagnostic capabilities including individual gene expression profiling for a variety of cancer types including melanoma.

To further explore the utility of hAuNPs as discriminative intracellular mRNA probes, we designed two additional melanoma marker probes (S100β and MIA) and a housekeeping probe (βactin) to serve as a universal marker for cell type variability.[32-34] The S100β protein is a calcium binding protein that is constitutively expresses in brain astrocytes and malignant melanoma.[34] A common approach for detection of metastatic disease is the analysis of S100β in the serum of melanoma patients.[35] An elevation of this protein has been observed in patients with malignant melanoma, and a positive correlation with disease progression has been demonstrated.[5] Another emerging serological marker is the melanoma inhibitory activity (MIA) protein.[36] MIA has been identified as a small protein secreted from malignant melanoma cells that inhibits integrin-matrix binding which promotes cell migration.[37] Unlike the tyrosinase gene, MIA gene expression has only been observed in metastatic melanoma and absent in normal skin-derived melanocytes. Incorporation of these two targets with the proven TYR probe allows for development of a intracellular gene expression profile that can easily be performed with standard flow cytometric analysis.

As with the TYR probe design, extensive BLAST search comparison was performed to ensure complete overlap of the recognition sequence with each respective mRNA molecule. The S100β and MIA probe design incorporated a 3' Quasar 670 fluorophore and the βactin probe was designed with a terminal Quasar 570 fluorophore (Cy3 equivalent). The sequences for each target are shown in **table 3**. Dithiolthreitol reduction of the S100β, MIA and βactin probes resulted in oligonucleotide-to-particle

ratios of ~110, ~100 and ~120 DNA strands per hAuNP, respectively. Absorption spectroscopy confirmed the characteristic 522 nm plasmon peak remained unchanged after covalent attachment of DNA for each probe.

Table 3. Melanoma hAuNP Oligonucleotide Sequence Information

Melanoma hAuNP Profile Probe Sequences

	Oligonucleotide Probe Sequence (5'-3')*	3' Dye
Tyr Probe	T_{10}-GCACG ATTGTGCATGCTGCTTTGAG CGTGC	Quasar 670
S100β Probe	T_{10}-GCACG CAGTAGTAACCATGGCAACA CGTGC	Quasar 670
MIA Probe	T_{10}-GCACG AGGTTTCAGGGTCTGGTCCT CGTGC	Quasar 670
MM Probe	T_{10}-GCACG ACTCAAGGCACATCGCAATA CGTGC	Quasar 670
βactin Probe	T_{10}-GCACG GGAGTTGAAGGTAGTTTCGT CGTGC	Quasar 570

*All sequences incorporate a 5' C6 thiol.
**Underlined represent hairpin formation sequences.

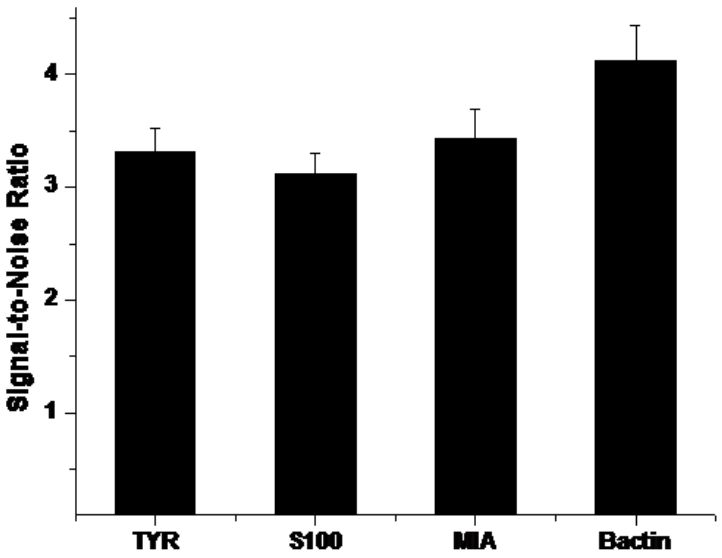

Figure 38. hAuNP Specificity of Melanoma Profile Probes. hAuNPs signal-to-noise ratios were determined by in vitro incubation with complementary and non-complementary oligonucleotides. S/N ratios were determine by comparison of specific vs nonspecific fluorescent signal.

To confirm target specificity of each probe *in vitro*, hAuNPs (1 nM) were incubated with the appropriate 20 base complement versus a 20 base non-complementary oligonucleotide for 2 hr at 37°C. As previously shown with TYR hAuNPs, each probe displays good specificity with > 3 fold increase in signal in the presence of the respective proper complement when compared to mismatch DNA (**figure 38**). *In vivo* confocal imaging of SK-MEL-28 cells treated with each melanoma marker probe confirmed intracellular utility of each probe, each having pronounced fluorescent signals as compared to control experiments (**figure 39**).

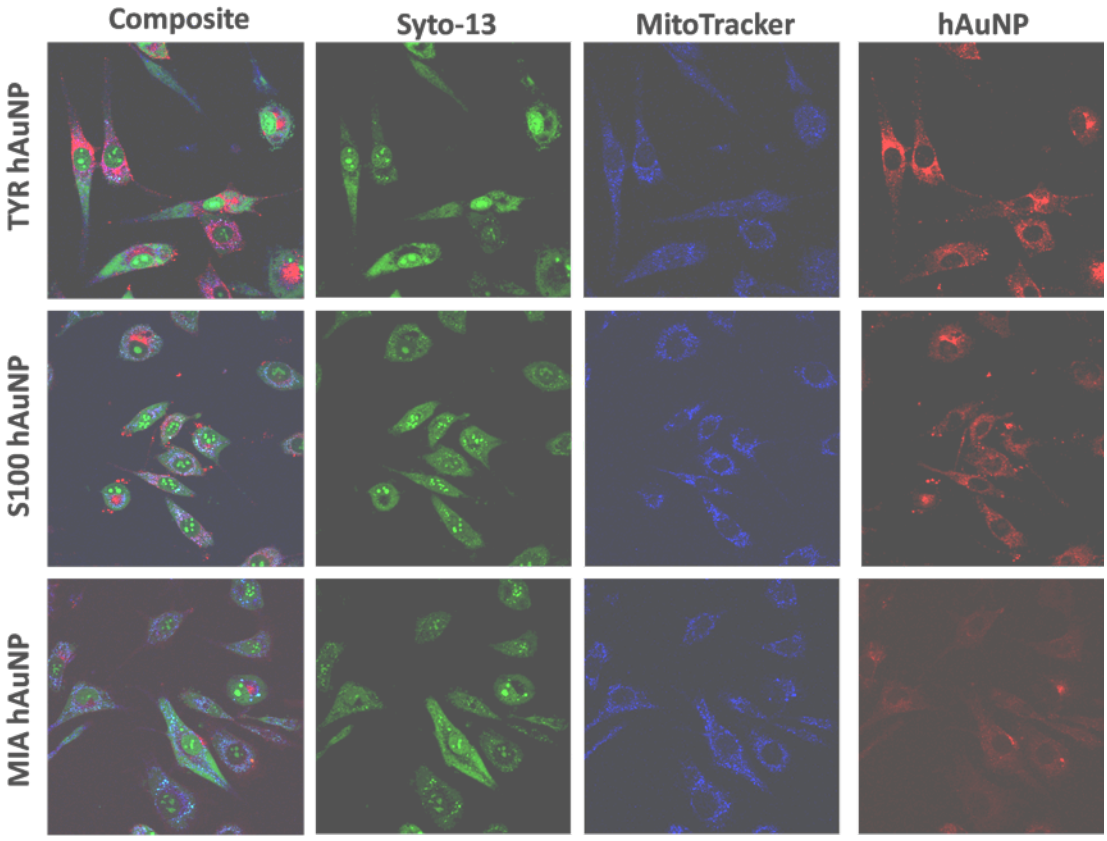

Figure 39. Scanning Confocal Imaging of Melanoma Profile hAuNPs. SK-MEL-28 cells were treated with 25 nM syto-13 nuclear stain (green), 5 nM MitoTracker (blue) and hAuNPs (red). Images were obtained with identical optical setting.

In melanoma progression, a variety of gene mutations occur that can initiate metastasis that influence melanoma progression.[38] The specifics associated with which genes are expressed rely on a signature phenotype for cancers such as melanoma. For example, the RAF kinase pathway mediates cellular responses to growth signals.[39] The BRAF somatic missense mutation is observed in over 60% of malignant melanomas[39] while another subset code for oncogenic mutations in KIT which code for nearly 20% of all melanoma mutations.[38] Each mutant oncogene responds differently to current treatment protocols.[40] This highlights the need for accurate and timely determination of malignant melanoma phenotype. By incorporating multiple melanoma expression targets into the hAuNP system, the goal is to develop a quick and non-invasive method for identifying the phenotypic classification of clinical melanoma diagnosis.

To explore the ability of hAuNPs to effectively discriminate phenotypic characteristics of malignant melanoma, a multicellular hAuNP profile experiment was performed using three melanoma-specific expression markers and a housekeeping β-actin probe for evaluation of phenotypic variations between human melanoma cell lines. To do this, the cell lines SK-MEL-28, Wm115, MeWo, and HS-294T human melanoma cell lines as well as the non-melanocytic HEp2 cell line were treated with 0.25 nM melanoma marker hAuNPs and 0.25 nM βactin hAuNPs followed by flow cytometric analysis. To form comparative expression values, the mean fluorescence of each probe was divided by the mean fluorescence of the βactin probe, which served as an internal control for cellular variability. Each hAuNP expression value was then normalized to the mismatch probe to give relative hAuNP expression values for each gene target as shown in the following equation:

□h□□□□=□□□□□□□ □□□□□□□□□□□ □□□□□ □□□□□□□□□□□□□□□ □□□□□□□□□□□

□□□□□ □□□□□□□□□□□□□□

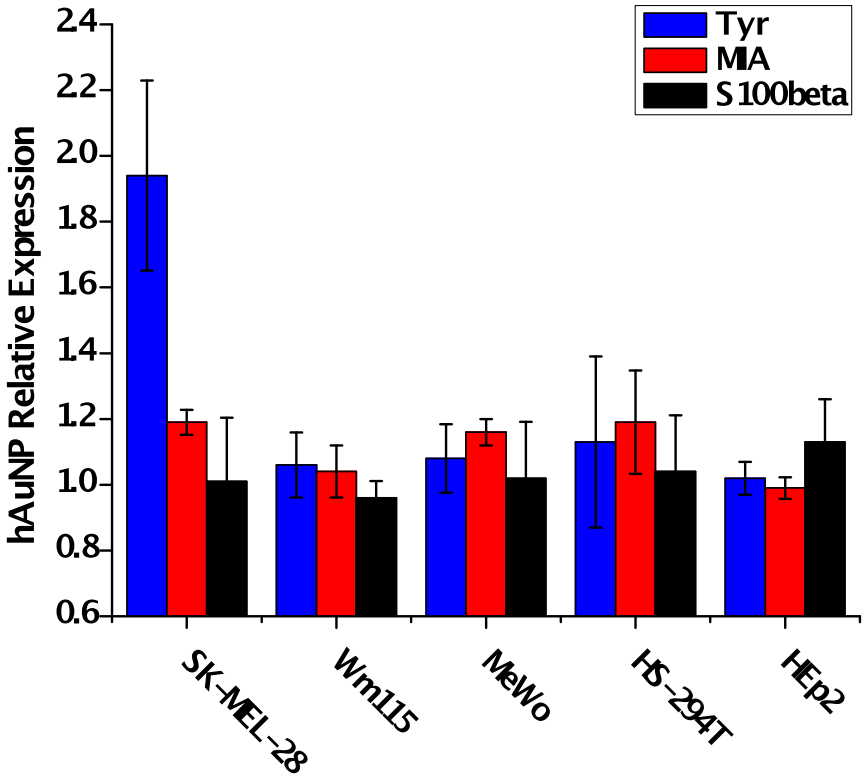

Figure 40. hAuNP Expression Values for Multiple Melanoma Cell Lines. (blue) Tyrosinase expression values, (red) MIA hAuNP expression values and (black) S100 hAuNP expression values.

α = hAuNP relative expression value

Table 4. hAuNP Expression Values for Multiple Melanoma Cell Lines

hAuNP Melanoma Expression Values			
	TYR	MIA	S100β
SK-MEL-28	1.94 ± 0.29	1.19 ± 0.04	1.01±0.19
Wm115	1.06 ± 0.10	1.04 ± 0.08	0.96 ± 0.05
MeWo	1.08 ± 0.10	1.16 ± 0.04	1.02 ± 0.17
HS-294T	1.13 ± 0.26	1.19 ± 0.16	1.04 ± 0.17
HEp2	1.02 ± 0.05	0.99 ± 0.03	1.13 ± 0.13

The results of the hAuNP expression profile explicitly show that SK-MEL-28 cells have high expression of tyrosinase as compared to the other melanoma cell lines (**figure 40; table 4**). Additionally, MIA expression levels were consistently higher each melanoma cell line. Interestingly, S100β values were not very conclusive and in fact, HEp2 cells displayed a slightly higher S100β signal. Extensive literature research does not indicate S100β expression in HEp2 cell lines but more insight is needed to evaluate this observation.

To assess the accuracy of the hAuNP melanoma expression profile, RT-PCR was performed for each cell line to determine the comparative expression values for each melanoma oncogene. The gene expression values were based on Ct values which were based on the comparative Ct method where the relative transcript level of each target gene was calculated according to the equation $2^{-\Delta Ct}$, where ΔCt is defined as Ct target

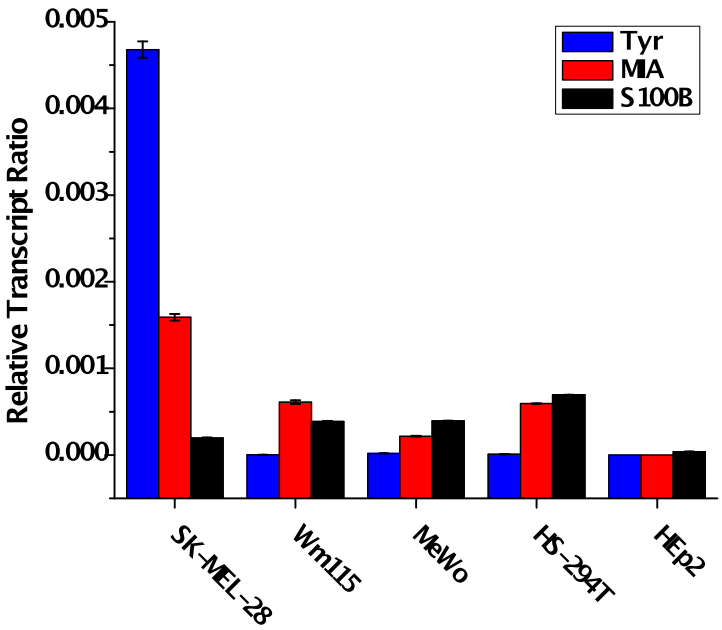

Figure 41. RT-PCR Relative Transcription Ratios for Experimental Cell Lines.

gene - Ct βactin gene (**figure 41; table 5**).

Table 5. RT-PCR Relative Transcription Ratios for Multiple Melanoma Cell Lines

	RT-PCR Melanoma Ct Values		
	TYR	MIA	S100β
SK-MEL-28	4.68 ± 0.09E-3	1.59 ± 0.04E-3	1.96 ± 0.06E-4
Wm115	1.26 ± 0.06E-6	6.10 ± 0.23E-4	3.86 ± 0.06E-4
MeWo	1.85 ± 0.01E-5	2.17 ± 0.05E-4	3.94 ± 0.04E-4
HS-294T	7.74 ± 0.20E-6	5.93 ± 0.06E-4	6.95 ± 0.02E-4
HEp2	N/A	N/A	3.89 ± 0.03E-5

At first glance, the majority of expression variability as a whole was too insignificant to form an accurate assessment of melanoma phenotype but a significant difference was observed for SK-MEL-28 cells in both gene expression assessments. The most apparent result showed a strong correlation of tyrosinase expression in both hAuNP and RT-PCR experiments. Another observation was the elevated MIA hAuNP values for melanoma cell lines which didn't discriminate between cell lines but did correlate to the absence of HEp2 comparative RT-PCR values. Furthermore, the similar lack of magnitude of expression values for each method could actually be attributed to cell type. To the best of our knowledge, this is the first study that has analyzed comparative RT-PCR of tyrosinase mRNA across these particular melanoma cell lines. The analogous measurement by the hAuNP expression value profile demonstrates the potential of hAuNP as a future diagnostic tool. The possibility of using these intracellular mRNA probes for measuring a cancer cell's gene expression profile in a matter of hours could greatly assist in a more accurate diagnosis and treatment.

Conclusions

As we learn more about the systematic process of cellular function, the need and demand for new intracellular tools capable of relaying accurate information regarding cellular status is of utmost importance. Unlike foreign microbes, cancerous cells do not exhibit intrinsic characteristics that are recognized by the body's immune system and therefore remain to be the focus of continued research. New paradigms are beginning to emerge due to focused attention on cellular dysfunction, namely gene expression. The most common technique for measuring gene expression is RT-PCR but while sensitive and well excepted, the extensive sample preparation, high risk of false results due to contamination and need to extract mRNA from a large population of cells does not make this technique viable for future clinical use. The ability to evaluate and measure statistics on a single cell level have yet to be mastered completely but emerging microfluidic technology as well as micro-analytical technologies holds promise for such future applications.

Herein, a new intracellular mRNA recognition nanoparticle probe is presented that is capable of discriminating melanoma cells, both primary and immortilized, from mixed cell cultures. The hAuNP construct is a unique intracellular probe due to its inherent ability to accumulate in the cytoplasm of the cell, lack of cytotoxicity and decreased nuclease susceptibility. The fluorescence quenching nature of the gold nanoparticle provides the needed 'on/off' switch that relays information upon target mRNA binding events.[27] The difference associated with live cell measurements of gene expression versus end-point measurements such as RT-PCR have yet to be sufficiently

evaluated which highlights the need for novel methods for live-cell gene analysis. The vast array of knowledge associated with cancer-associated gene expression is constantly growing with much to learn in the future. Having clinical tools to personalize cancer diagnostics is of utmost importance for initial diagnosis, post-treatment assessments and phenotypic evaluation which will maximize treatment efficacy. Nanoscale diagnostic probes such as hairpin DNA coated gold nanoparticles provide a functional means to developing tools that will revolutionize the way society approaches cancer diagnosis and treatment.

Future Directions

In recent years, there have been a variety of gold nanoparticle diagnostics developed that address many issues associated with vaccine development, protein/antigen detection and intracellular delivery, detection and modulation. Each subset has great potential to incrementally revolutionize modern diagnostics as we see it today. The intracellular mRNA detection probe presented in this chapter is merely a well developed prototype capable of addressing many of the current hurdles associated with live cell imaging of intracellular mRNA. In addition to their overall cellular compatibility, hAuNPs, provide a unique real-time quantitative assessment of intracellular mRNA using well established techniques such as flow cytometry and confocal microscopy.

The hAuNP modular design was inspired by traditional DNA beacon technologies and is far from optimized for maximum efficacy in regards to the size and ratio of the stem-loop DNA. Additionally, a better understanding of the exact orientation of surface hairpin oligonucleotides as well as the influence of hairpin secondary structure is needed. Several experiments were performed that incorporated various molar ratios of thiolated spacer ligands including 6-mercaptohexanoic acid (MHA) and C6- thiol T10 oligonucleotides but were not effective due to aggregation issues (MHA) and no appreciable increase in signal-to-noise. The gold particle size (15 nm) used for this study proved to be an effective scaffold with ~ 100 strands per particle but there is plenty to be learned from different sizes and shapes which modulate the gold plasmon peak to expand the range of quenchable fluorophores.

The current experimental protocol for cellular hAuNP loading was optimized for 0-3 nM solutions and 8-12 hr hybridization periods but due to time constraints, higher hAuNP loading concentrations and shorter hybridization periods should be explored to expand the robustness and throughput of the probe. The current protocol requiring a 4 hr hAuNP loading and 12 hr hybridization period is a very taxing experimental design for future researchers due to the elongated processing time. Refinement in this area will allow for increase experimental throughput as well as a much more sustainable experiment design for the researcher.

There are several oligonucleotide design areas that would greatly benefit from modest financial investments. First, the incorporation of locked nucleic acids or o-methyl nucleic acids would essentially eliminate the intracellular endogenous nuclease activity resulting in reduced background noise in all aspects. One potential side-effect of these nuclease resistant oligonucleotides is a disruption of the salt-stabilization phenomenon which can only be determined experimentally. Secondly, the recognition sequences used for each probe in this chapter were designed from a published antisense primer. While the current method proves to be successful by comparison to the designed mismatch sequence, the evaluation of multiple recognition sites for a single mRNA target would be useful for accurately identifying an optimum recognition sequence. Additionally, multiple recognition sites for a single mRNA molecule could lend to multiplexed hAuNPs that could overcome low expression by increaseing the signal **x**-fold, where **x** is equivalent to the number of viable recognition sequences for a single target.

References

1. *National Cancer Institute* **2006**.

2. Hearing, V. J.; Tsukamoto, K. *FASEB J* **1991**, *5*, 2902-9.

3. Goetz, T. In *Wired* 2009.

4. O'Connell, C. D.; Juhasz, A.; Kuo, C.; Reeder, D. J.; Hoon, D. S. B. *Clinical Chemistry* **1998**, *44*, 1161-1169.

5. Andres, R.; Mayordomo, J. I.; Visus, C.; Isla, D.; Godino, J.; Escudero, P.; Saenz, A.; Ortega, E.; Lastra, R.; Lambea, J.; Aguirre, E.; Elosegui, L.; Marcos, I.; Ruiz-Echarri, M.; Millastre, E.; Saez-Gutierrez, B.; Asin, L.; Vidal, M. J.; Ferrer, A.; Giner, A.; Larrad, L.; Carapeto, F. J.; Tres, A. *Am J Clin Oncol* **2008**, *31*, 335-9.

6. Gry, M.; Rimini, R.; Stromberg, S.; Asplund, A.; Ponten, F.; Uhlen, M.; Nilsson, P. *BMC Genomics* **2009**, *10*, 365.

7. Mocellin, S.; Rossi, C. R.; Pilati, P.; Nitti, D.; Marincola, F. M. *Trends Mol Med* **2003**, *9*, 189-95.

8. Nezos, A.; Lembessis, P.; Sourla, A.; Pissimissis, N.; Gogas, H.; Koutsilieris, M. *Clin Chem Lab Med* **2009**, *47*, 1-11.

9. de Vries, T. J.; Fourkour, A.; Punt, C. J.; Diepstra, H.; Ruiter, D. J.; van Muijen, G. N. *Br J Cancer* **1999**, *81*, 1066-70.

10. Stevens, G. L.; Scheer, W. D.; Levine, E. A. *Cancer Epidemiology, Biomarkers and Prevention* **1996**, *5*, 293-296.

11. Gradilone, A.; Ribuffo, D.; Silvestri, I.; Cigna, E.; Gazzaniga, P.; Nofroni, I.; Zamolo, G.; Frati, L.; Scuderi, N.; Agliano, A. M. *Ann Surg Oncol* **2004**, *11*, 983-7.

12. Arenberger, P.; Arenbergerova, M.; Gkalpakiotis, S.; Lippert, J.; Stribrna, J.; Kremen, J. *European Academy of Dermatology and Venereology* **2008**, *22*, 56-64.

13. Bao, G.; Rhee, W. J.; Tsourkas, A. *Annu Rev Biomed Eng* **2009**, *11*, 25-47.

14. Santangelo, P.; Nitin, N.; Bao, G. *Ann Biomed Eng* **2006**, *34*, 39-50.

15. Santangelo, P.; Nitin, N.; LaConte, L.; Woolums, A.; Bao, G. *J Virol* **2006**, *80*, 682-8.

16. Santangelo, P. J.; Nitin, N.; Bao, G. *J Biomed Opt* **2005**, *10*, 44025.

17. Chen, A. K.; Behike, M. A.; Tsourkas, A. *Nucleic Acids Research* **2007**, *35*, 1-12.

18. Walev, I.; Bhakdi, S. C.; Hofmann, F.; Djonder, N.; Valeva, A.; Aktories, K.; Bhakdi, S. *Proc Natl Acad Sci U S A* **2001**, *98*, 3185-90.

19. Tsourkas, A.; Behlke, M. A.; Bao, G. *Nucleic Acids Res* **2003**, *31*, 5168-74.

20. Tsourkas, A.; Behlke, M. A.; Rose, S. D.; Bao, G. *Nucleic Acids Res* **2003**, *31*, 1319-30.

21. Tyagi, S.; Kramer, F. R. *Nature Biotechnology* **1996**, *14*, 303-308.

22. Alivisatos, A. P.; Johnsson, K. P.; Peng, X.; Wilson, T. E.; Loweth, C. J.; Bruchez, M. P., Jr.; Schultz, P. G. *Nature* **1996**, *382*, 609-11.

23. Mirkin, C. A.; Letsinger, R. L.; Mucic, R. C.; Storhoff, J. J. *Nature* **1996**, *382*, 607-9.

24. Rosi, N. L.; Giljohann, D. A.; Thaxton, C. S.; Lytton-Jean, A. K. R.; Han, M. S.; Mirkin, C. A. *Science* **2006**, *312*, 1027-1030.

25. Seferos, D. S.; Giljohann, D. A.; Hill, H. D.; Prigodich, A. E.; Mirkin, C. A. *J. Am. Chem. Soc.* **2007**, *129*, 15477-15479.

26. *http://www.tedpella.com/gold_html/gold-tec.htm*.

27. Dubertret, B.; Calame, M.; Libchaber, A. J. *Nature Biotechnology* **2001**, *19*, 365-370.

28. Giljohann, D. A.; Seferos, D. S.; Prigodich, A. E.; Patel, P. C.; Mirkin, C. A. *J. Am. Chem. Soc.* **2009**, *131*, 2072-2073.

29. Lytton-Jean, A. K. R.; Mirkin, C. A. *J. Am. Chem. Soc.* **2005**, *127*, 12754-12755.

30. Seferos, D. S.; Prigodich, A. E.; Giljohann, D. A.; Patel, P. C.; Merkin, C. A. *Nano Letters* **2009**, *9*, 308-311.

31. Nezos, A.; Lembessis, P.; Sourla, A.; Pissimissis, N.; Gogas, H.; Koutsilieris, M. *Clin Chem Lab Med* **2009**, *47*, 1-11.

32. Enk, C. D.; Lotem, M.; Gimon, Z.; Hochberg, M. *Melanoma Res* **2004**, *14*, 361-5.

33. Horikoshi, T.; Danenberg, K. D.; Stadlbauer, T. H.; Volkenandt, M.; Shea, L. C.; Aigner, K.; Gustavsson, B.; Leichman, L.; Frosing, R.; Ray, M.; et al. *Cancer Res* **1992**, *52*, 108-16.

34. Kan-Mitchell, J.; Liggett, P. E.; Taylor, C. R.; Rao, N.; Granada, E. S.; Danenberg, K. D.; White, W. L.; Van Eldik, L. J.; Horikoshi, T.; Danenberg, P. V. *Invest Ophthalmol Vis Sci* **1993**, *34*, 3366-75.

35. Garbe, C.; Leiter, U.; Ellwanger, U.; Blaheta, H.-J.; Meier, F.; Rassner, G.; Schittek, B. *Cancer* **2003**, *97*, 1737-1745.

36. Bosserhoff, A. K. *Pigment Cell Res* **2005**, *18*, 411-6.

37. Bauer, R.; Humphries, M.; Fassler, R.; Winklmeier, A.; Craig, S. E.; Bosserhoff, A. K. *J Biol Chem* **2006**, *281*, 11669-77.

38. Curtin, J. A.; Busam, K.; Pinkel, D.; Bastian, B. C. *J Clin Oncol* **2006**, *24*, 4340-6.

39. Davies, H.; Bignell, G. R.; Cox, C.; Stephens, P.; Edkins, S.; Clegg, S.; Teague, J.; Woffendin, H.; Garnett, M. J.; Bottomley, W.; Davis, N.; Dicks, E.; Ewing, R.; Floyd, Y.; Gray, K.; Hall, S.; Hawes, R.; Hughes, J.; Kosmidou, V.; Menzies, A.; Mould, C.; Parker, A.; Stevens, C.; Watt, S.; Hooper, S.; Wilson, R.; Jayatilake, H.; Gusterson, B. A.; Cooper, C.; Shipley, J.; Hargrave, D.; Pritchard-Jones, K.; Maitland, N.; Chenevix-Trench, G.; Riggins, G. J.; Bigner, D. D.; Palmieri, G.; Cossu, A.; Flanagan, A.; Nicholson, A.; Ho, J. W.; Leung, S. Y.; Yuen, S. T.; Weber, B. L.; Seigler, H. F.; Darrow, T. L.; Paterson, H.; Marais, R.; Marshall, C. J.; Wooster, R.; Stratton, M. R.; Futreal, P. A. *Nature* **2002**, *417*, 949-54.

40. Hodi, F. S.; Friedlander, P.; Corless, C. L.; Heinrich, M. C.; Mac Rae, S.; Kruse, A.; Jagannathan, J.; Van den Abbeele, A. D.; Velazquez, E. F.; Demetri, G. D.; Fisher, D. E. *J Clin Oncol* **2008**, *26*, 2046-51.